7-28-2011

Novel Feature-Based Methods for Improved Glaucoma Detection and Progression Prediction

Young June June Kim

To the University Council:

The Dissertation Committee for Young June Kim certifies that this is the final approved version of the following electronic dissertation: "Novel Feature-based Methods for Improved Glaucoma Detection and Progression Prediction."

_____

Khan M. Iftekharuddin, Ph.D.
Major Professor

We have read this dissertation and recommend its acceptance:

_____

Pinakin G. Davey, Ph.D.

_____

Aaron L. Robinson, Ph.D.

_____

Ebenezer O. George, Ph.D.

_____

Peter S. Lau, Ph.D.

Accepted for the Graduate Council:

_____

Karen D. Weddle-West, Ph.D.
Vice Provost for Graduate Programs

NOVEL FEATURE-BASED METHODS FOR IMPROVED GLAUCOMA DETECTION AND PROGRESSION PREDICTION

by

Young June Kim

A Dissertation

Submitted in Partial Fulfillment of the

Requirements for the Degree of

Doctor of Philosophy

Major: Electrical and Computer Engineering

The University of Memphis

August 2011

To my parents and my family

ACKNOWLEDGMENT

First of all, I would like to thank God for all his grace upon me in my pursuit of this Ph.D. study.

My heartfelt thanks go to my advisor Dr. Khan M. Iftekharuddin for his unlimited patience, support and guidance. I am truly grateful for his supervision of this dissertation with such great dedication. He has borne with me time and again in every aspect of this research work. My very sincere thanks also go to my co-advisor Dr. Pinakin G. Davey who has shown his constant support during my Ph.D. work and brought new dimensions into my glaucoma research. He has given me so many valuable advices and broadened my thinking about this topic with his brilliant insight. I also give thanks to Drs. Ebenezer O. George, Aaron L. Robinson and Peter S. Lau for their valuable comments and suggestions with statistical knowledge and signal processing expertise.

I give my special thanks to my wife who has been constantly supporting me. Among my friends, I would like to thank Yong Ren, Shaheen Ahmed and Keith Anderson who put so much of their time for me. My grateful heart goes also to other Intelligent Systems and Image Processing (ISIP) lab members, Mahmud, Suzan, Sushil, Teddy, Jakir and Supriya for their cordial support. Finally, I would like to thank Ms. Becky Ward for being there for me whenever I needed anything from her.

This work was supported in part by the grants from the ASSISI Foundation of Memphis (09-066) and Southern College of Optometry. The same grants also supported the equipment of Dell Precision M2400 Mobile Workstation and IBM SPSS Statistics 18. Finally, this work was used in applying for a US patent (USPTO S/N: 61/234803).

ABSTRACT

Kim, Young June. Ph.D. The University of Memphis. August 2011. Novel Feature-Based Methods for Improved Glaucoma Detection and Progression Prediction. Major Professor: Khan M. Iftekharuddin, Ph.D.

Glaucoma is a leading cause of blindness worldwide. Since glaucomatous vision loss is irreversible, early detection is essential to prevent or manage this disease. Assessing retinal nerve fiber layer (RNFL) using imaging technologies plays an important role in early glaucoma detection. However, accurate evaluation of the RNFL using such technologies can be limited due to overlaps. In literature, feature-based techniques such as fast-Fourier analysis and wavelet-Fourier analysis have shown better diagnostic capability over the standard methods. Nevertheless, such techniques may not fully represent local variation and randomness in the RNFL.

Similarly, progression prediction is also critical. Assessing visual field (VF) data using standard automated perimetry (SAP) has been widely used in diagnosing glaucomatous progression. However, use of VF data is functional and subjective and VF data analysis may not fully indicate true progression due to short-term and long-term fluctuation. Hence, diagnosis of progression in an objective and quantitative manner still remains challenging. For progression prediction, it is necessary to differentiate the patients according to the severity of progression. Consequently, progression prediction at different disease stages may require classifiers involving more than two classes.

The primary contribution of this dissertation is investigation of feature-based techniques that exploit novel fractal features. These fractal features have shown better characterization of local variation and randomness in structural changes in the RNFL. Consequently, our novel fractal features offer improved glaucoma detection and

progression prediction capability than the standard methods and other feature-based techniques. A novel multi-class classification is further proposed for enhanced progression prediction.

Glaucoma is known to be characterized by both structural and functional changes. For a complete assessment of glaucoma, it is therefore essential to consider both structural and functional changes. In this work, we exploit a known topographic correspondence between structural and functional data for selective fusion of respective features from both data for improved glaucoma detection.

Statistical analyses show that our novel fractal features, multi-class classification and selective fusion of structural and functional data have better diagnostic and predictive capability of glaucoma and glaucomatous progression, when compared with the existing standard and feature-based techniques.

PREFACE

This dissertation follows the guideline of Proc. of SPIE Medical Imaging 2011. This dissertation was also submitted to Proc. of SPIE Medical Imaging 2011 for publication.

TABLE OF CONTENTS

LIST OF TABLES

LIST OF FIGURES

1. Introduction

1.1. Dissertation Overview

Glaucoma is a slow progressive optic neuropathy in which there is an accelerated loss of retinal ganglion cells. Its primary form, primary open angle glaucoma (POAG), leads to progressive cupping of optic disc, thinning of retinal nerve fiber layer (RNFL) and visual field (VF) damage [1]. Once glaucomatous damage has occurred to the optic nerve, it is irreversible. Hence, its early detection and thus intensifying treatment is the best way of managing the disease. However, since POAG has no obvious symptoms or signs until there is severe vision loss it is difficult to identify in its early stages [2]. Over the years, testing VF defects, examining the shape of the optic disc, and evaluating the RNFL have been used to diagnose glaucoma. Among these methodologies, assessing the RNFL has been an integral part of glaucoma detection [3-4]. Generally, assessing the RNFL requires sophisticated non-invasive medical imaging technologies such as scanning laser polarimetry (SLP) and optical coherence tomography (OCT) [5-6].

The version of SLP that this dissertation work utilizes is GDx-variable corneal compensator (GDx-VCC: Carl Zeiss Meditec Dublin, California, software version 5.4.0.27). GDx-VCC measures the anterior segment birefringence and determines an estimate of polarization retardation. The polarization retardation is then converted to an estimate of the thickness of the RNFL [7]. The version of OCT that this work utilizes is StratusOCT (Carl Zeiss Meditec USA, software version 4.04). StratusOCT measures infrared light waves that reflect off the retina. By adopting interferometry, StratusOCT obtains interference fringes which are electronically processed to determine reflectivity values of the sample as a function of the depth of the RNFL [8].

The assessment of the RNFL either by SLP or OCT may be done using its mean values at different locations around the parapapillary retina at a given distance from the optic disc as a function of angle. Such a thickness graph is known as a temporal, superior, nasal, inferior, and temporal (TSNIT) graph. A TSNIT graph measures the thickness of a ring around the optic disc. The TSNIT graph shows a general double-hump pattern due to a much greater number of ganglion cells and their axons entering the optic disc superiorly and inferiorly.

Although the mean values of the RNFL TSNIT graphs are sufficient in group separation (glaucomatous from normal eyes), its classification performance can be quite limited due to the overlaps among early glaucomatous eyes. The overlaps cause a wide range of ocular normal values [9]. To address this issue further, GDx-VCC inherently has a classifier called the Nerve Fiber Indicator (NFI). The NFI is a global parameter and ranges from 0 to 100. A value of 0 represents absolute ocular normality and a value of 100 represents absolute glaucoma [5, 7]. However, the classification performance of the NFI can be also limited and many more challenges remain especially in early glaucoma where the RNFL damage is not overt. Furthermore, since the NFI is a global parameter, there can be early glaucoma cases with local RNFL defect not fully reflecting abnormality [7]. Additionally, with no built-in classifier in StratusOCT, there are inherent differences between the RNFL thickness measured by GDx-VCC and that measured by StratusOCT [8, 10-21]. This issue requires more careful research work.

In the literature, feature-based techniques over the RNFL TSNIT graphs have been found more useful in identifying glaucomatous damage than the NFI alone such as fast-Fourier analysis (FFA) and wavelet-Fourier analysis (WFA) [22-23]. However, FFA or

WFA features may not fully represent the inherent randomness and irregularity of the RNFL damages. Furthermore, since FFA and WFA are linear processes they may generate more number of features whereas there may be a nonlinear process that requires small number of features. Accordingly, there is a need for systems and methods for detecting glaucoma that outperform both currently available technology and feature-based techniques such as FFA and WFA.

From many successful research endeavors, fractal analysis (FA) has proved to be more effective in many medical imaging applications such as the detection of micro-calcifications in mammograms, the prediction of osseous changes in ankle fractures, the diagnosis of small peripheral lung tumors and the identification of breast tumors in digitized mammograms [24-26]. In our Intelligent Systems and Image Processing (ISIP) lab, pediatric brain tumor regions have been successfully segmented from normal brain regions by applying a multi-fractal feature-based technique on pediatric brain magnetic resonance imaging (MRI) [27-32].

Therefore, in this dissertation work, we investigate the feature-based techniques for improving the classification performance in early glaucoma detection. We utilize novel features such as fractals and multi-fractals. The novel algorithm based on fractal and multi-fractal features adopts pseudo 2D representation converted from 1D TSNIT RNFL data. Our novel algorithm has shown its enhancing diagnostic ability on glaucoma [33] and has offered comparable results with the existing feature-based techniques such as FFA and WFA [22-23]. In addition, above-mentioned feature-based techniques use only 1D or pseudo 2D TSNIT RNFL data and thus may not fully exploit the real 2D eye scan data.

Consequently, we also investigate the feature-based 2D fractal techniques using real 2D RNFL image data which may provide more information.

Detecting or predicting glaucomatous progression has been known to be essential in the treatment of glaucoma patients in that such detection or prediction may prevent the glaucomatous eyes from further worsening and eventual blindness. Over the years, assessing a series of visual field (VF) data using standard automated perimetry (SAP) has been a major method in detecting and monitoring the progression [34-35]. However, SAP is a functional test and inherently subjective in nature. There is high possibility that a patient's psycho-physical condition affects their alertness level: the reaction of the patient to the visual stimuli may fluctuate [35]. Such variability makes it difficult to distinguish actual progression from random variations. Hence, SAP results may not fully represent true progression from variability.

It has been well known that structural changes often precede distinguishable functional changes in glaucoma and that the subtle changes in the RNFL may also indicate the risk of the progression [3-4]. Since structural changes are measured in an objective and quantitative manner, such changes may better characterize the mechanism of the progression. In this respect, the evaluation of the RNFL using imaging technologies such as SLP and OCT can be a good candidate of more correctly detecting or predicting the progression than the evaluation of functional changes in VF data using SAP [34-35]. However, since the structural progression is slow and heterogeneous, it is very difficult to predict future progressive changes in specific patients. Gunvant *et al*. report that a feature-based technique such as WFA has successfully predicted the progression using SLP data with the AUROC of 0.86 [36]. Essock *et al*. also report the AUROC of 0.83

on SLP data in predicting which patients would progress by obtaining the linear discriminant function (LDF) using the training dataset consisting of glaucomatous and ocular normal patients and applying the obtained LDF to the testing data [37]. Such research works provide substantial promise but the better performance is anticipated, in that detecting the progression using the RNFL evaluation has not been validated or standardized [38]. Hence, it is desirable to establish a feature-based technique that detects and predicts the progression using the novel features such as fractals and multi-fractals. We explore the possibility of obtaining novel features that best characterize the presence of glaucomatous progression. After obtaining such novel features, we investigate the potential of establishing a statistical model which best predicts progressors from non-progressors or ocular normal patients.

For the task addressed as above, it may require more than just two-class classifiers. In statistical analyses, two-class classification has been widely adopted and one of such methods has been support vector machine (SVM). SVM has been extensively used due to its simple geometrical interpretation, statistical robustness and overfitting control [39-40]. Nevertheless, directly applying a two-class SVM on a nonlinearly separable multi-class problem may not result in better classification performance, especially in determining the multi-staged glaucomatous progression [41]. A kernel-based SVM has been proved to be effective in dealing with nonlinearly separable data, due to its capacity of mapping the input data space into the pre-determined kernel-based feature space [42-43]. In addition, a Gaussian kernel has been known to have a corresponding infinite-dimensional feature space with its well regularized bounds. It is highly possible that variations of a Gaussian kernel can well separate nonlinearly separable input data by mapping the input

data. Hence, a Gaussian kernel-based multi-class SVM classifier is investigated in predicting the progression.

Recently, there have been attempts to combine features and classifiers to enhance the classification performance [44-46]. There are also research efforts for combining structural and functional dataset for the detection of glaucoma [47]. For such a task as combining structural and functional dataset for better detecting glaucoma, it has been known that the relationship between structural and functional data should be explained [48]. It has been shown that glaucoma-related structural (e.g., RNFL defect) and functional changes (e.g., VF defect) are closely related to each other. There have been works in comparing different methods in structural and functional analyses to distinguish glaucoma from ocular normal patients [49]. Generally, it is known that there is a local correspondence between structural and functional data even with different methodologies used to measure structural and functional changes. However, very few studies have investigated such a correspondence between local structural measurement and functional losses in the same individuals [48]. Further, very few fusion methods of different feature sets for enhancing the classification performance of glaucoma detection have been reported. Hence, it is desirable to develop the models that analyze both structural and functional data simultaneously and fuse the respective features from them for better glaucoma detection. Consequently, we aim to develop a feature-based selective fusion method for improved glaucoma detection.

1.2. Dissertation Aims

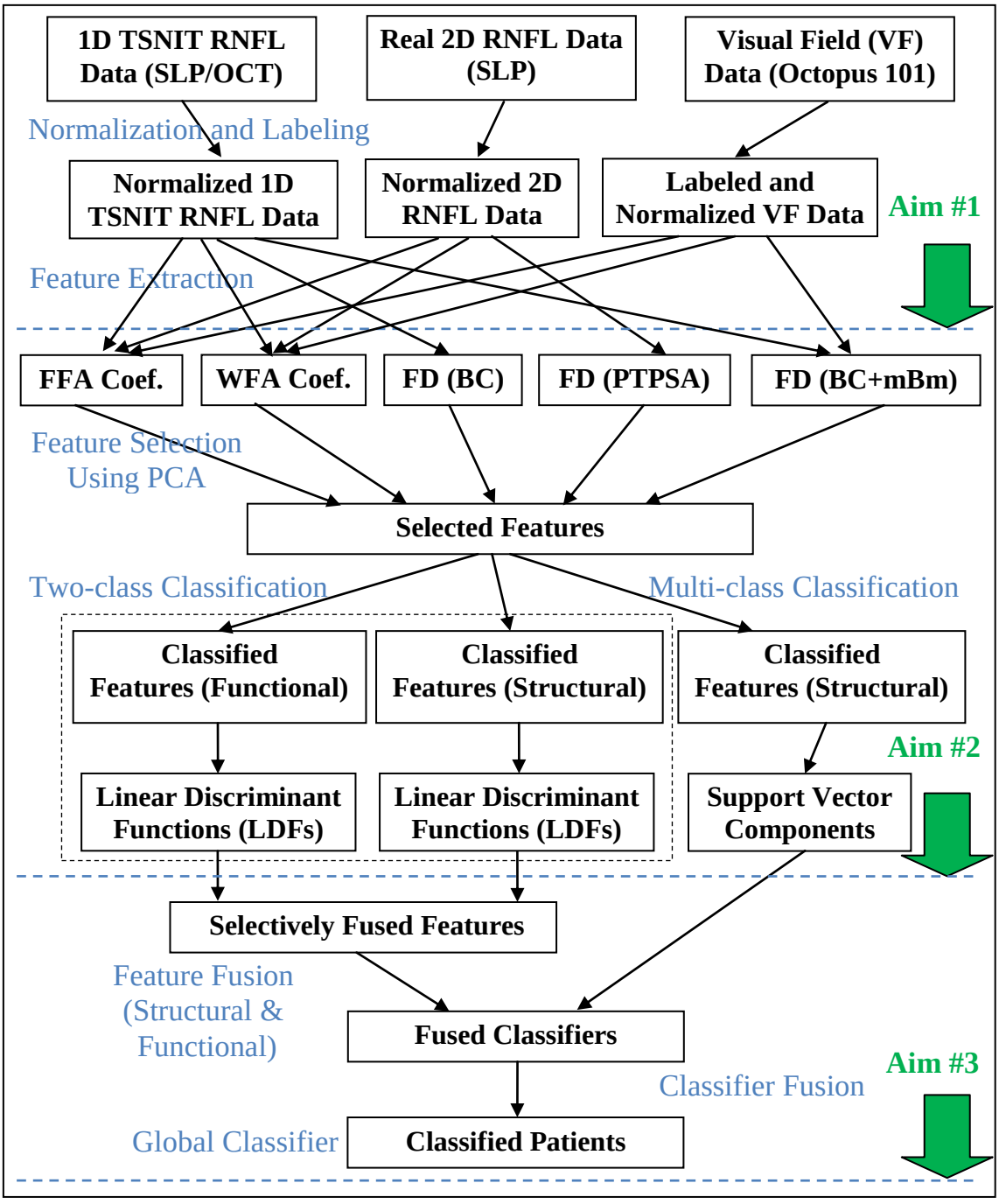

Figure 1-1. The overall flowchart of the dissertation aims

Following the above discussions, we discuss the aims of this dissertation. The overall flowchart that outlines the aims of this dissertation work is shown in Fig. 1-1. In Aim #1, we investigate the novel features such as fractal and multi-fractal for improved glaucoma detection on 1D TSNIT RNFL and real 2D RNFL data obtained from SLP and OCT. In Aim #2, we study the novel fractal/multi-fractal features and application of multi-class classification that best characterize the mechanism of glaucomatous progression in order to detect or predict the progression. In Aim #3, we investigate feature-based fusion of structural and functional data for improved glaucoma detection. This step leads to obtaining a global classifier that identifies glaucoma and predicts the progression by fusing structural and functional data. We discuss each aim below.

Aim #1: To study novel features such as fractal and multi-fractal in addition to existing FFA and WFA features extracted from 1D TNSIT RNFL and real 2D RNFL data obtained from SLP and OCT for improved glaucoma detection.

Rationale #1

As discussed before, there remain inherent challenges in extracting the representative features from the 1D TSNIT RNFL data via existing feature-based techniques such as FFA and WFA. The heterogeneous nature of glaucoma in 1D TSNIT RNFL data makes the feature-based techniques more difficult. The embedded randomness and irregularity of the RNFL damages may not be fully characterized with such analyses alone. The FA using fractal and multi-fractal features is a compact way of encoding the complexity of many natural objects. Fractal features are known to be very effective at simulating natural shapes. If the fractal dimension (FD) is in the appropriate

range, the fractal-based model begins to mimic the nature very closely. Fractal features have been investigated with local models to describe local irregularity [27]. In prior studies, fractal features have shown their effectiveness in differentiating tumor from normal brain tissues using brain magnetic resonance imaging (MRI) [24]. We have also investigated different fractal and multi-fractal feature-based techniques for brain tumor analysis and segmentation [28]. Since the malformation of biological tissues in cancerous area, which show irregularity and randomness, have been well characterized by fractal and multi-fractal features, it is reasonable to apply FA to the glaucomatous damage where irregularity and local randomness are expected to be present. Hence, it is believed that investigation to mathematical and statistical models using fractal and multi-fractal features will lead to improved glaucoma detection.

Further, it has been shown that existing feature-based techniques only adopted 1D TSNIT RNFL data, while original RNFL data are real 2D image data. No standardized method in exploiting real 2D RNFL image data has been presented and its statistical analysis has not been fully performed. In literature, a higher dimensional OCT has been experimented for discriminating glaucomatous from normal eyes with moderate success 50]. Intuitively, if we take advantage of real 2D RNFL image data where hidden irregularity may contribute to the characteristic of the disease, we may be able to achieve improved glaucoma detection. Hence, we also study the 2D fractal feature-based techniques using real 2D RNFL image data, which may provide more useful information.

Aim #2: To study novel fractal/multi-fractal features and application of multi-class classification for characterizing the mechanism of glaucomatous progression and improved progression prediction.

Rationale #2

It has been known that while analyzing a series of VF data is useful in detecting glaucomatous progression, structural changes in the RNFL often precede VF loss and that the progression may be difficult to be differentiated from the test variability of the VF test. Hence, predicting glaucomatous progression in an objective manner by assessing the progressive structural damage to the RNFL still remains challenging. It has been also shown that glaucomatous progression is multi-staged, which may require a multi-class classifier that separate a nonlinearly separable data.

A multi-class SVM classifier with a Gaussian kernel has a corresponding infinite-dimensional feature space, which is well regularized [42]. A special case of a SVM Gaussian kernel method has shown its capacity of separating nonlinearly separable input data for the multi-class classification [43]. Hence, in this work, we evaluate and compare the effectiveness of the fractal/multi-fractal features and a multi-class SVM classifier with Gaussian kernel method for best characterizing the mechanism of progressive structural changes for improved glaucomatous progression prediction.

Aim #3: To investigate feature-based selective fusion of structural (e.g., RNFL assessment) and functional (e.g., VF test) data to build a global classifier that better detects glaucoma.

Rationale #3

There are ongoing research efforts in identifying glaucoma utilizing both structural and functional measures [47-48, 51]. Additionally, it has been reported that the different procedures used in the various studies agree with each other only about 50%-60% of the time [49]. Lauande-Pimentel *et al*. proposed the creation of the integrated LDFs for both SLP and VF data. They reported higher sensitivity and specificity but their approach is simple pair-wise parameter fusion [51]. In their report, the corresponding structural and functional relationship has not been fully reflected. In this research work, we plan to investigate the effectiveness of fusing structural and functional data at the feature level exploiting known topographic correspondence between structural and functional data.

A functional analysis on VF data has been done using the total deviation (TD), mean deviation (MD) and pattern standard deviation (PSD), which are global indexes [57]. Total Deviation (TD) values represent the difference between a patient's test results and the expected age-corrected normal values at each test point in the VF. MD is obtained by averaging the TD. PSD is similar to TD, except that the values have been adjusted for any shifts (e.g., cloudy media, cataracts or small pupils). While TD, MD and PSD have been successfully utilized in differentiating glaucomatous from ocular normal patients, since they are global values, they cannot be used in a localized analysis of glaucomatous damages.

We plan to utilize a cluster-wise approach where 10 different clusters are locally analyzed, weighted and selectively fused between structural and functional data. We also explore the classification of classifier fusion utilizing AdaBoost or AdaBoostSVM so as to build a global classifier that independently identifies glaucoma and predicts the progression.

1.3. Dissertation Contributions

In this section, the novel contributions in this dissertation work are summarized. Note our contributions follow the above three research aims and are shown as follows:

1. We demonstrate that our novel fractal/multi-fractal features well represent the structural and functional changes to the 1D TSNIT RNFL and VF data where there are embedded local variation and randomness.
2. We also show that our novel fractal/multi-fractal features outperform the existing standard methods and other feature-based techniques in glaucoma detection.
3. We demonstrate that our feature-based techniques that exploit novel fractal/multi-fractal features best characterize the mechanism of multi-staged glaucomatous progression in structural data and thus prove its efficacy in comparison to the existing feature-based techniques.
4. We first introduce our novel application of multi-class SVM classification using a Gaussian kernel, which better predicts glaucomatous progression than the existing non-linear techniques such as neural networks.

5. We propose the first feature-based fusion of structural and functional data, which performs better or comparably in comparison to the standard methods and the existing feature-based techniques.

1.4. Dissertation Organization

In chapter 2, a brief description of glaucoma and glaucomatous progression is first provided. Then, the fundamentals of imaging technologies such as scanning laser polarimetry (SLP) and optical coherence tomography (OCT) are reviewed. For functional analysis, the review of visual field (VF) test is included. The feature-based techniques such as FFA, WFA and FA are generally reviewed. Then, a multi-class SVM and a Gaussian kernel method are discussed along with a feature/classifier fusion method. In chapter 3, based on the discussion in the previous sections, a detailed research work, "Identifying Glaucoma Using Fractal Features" is provided. In chapter 4, "Novel Fractal/Multi-Fractal Features and Application of Multi-class Classification for Improved Progression Prediction" is described. "Feature-based Selective Fusion of Structural and Functional Data for Improved Glaucoma Detection" is extensively discussed in chapter 5. All relevant discussions and experimental results of those works are provided in the respective chapters. Finally, chapter 6 describes the concluding remarks and future directions.

2. Background Review

2.1. Glaucoma and Progression

Glaucoma is a progressive irreversible optic neuropathy that leads to optic disc shape change, retinal nerve fiber layer (RNFL) thinning and visual field (VF) defects. According to World Health Organization (WHO), glaucoma is one of the leading causes of blindness worldwide, affecting more than 60 million people in the world and about 4 million individuals in the United States [52-54]. As humans live longer, glaucoma may affect more people and thus economic burden of society may increase.

The most common form of glaucoma, primary open angle glaucoma (POAG), is known to have an elevated intraocular pressure (IOP) causing damage to the optic nerve. The optic nerve consists of ganglion cell axons which connect to neurons in the brain. The retina, the paper-thin tissue lining in the back of the eye, has about 0.75 to 1.25 million retinal ganglion cells [55]. The axons of these ganglion cells constitute the layer termed retinal nerve fiber layer (RNFL). At a cellular level, glaucoma is characterized by a progressive and rapid death of the ganglion cells and their axons by a process of apoptosis which is measured as a progressive thinning of the RNFL. Figure 2-1 shows the cross section of the human eye which illustrates the ganglion cells and their axons of the retina [56].

Over the years, diagnosing glaucoma has involved a variety of methodologies, including measuring intraocular pressure (IOP) via tonometry, testing VF loss via standard automated perimetry (SAP), analyzing the RNFL by either scanning laser polarimetry (SLP) or optical coherence tomography (OCT), assessing optic disc changes via ophthalmoscopy, and inspecting the drainage angle via gonioscopy [57]. There are also

certain risk factors that can be useful in diagnosing glaucoma such as age, ethnic background, and medical history. However, since the exact cause of glaucoma has not been known and that POAG can impair one's vision before any signs or symptoms are apparent, it is difficult to early diagnose glaucoma with these methods only.

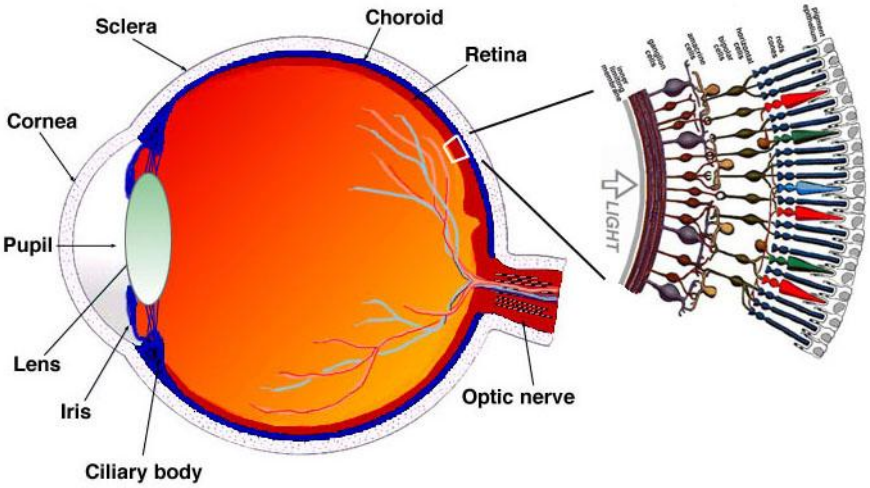

Figure 2-1. A cross section of the human eye with the enlargement of the retina [56]

Studies have shown that the RNFL can be damaged up to 50 % before the detection of the visual defect in glaucomatous patients [13]. It is also known that the structural damage such as the RNFL defect precedes functional damage up to six years before the development of VF loss [3-4, 58]. Hence, the assessment of the RNFL damage can lead to an early detection of glaucoma.

One key to the management of glaucoma involves monitoring the patient's visual status change. If an eye diagnosed as having glaucoma gets worse, it is referred to have "progressed" (a 'progressor'). If it does not progress, it remains stable and is called as a

'non-progressor' over that specific time-frame. Nevertheless, there is possibility that this eye may "progress" later. If an eye "suspected" of being at risk of glaucoma gets worse and comes to meet the definition of glaucoma, it will be defined as "converted."

While assessing a series of VF data acquired by SAP has been widely used in diagnosing glaucomatous progression, it is functional and subjective in nature, which may not fully indicate true progression in structure due to the short-term fluctuation (SF) and the long-term fluctuation (LF). SF is obtained when the pre-selected points are tested twice and the difference of the patient's responses is compared. LF is obtained by measuring the changes in threshold between VF tests. Hence, the ability to detect or predict glaucomatous progression in an objective manner still remains challenging in the management of the glaucoma.

Glaucomatous progression prediction has been an active area of research [36-38, 59-62]. Gunvant *et al*. and Essock *et al*. respectively report a feature-based technique and a LDF-based approach that achieve classification performance with moderate accuracy [36-37]. Medeiros *et al*. report eyes that are not detected as progressing by SAP may have a statistically significant decline in the GDx-VCC RNFL thickness measurement over time [38]. They propose a statistical technique to determine the progression. In [59], Medeiros *et al*. actually measure the sensitivity and specificity of OCT parameters to discriminate progressors from non-progressors. Vermeer *et al*. have presented a novel spatial coherence criterion (SCC) from GDx-VCC images for differentiating progressors from non-progressors [60]. However, they have achieved relatively low sensitivity (42%) compared with that of others [61]. Alencar *et al*. point out that the normal eyes may have different characteristics from the progressive eyes followed in clinical practice [62]. Note

that all of such works in glaucomatous progression prediction utilize the 1D TSNIT RNFL data, except Arnalich-Montiel *et al*. who take VF data as their features. Therefore, in this work, we propose a novel feature-based technique that adopts novel features such as fractal/multi-fractal and a multi-class classifier to detect and predict the progressive RNFL loss.

2.2. Structural Analysis: RNFL Thickness Measurement

2.2.1. Scanning Laser Polarimetry (SLP)

Scanning laser polarimetry (SLP) provides us with a patient's ocular structure by estimating the thickness of the peripapillary RNFL based on the birefringent property of the RNFL [4-5]. SLP utilizes a polarized light which has two orthogonal components: ordinary and extra ordinary light. The axonal microtubules of the RNFL have an organized and parallel structure. When a polarized light, an illuminated laser beam, reaches this structure of the RNFL, the phase-shift (retardation) of light occurs due to the peculiar anatomy of the RNFL, causing a change in the state of the polarized light, which is called birefringence as shown in (1). The amount of the phase-shift (retardation) is directly proportional to the thickness of the RNFL (approximately 1 degree of retardation per 7.4 μm of thickness) [5]. The amount of the phase-shift (retardation) is calculated pixel-wise and displayed in a map of the scanned area.

$$\text{Birefringence} = |n_e - n_o| \quad (1)$$

where n_e is refractive index of extraordinary and n_o is refractive index of ordinary ray.

It has been shown that the RNFL measurement by SLP needs to be compensated due to the fact that the retardation can be caused by other factors such as cornea and lens [58]. Older versions of SLP have employed a fixed compensation where both axis and magnitude reflect the median values of the general population. In the more advanced version of SLP such as GDx-VCC, however, customized anterior segment birefringence compensation (ASBC) is employed, where an initial scan of the patient's macula is adopted to perform patient-specific compensation. This enhances the discriminating power for glaucoma detection. Consequently, GDx-VCC is shown to better aid in detecting the glaucomatous defect. Figure 2-2 shows an example of scanning laser polarimeter.

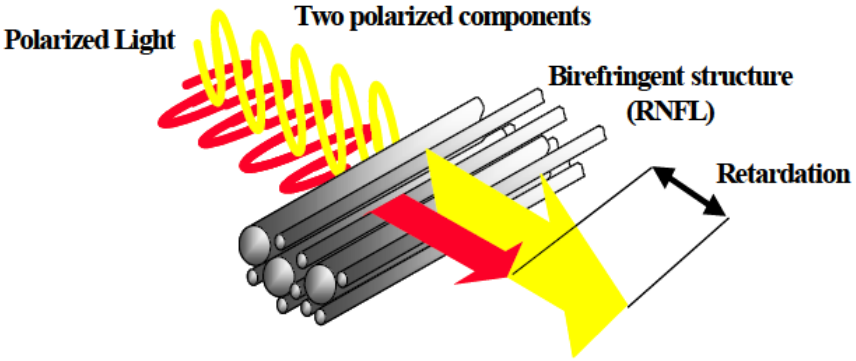

Figure 2-2. Scanning Laser Polarimeter [63]

Figure 2-3 (a) shows how a 1D TSNIT RNFL data is obtained along a circular path in the retina from GDx-VCC. Then, 64 RNFL thickness segments within an eight-

pixel-wide ring are made. These segments are grouped into the 64 sectors to yield a 1D TSNIT RNFL data in the 360° around the optic disk as shown in Fig. 2-3 (b).

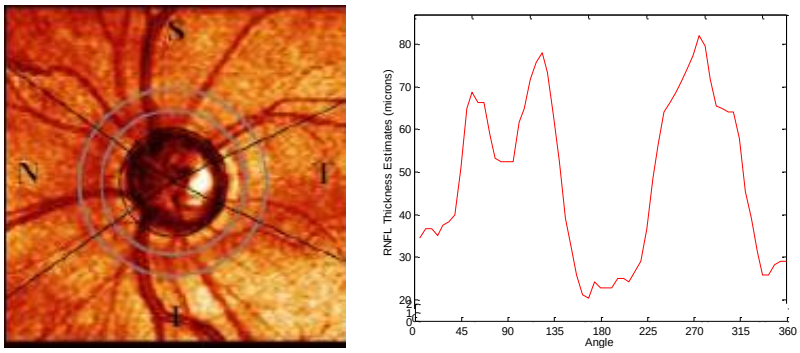

(a) (b)

Figure 2-3. (a) TSNIT RNFL measurement around the optic disc using GDx-VCC (b) The resulting 1D TSNIT RNFL with 64 sectors of thickness values in the 360°

2.2.2. Optical Coherence Tomography (OCT)

Optical coherence tomography (OCT) is a noninvasive imaging technique that obtains cross-sectional images from a series of amplitude modulation scans (A-scans) [64]. It is based on the interferometry which achieves higher resolution, deeper penetration depth and better quality images of the RNFL. First developed for the ophthalmic application, OCT has now been used for a wide variety of other medical applications such as cardiology, dermatology and neurology [65]. There are two basic approaches of using OCT: time-domain OCT (TD-OCT) and Fourier-domain OCT (FD-OCT). TD-OCT is relatively slower than FD-OCT due to the rate of the mechanical moving part that performs the A-scans. On the contrary, FD-OCT has the fixed reference arm and thus calculates the depth scan immediately using an inverse Fourier-transform from the

acquired data [66]. In this work, since we only utilize the dataset acquired by StratusOCT, which is based on TD-OCT, FD-OCT is not covered.

2.2.2.1. Time-Domain OCT (TD-OCT)

In determining ocular images, TD-OCT splits low-coherence infrared light into two separate light beams: one that travels the reference path and the other that hits the RNFL. The interferometry combines the split beams together in a way that they may result in either constructive or destructive interference between them. Since the light beam that reflects off the RNFL and the light beam that travels the reference path cause the time delay between them, this time delay is detected in the time-domain detector in the form of interference fringes. An example of a TD-OCT interferogram is shown in Fig. 2-4. Note that the light beams in phase are in constructive interference, while the light beams out of phase are in destructive interference.

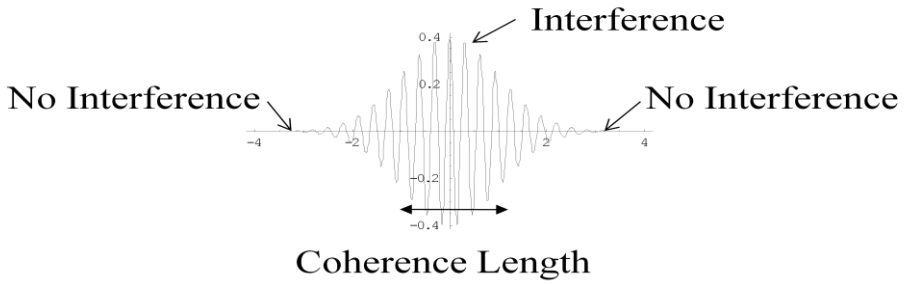

Figure 2-4. TD-OCT interferogram [67]

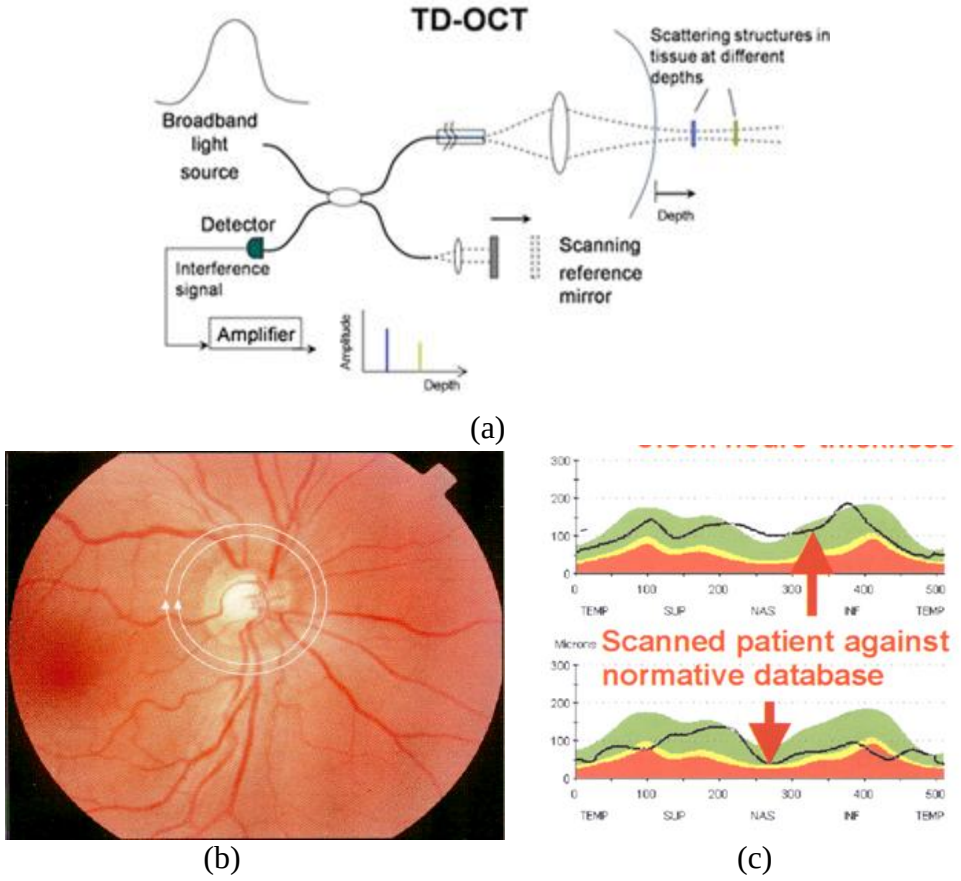

Figure 2-5. (a) The basic setup for TD-OCT (b) RNFL TSNIT measurement around the optic disc using TD-OCT (c) cross sectional RNFL TSNIT image using TD-OCT [64]

To get ocular images at different depths, TD-OCT varies the distance that the light beam travels the reference path by scanning an optical delay line. This process, known as path-length ranging, covers the interferometer with a range of light from varying depths and thus, builds a single line of the image of the sample (A-scan). This light with the receiving optics then moves to another spot to be imaged off the RNFL and the process continues, finally combining the lines of the scan and capturing the desired image (B-scan).

The light beams that TD-OCT adopts should be spatially coherent and directional. Also, they should be temporally incoherent, having many different wavelengths which provide higher resolution. In Fig. 2-5, the basic setup for a TD-OCT, a representative TSNIT RNFL data using TD-OCT, and the cross-sectional image of the RNFL using TD-OCT are shown.

2.3. Functional Analysis: Visual Field (VF) Test

A visual field (VF) is the area of the space visible by the central and peripheral vision of the immobile eyes [68]. An average VF is 60° upward, 75° downward, 60° nasally, and 90° temporally [69]. The sensitivity of a VF is the highest centrally and it steadily falls as shown in the hill of vision by Traquair in Fig. 2-6.

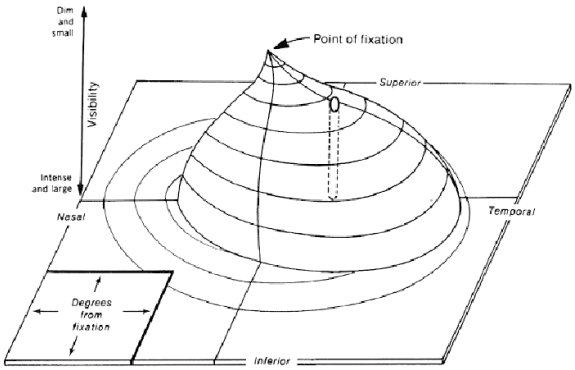

Figure 2-6. The hill of vision by Traquair [70]

The VF test is an important part of diagnosing and managing of glaucoma. The VF test measures the patients' visual sensitivity via evaluating the ability of detecting points of light centrally and peripherally. Since patients may not recognize the VF defects

until the symptoms or signs of peripheral vision loss are obvious, the VF test can help early detect such defects. There is a list of techniques for visual field test: confrontation visual field exam, Goldmann field exam and automated perimetry [71]. However, automated perimetry devices such as Humphrey Field Analyzer (HFA) and Octopus perimeter have replaced manual perimetry such as Goldmann field exam. Fig. 2-7 shows a HFA and an Octopus perimeter [72-73].

Automated static perimetry (ASP), also called standard automated perimetry (SAP), uses stationary white light stimuli at fixed locations onto a white background, gradually increasing in their intensity or size until the stimuli are perceived. SAP can be performed in an objective and standardized fashion with minimal bias using pseudorandom light stimulus presentation. With SAP, the reliability and speed of the VF test are increased [74-75]. The visibility at the fixed locations is measured using the threshold values of various intensities. The test is done one eye at a time and the patient is to response to light sensation. The luminance of the test targets is measured in apostilbs, where an apostilb (asb) is an absolute unit of luminance, being the luminance of a perfectly diffusing surface emitting light at the rate of π^{-1} (i.e., 0.3183) candela/m^2 or 0.1 mililambert. Then, the threshold values are recorded in the decibel (dB) scale, where zero dB is denoted as the brightest stimulus while the greatest dB is the dimmest stimulus.

(a) (b)

Figure 2-7. (a) Humphrey Field Analyzer (HFA) [71] (b) Octopus perimeter [73]

If the initial light stimulus is not perceived, then the intensity of light stimulus is increased 4 dB each time until it can be seen. Next, the intensity is decreased 4 dB each time until it cannot be seen. Then, it is increased again 2 dB at a time until it can be seen again. This process is called a 4-2 staircase bracketing strategy. The threshold values are estimated as the intensities of the last seen stimuli (Humphrey) or the average values of the last seen and unseen stimuli (Octopus). Hence, these threshold values are used to determine the visual sensitivity of any given location. Normally, the patients with good peripheral vision detect very dim light stimuli. Hence, the dimmer the stimuli, the higher the threshold values are obtained and the higher the number on the VF map, then, the better the patient has performed on the test.

For the reliable VF test, the number of fixation losses and false positive and negative errors should be small [75]. Fixation losses are the number of times a patient is detected to be looking at the wrong spot. During the test, light stimuli are shown to the patient's blind spot, and if the patient responds to these stimuli, it is regarded as a fixation loss. To be considered a reliable test, fixation losses should be less than 15%. Another

indicator for reliability is the number of false positive or false negative errors. If the patient responds to the noise of the machine and not to the actual light stimulus, it is registered as a false positive error. In contrast, false negative errors are recorded when the patient could not see a bright stimulus in the same spot they previously detected a dim stimulus. For a reliable test, these false positive and negative should be less than 15%.

2.3.1. Octopus Perimeter

Octopus 101 perimeter has been extensively used in everyday practice, clinical studies and research work [76]. It is a separate unit remotely controlled by a computer hardware and via the PeriTrend software. All Octopus 101 test results can be exported to the latest EyeSuite Perimetry software and evaluated further. Octopus 101 perimeter features a spherical cupola with direct projection for 90° full field static and kinetic perimetry. For eye monitoring, infrared sensitive eye camera is used. There are 14 diagnostic examination programs and the test strategies include normal 4-2-1dB, low vision, dynamic and qualitative 3-zone.

2.4. Feature Extraction Techniques

Features are individual measurable heuristic properties of the phenomenon of interest being observed [77]. Feature extraction is the key to any pattern recognition method, particularly for the purpose of classification. Since the 1D TSNIT RNFL data show unique double-hump patterns, their shape as features in average (e.g., TSNIT Average, Superior Average and Inferior Average) have been used for classifying glaucomatous from normal eyes. At the same time, such double-hump pattern data have

been passed through feature-based techniques (e.g., FFA, WFA and FA), which parameterize the unique shape of the 1D TSNIT RNFL data, for better classification performance. In these procedures, all the double-hump pattern data have been treated as 1D data. We review the background of the existing feature extraction techniques such as FFA and WFA along with the newer technique, FA, below.

2.4.1. Fast-Fourier Analysis (FFA)

From a statistical point of view, a signal is regarded as an array of intensity values with locally varying statistics [77]. Fast-Fourier analysis (FFA) breaks down this statistically varying signal into the elements of sinusoids of different frequencies so that it may transform the given signal from a time domain to a frequency domain [78]. This concept of the FFA heavily depends on the type of a signal. If a signal does not change much over time, that is, a stationary signal, transforming the signal from a time domain to a frequency domain using the FFA does not make any significant difference. However, most interesting signals contain numerous non-stationary or transitory characteristics such as drift, trends, abrupt changes, discontinuities, and beginnings and ends of events. Hence, the FFA is useful where the valuable information of the signal's frequency is intended to be obtained and utilized.

Mathematically, the process of the FFA is represented by the Fourier transform [78]. It is the sum over all time of a signal, multiplied by a complex exponential. In actual computer simulation, the Fourier transform is done in a discrete manner, yielding the discrete Fourier coefficients. Hence, the discrete Fourier transform (DFT) is utilized by the equation below:

$$F(\omega) = \frac{1}{M} \sum_{t=1}^{M-1} f(t) e^{-jw\frac{t}{M}} \qquad \text{for } \omega = 0, 1, 2, M\text{-}1 \qquad (2)$$

where $F(\omega)$ are the discrete Fourier coefficients, M is the total number of input points and $f(t)$ is the input signal.

For the faster calculation of the discrete Fourier transform, the fast Fourier transform (FFT) is implemented and thus achieves the same results more quickly. Using these fast Fourier coefficients, the fast-Fourier analysis (FFA) is done. Since the FFA better captures discontinuities and abrupt changes in a non-stationary signal and thus shows more robustness than the methods that only emphasize the average values, the FFA is suited for analyzing the 1D TSNIT RNFL data where abrupt changes and discontinuities are expected to be present.

2.4.2. Wavelet-Fourier Analysis (WFA)

While the FFA is a good candidate for analyzing a non-stationary signal such as the 1D TSNIT RNFL data, it has a few drawbacks. In transforming to the frequency domain in FFA, non-periodic local information is lost. The wavelet analysis can overcome such a drawback by revealing the hidden aspects such as breakdown points, discontinuities in higher derivatives, and self-similarity [79]. The wavelet analysis analyzes a localized area of a larger signal using flexible wavelets. Comparing wavelets in the wavelet analysis with the sinusoidal waves of the FFA, it has been known that wavelets are more irregular and asymmetric with limited spatial duration [80]. For many signals, the low-frequency content is the most important part, providing the signal with its identity.

The high-frequency content, on the other hand, imparts unique characteristics. These two processes constitute so called wavelet decomposition. In the wavelet analysis, a function is decomposed by wavelet $\psi(x)$ and scaling function $\varphi(x)$ given as,

$$f(x) = \sum_k c_{j_0}(k)\varphi_{j_0,k}(x) + \sum_{j=j_0}^{\infty}\sum_k d_j(k)\psi_{j,k}(x) \quad . \tag{3}$$

where j_0 is an arbitrary starting scale, the $c_{j0}(k)$'s are approximation coefficients and the $d_j(k)$'s are detail coefficients [78, 81]. Like the way the FFA is represented by the Fourier transform, the wavelet analysis is represented by the wavelet transform. For a discrete function, the discrete wavelet transform (DWT) is used, using the DWT transform pair, shown below.

$$W_\varphi(j_0,k) = \frac{1}{\sqrt{M}}\sum_x f(x)\varphi_{j_0,k}(x) \quad ; \tag{4}$$

$$W_\psi(j,k) = \frac{1}{\sqrt{M}}\sum_x f(x)\psi_{j,k}(x) \quad ; \tag{5}$$

and,

$$f(x) = \frac{1}{\sqrt{M}}\sum_k W_\varphi(j_0,k)\varphi_{j_0,k}(x) + \frac{1}{\sqrt{M}}\sum_{j=j_0}^{\infty}\sum_k W_\psi(j,k)\psi_{j,k}(x) \quad . \tag{6}$$

where $W_{\varphi}(j_0,k)$'s and $W_{\psi}(j,k)$'s in (4) to (5) correspond to the approximation coefficients and detail coefficients, respectively in the discrete domain and M is the total number of input points.

There have been attempts to combine the FFA with the wavelet analysis known as the wavelet-Fourier analysis (WFA) for obtaining better performance [23]. Firstly, the DWT is applied to the 1D TSNIT RNFL data yielding the approximation and the detail coefficients, where the former contains down-sampled spatial information, and the latter contains detailed information. The DWT is then applied to the approximation coefficients and the results of this second-level transformation are retained. The detail coefficients are further processed using FFT to obtain more useful high frequency information. This process is repeated based on the pre-determined scales so as to maximize the performance. In this process, only the amplitude values are retained.

2.4.3. Fractal Analysis (FA)

It has been known that many signals and images with smooth curves and surfaces can be analyzed through classical geometries such as Euclidean geometry where shape, size and relative position are addressed. However, there are numerous natural phenomena which cannot be described using the classical geometries due to their complexity and irregularity. They are better represented via a different geometrical representation such as fractal analysis (FA) [82].

A fractal is a scale-invariant entity with embedded irregularity and complexity, which can be found everywhere in nature such as clouds, mountain ranges, coastlines, vegetables, snowflakes, and bacteria [83-85]. A fractal is a rough or fragmented geometric

object with an infinite nesting of structure at all scales. Each fractal is a reduced-size copy of the whole, which accounts for the localized variation. A fractal typically has unique properties, such as self-similarity, chaos, and non-integer fractal dimension (FD). Self-similarity implies that any portion of the fractal object appears identical to the whole object. Chaos symbolizes the unpredictability of the fractal object. Non-integer fractal dimension (FD) represents the quantitative measurement of the fractal object.

A topological dimension is known to characterize an object of interest with different units of measurements. However, a topological dimension may not fully describe the morphology of a complex object such as a fractal object. For example, a straight line has a topological dimension of one in Euclidean geometry (e.g., 1D, 2D and 3D), but a complex line such as a coastal line has a topological dimension between one and two, which is between a straight line and a plane. The FA well describes such an object and has shown much success in 1D signal and 2D image processing [85-86]. Even when the considered 1D or 2D data are not strictly fractal object, the FA can be still applied for the embedded irregularity and complexity in such data can be utilized as useful information. For the FA, FD is measured, which is the approximation of Hausdorff dimension. There are several methods in estimating the FD such as box-counting (BC) method and multi-fractional Brownian motion (mBm) method. We briefly discuss such methods below.

2.4.3.1. FD Estimation Using BC Method

The first technique involves obtaining the FD features using a BC method. Using the pseudo 2D image of the 1D TSNIT RNFL data, a BC method calculates the FD

features for each size of the boxes by dividing 2D image into the boxes of predetermined size, "*r*," and counting the number of the occupied boxes, "*N*," needed to capture the signal values. The resulting FD features are the ratios between the logarithmic values of *N* and *1/r*. The expression of pseudo 2-dimension FA is as follows:

$$FD = \lim_{r \to 0^{0+}} \frac{\ln(number\ of\ \ self - similar\ \ pieces, N)}{\ln(magnification\ \ factor, \frac{1}{r})} \quad . \qquad (7)$$

Since the 1D TSINT RNFL data have been extracted from the 2D TSNIT RNFL thickness profiles, it may be reasonable to convert such a 1D data into a pseudo 2D image using *y*-coordinate as the index. Such a 2D pseudo image representation of 1D TSINT RNFL data is then amenable to a BC method without losing any generality of the 1D TSNIT RNFL thickness measurement values.

2.4.3.2. FD Estimation Using mBm Method

A fractional Brownian motion (fBm) model is a non-stationary and zero-mean Gaussian process and has been commonly used for medical imaging applications such as brain tumor segmentation and prediction [31]. This fBm model is known to well characterize a random phenomenon and is based on self-affine fractal Brownian functions (fBfs). Hence, an fBm model is defined as follows:

$$B_H(t) - B_H(s) = \frac{1}{\Gamma(H+0.5)} \left\{ \int_{-\infty}^{0} \left[(t-s)^{H-0.5} - s^{H-0.5} \right] dB(s) + \int_{-\infty}^{0} (t-s)^{H-0.5} dB(s) \right\}. \quad (8)$$

where H is the Holder exponent, s and t are different observation times of the process, and B_H is a generalization of Brownian motion. The Holder exponent is a measure of the roughness of the object of interest. Then, the FD of an fBm model is defined as follows:

$$FD_{fBm} = n + 1 - H. \quad (9)$$

where n is Euclidean dimension of the space.

Although an fBm model has proved to be useful in quantifying the random phenomenon such as brain tumor texture, it appears to be homogeneous or mono-fractal. It has been reported that there exists multi-fractal structure in real world entities such as tumor regions in MRI [29, 86-88]. Hence, multi-fractional Brownian motion (mBm) model may be more suitable for characterizing the RNFL data. The mBm is defined as,

$$x(at) = a^{H(t)} x(t). \quad (10)$$

where $H(t)$ is the time varying Holder exponent, $x(t)$ is a random process and a is the scaling factor. After a mathematical derivation, the expectation of the squared-magnitude of the wavelet transform W_x of $x(t)$ is,

$$\log\left(E\left[|W_x(a,t)|^2\right]\right) = (2H(t)+1)\log a + C. \quad (11)$$

where C is a constant. Then, $H(t)$ can be approximated as follows :

$$2H(t) = \lim_{a\to 0+} \frac{\log\left(\frac{1}{N}\sum_{i=0}^{N-1}|W_x(a,t)|^2\right)}{\log a}. \quad (12)$$

Finally, we compute the FD using Eq. (9) as follows:

$$FD_{mBm} = n+1-H(t). \quad (13)$$

2.5. Feature Selection

After the original data are normalized and passed through the feature extraction techniques for obtaining the better representative features of the original data, the next step involves feature selection [89]. Generally speaking, selecting more features out of all available features results in better classification performance. However, selecting more features means more computational burden and some features are redundant or irrelevant on our specific purposes. Hence, care must be given to this step of feature selection for the best performance.

Principal component analysis (PCA) has been commonly used as a feature selection method in the machine learning area for its feature compression capability. More details of feature selection will be discussed below.

2.5.1. Principal Component Analysis (PCA)

Principal component analysis (PCA) projects a given feature dataset $X = [x_1, x_2, \ldots, x_n]^T$ with n variables into a new feature set $Y = [y_1, y_2, \ldots, y_m]^T$ with m variables so that most of the variability of the dataset is contained within the first few combinations [90]. It essentially transforms a given feature dataset with correlated variables into a smaller sized feature dataset with uncorrelated variables, which are called the principal components (PCs), such that $m < n$. The first principal component (PC) is the projection of the data points in the direction of the line giving the best orthogonal regression fit to the data points. Since the best fit to this type should pass through the mean, the data points are centered on the mean by subtracting the mean from the data points. The first principal component (PC) is hence the projection of the data points into the direction with maximal variance of the projected points. The first principal component (PC) corresponds to the maximum variability of the original feature set and the second PC corresponds to the second highest variability of the set and so forth. The PCA transformation is then given as:

$$Y = W(X - m_x) \text{ or } (X - m_x) = AY \tag{14}$$

where m_x is the mean of X, W is a unmixing matrix and A is a mixing matrix.

The first step in PCA is to find the sample covariance matrix C_x for the combined samples of both classes (in the present study, glaucomatous and normal eyes). Then, the eigenvalues and the corresponding eigenvectors of the matrix are computed by using the equation given as:

$$(C_x - \lambda I)a_i = 0 \qquad (15)$$

where C_x is a covariance matrix, λ is an eigenvalue and a_i is a mixing vector.

The combination of the feature points that has the maximum variability is obtained in the direction of the first principal component and this direction is that of the eigenvector corresponding to the highest eigenvalues. Hence, the eigenvalues are ordered from the highest to the lowest and the ordered eigenvectors represent the principal component (PC) directions. After the covariance matrix is calculated, the transformation matrix is then extracted from this matrix by taking only the selected number of eigenvectors according to such number of eigenvalues (feature selection). Finally, the new transformation matrix is then used to derive the new compressed feature vector set.

2.5.2. Fisher's Linear Discriminant Analysis (LDA)

After feature selection is performed, the final classification is performed. For two-class classification, the classifier is generated by using two subsets–the training and the testing set. K-fold cross validation and Fisher's linear discriminant analysis (LDA) have

been commonly used for this task. Using the training set, the classifier is formulated, and the testing set is used to assess the stability of the classifier (k different times). Fisher's LDA classifier is used to maximize the ratio of the between-class scatter to the within-class scatter in lower dimensional space than input feature dataset. This ratio is the foundation of the classifier that optimally separates two pre-determined categories (in the present study: glaucomatous and normal eyes). The first step in Fisher's LDA is to find three mean values: the mean of glaucomatous group, the mean of normal eyes group and the mean of the combined group. These mean values are used to find the between-group and within-group variability. If we define each group's mean values as vectors, the corresponding mean vectors can be given as:

$$\boldsymbol{\mu}_i = \frac{1}{n_i}\sum_{j=1}^{n_i}\mathbf{x}_{ij} \ , i = 1,2 \tag{16}$$

where n_i is the corresponding size of the groups.

Also, the overall mean vector will be given as:

$$\boldsymbol{\mu} = \frac{\sum_{i=1}^{2} n_i \boldsymbol{\mu}_i}{\sum_{i=1}^{2} n_i}, \ i = 1, 2 \tag{17}$$

Next, we obtain the scatter matrices. The between-group scatter matrix is given as:

$$S_B = n_i \sum_{i=1}^{2} (\boldsymbol{\mu}_i - \boldsymbol{\mu})(\boldsymbol{\mu}_i - \boldsymbol{\mu})^T \tag{18}$$

The within-group scatter matrix is given as:

$$S_W = \sum_{i=1}^{2} (n_i - 1) \sum_{i=1}^{2} \sum_{j=1}^{n_i} (\mathbf{x}_{ij} - \boldsymbol{\mu}_i)(\mathbf{x}_{ij} - \boldsymbol{\mu}_i)^T \tag{19}$$

Fisher's LDA finds a coefficient vector **q** that maximize the ratio of the between-group scatter matrix to the within-group scatter matrix, given as:

$$\mathbf{q}_{opt} = \arg\max_{\mathbf{q}} \left| \frac{\mathbf{q}^T S_B \mathbf{q}}{\mathbf{q}^T S_W \mathbf{q}} \right|, \tag{20}$$

and

$$S_B \, \mathbf{q} = \boldsymbol{\lambda} S_W \, \mathbf{q} \tag{21}$$

where $\boldsymbol{\lambda}$ is an eigenvalue vector.

Then we obtain the eigenvectors by solving

$$(S_B - \lambda S_W)\,\mathbf{q} = 0 \tag{22}$$

and using a single threshold (linear discriminant), the input data can be categorized into two groups.

2.6. Multi-class Classification Using Support Vector Machine (SVM)

2.6.1. Basic SVM

Support vector machine (SVM) has been used in classification problems with the application to the pattern recognition and machine learning [39]. SVM works by finding the hyperplane that separates the two classes, while providing the widest margin. The SVM assumes a training dataset D = $\{x_i , y_i\}_{i=1,2}$ where $y_i \in \{-1,1\}$. This dataset can be separated by a hyperplane, $\mathbf{w}^T \cdot \mathbf{x} + b = 0$ with a small error. The distance between the hyperplane and support vector for each group is the reciprocal of the norm of the weight, such as, $1/\|\mathbf{w}\|$ and the distance between two groups is its double, that is, $2/\|\mathbf{w}\|$. In order to maximize the margin, we need to minimize $\|\mathbf{w}\|$ with the constraint condition given as,

$$\mathbf{y} \mid \mathbf{w}^T \cdot \mathbf{x} + b \mid \geq 1, \tag{23}$$

where **w** is a normal vector that contains weight parameters and b is a constant.
Then, it is an optimization problem and using the Lagrangian with a loose variable and a penalty factor α, it can be described as:

$$L = \frac{1}{2}\|w\|^2 - \sum_i \alpha_i (y_i (w^T x_i + b) - 1) \qquad \alpha_i \geq 0 \quad \forall i \tag{24}$$

By setting the derivative of the Lagrangian to be zero, the optimization problem can be written in terms of α_i as shown below.

$$\max W(\alpha) = \sum_{i=1}^{n} \alpha_i - \frac{1}{2} \sum_{i,j} \alpha_i \alpha_j y_i y_j x_i^T x_j \qquad \alpha_i \geq 0, \quad \sum_{i=1}^{n} \alpha_i y_i = 0, \forall i \tag{25}$$

where x is an input dataset, y is an output dataset, α is a penalty factor and W is a weight parameter vector. The unknown parameter vector **w** can be recovered by

$$\mathbf{w} = \sum_{i=1}^{n} \alpha_i y_i x_i \tag{26}$$

For testing, the testing dataset **z** is classified as class +1 if the decision function, f, is greater than 0, and as class -1 if f is less than 0.

$$f = \mathbf{w}^T \mathbf{z} + b = \sum_{i=1}^{n} \alpha_i y_i \mathbf{x}_i^T \mathbf{z} + b \tag{27}$$

where **x** is an input dataset, *y* is an output dataset, **z** is a testing dataset, α is a penalty factor and **w** is a weight parameter vector.

2.6.2. Kernel Function

SVM is a linear classifier which cannot deal with nonlinearly separable data. One solution to this issue is to map the nonlinearly separable data into a high dimensional feature space so that a linear classifier can be applied. For our multi-class classification, the data distribution is normally perceived as nonlinear. Hence, we propose to use a kernel based SVM for multi-class classification in this work.

Equation (26) shows that the data points appear as inner product. Consequently, as long as the inner product in the feature space can be calculated, the mapping does not need to be explicitly addressed. Many common geometric operations such as angles and distances can be expressed by inner products. According to Mercer's theorem, if a kernel function, *K*, is semi-positive definite and symmetric, then there exists mapping with the inner product given as,

$$K(x_i, x_j) = \langle \mathbf{\Lambda}(x_i),\ \mathbf{\Lambda}(x_j) \rangle \tag{28}$$

where x is an input dataset and $\mathbf{\Lambda}$ is an implicit mapping of the input dataset into a high-dimensional feature space.

It is known that the dimensionality of the kernel-induced feature space is not necessarily important. With the kernel function shown above, Eq. (25) can be rewritten by

$$\max W(\alpha) = \sum_{i=1}^{n} \alpha_i - \frac{1}{2} \sum_{i,j} \alpha_i \alpha_j y_i y_j K(x_i, x_j) \qquad \alpha_i \geq 0, \quad \sum_{i=1}^{n} \alpha_i y_i = 0, \forall i \,. \tag{29}$$

where x is an input dataset, y is an output dataset, α is a penalty factor, K is a kernel function and W is a weight parameter vector.

In addition, the set of kernels is closed under some operations such as addition and scaling. It is known that any complex kernel can be made from simple ones by Eq. (28), which is called modularity. In this work, we use the Gaussian kernel, which is a form of radial basis function kernel.

$$K(x_i, x_j) = \exp(-\|x_i - x_j\|^2/(2\sigma^2)). \tag{30}$$

where K is a kernel function and σ is a tuning parameter.

In this Gaussian kernel function, the tuning parameter, σ, plays an important role in the performance of the kernel. If σ is overestimated, the exponential will behave as a linear function and thus the kernel function will lose its nonlinear power. If σ is underestimated, the kernel function will lack regularization and the decision boundary will be highly sensitive to noise in training data.

2.6.3. Multi-class SVM

A multi-class SVM classifier can be obtained by training several classifiers and combining their results [40]. There are several strategies for combining SVM classifiers. Out of such strategies, two common methods are "one-against-one (OAO)" and "one-against-all (OAA)" [40]. The OAO involves training one classifier for each class to discriminate that class from the other classes. Out of possible pairs of *N* classes, each classifier defines a discrimination function which assumes positive values when the cases belong to the class and otherwise, negative values. These values are then compared and the output of the combined classifier is the matching index for which the value of the discriminating function is the largest. The most commonly used discrimination function is the signed distance between the case to classify and the hyperplane. In OAO method, the required number of classifiers is $N(N\text{-}1)/2$. In the OAA method, however, only *N* two-class classifiers are needed, since the *N* class problem is broken down to a series of two-class problems. Hence, in this work, we use the OAA method which requires one less classifier. At each class, its classifier is trained on the whole training dataset so as to classify the members of class against the rest. Hence, the j^{th} classifier or the decision function, *g*, solves the following problem, similar to the two-class case:

$$\min_{w_i,b_i,\xi_i} \frac{1}{2}\|w_i\|^2 + C\sum_j \xi_i^j ; where\ \ \xi_i^j \geq 0,\ j = 1,..., l \quad \forall j \ ;$$

$$\begin{aligned} & g^j = \mathbf{w}_i^T \mathbf{\Lambda}(\mathbf{x}^j) + b_i \geq 1 - \xi_i^j, \quad if\ \ y^j = i\,; \\ & g^j = \mathbf{w}_i^T \mathbf{\Lambda}(\mathbf{x}^j) + b_i \leq -1 + \xi_i^j, \quad if\ \ y^j \neq i\,; \\ & \text{and,} \quad \xi_i^j \geq 0,\ j = 1,\ldots,l\,. \end{aligned} \tag{31}$$

where the training data $\mathbf{x}^j$ are mapped into a higher dimensional space by a kernel function $\mathbf{\Lambda}$, $\mathbf{w}$ is a weight parameter vector, C is a penalty parameter and ξ_i^j are slack variables.

The role of the penalty term in (31), $C\sum_j \xi_i^j$, is to reduce the training errors. After solving (29), there are k decision functions and the test dataset is labeled as the j^{th} class with the largest value of decision function, which shows that the classifier with highest confidence score is estimated as the labeled class. Hence, the expression for estimating the class using multi-class SVM is given as,

$$x \text{ as } j^{th} class = \arg\max_{i=1,\ldots,k} (\mathbf{w}_i^T \mathbf{\Lambda}(\mathbf{x}^j) + b_i) \cdot \tag{32}$$

where $\mathbf{x}^j$ are the training dataset, $\mathbf{\Lambda}$ is a kernel function, $\mathbf{w}$ is a weight parameter vector and b is a constant.

2.7. Feature-based Fusion

Feature-based fusion has been adopted as a new technique that achieves improvement in the classification performance [44-45]. In this work, we mainly focus on discovering the relationship between the structural and functional data so as to obtain the best possible selective feature fusion. Further, we explore AdaBoost and AdaBoostSVM for classifier fusion.

2.7.1. AdaBoost

Considering the heterogeneous nature of the features in glaucoma, boosting is expected to improve classification performance. In boosting, each component classifier is successively added and trained on a subset of the training data that is "most informative," given the current set of component classifiers already added to the ensemble of the classifiers. After the training procedure is finished, prediction on the new testing data is made based on the voting of the component classifiers, which are weak learners.

Among various types of boosting, adaptive boosting (AdaBoost) has been commonly used, which we will utilize. AdaBoost keeps adding the weak learners until the pre-determined low training error has been achieved. During the training of the classifiers, a weight is assigned to each sample that determines its probability of being selected in the training set for the next component classifier. If a training sample is correctly classified by the current ensemble of the classifiers, its probability of being selected in the training set of the subsequent weak learner is reduced. However, if the training sample is not correctly classified, its weight is increased. The new distribution of the weight is used to select the training set for the next iteration of training a new component classifier. Thus, AdaBoost selectively focuses on the informative samples. Predictions of the new testing data are made based on the weighted votes of the weak learners. The classifier weights are calculated based on their individual performance on classification.

2.7.2. AdaBoost Support Vector Machine (SVM)

AdaBoostSVM is a relatively new method of enhancing classification performance, which combines AdaBoost and SVM. This method gives promising results with other classifier fusion methods. We will explore the possibility of developing a new algorithm for this approach.

3. Identifying Glaucoma Using Fractal Features

3.1. Introduction

The glaucomatous damage to the retinal nerve fiber layer (RNFL) often precedes visual field (VF) defect. Therefore, assessing the RNFL using imaging technologies such as SLP and OCT can provide clinically more useful information than VF test in identifying glaucoma and monitoring glaucomatous changes. However, detecting early stage of glaucoma using only SLP and OCT may not be sufficient due to considerable inter-individual variation in the RNFL, caused by different physiological aging process and the heterogeneous nature of the glaucoma [4]. Feature-based techniques such as FFA and WFA have shown superior performance to the standard machine classifiers in identifying glaucoma owing to their ability of extracting the better features from the 1D TSNIT RNFL data.

Recently, fractal-based techniques have demonstrated considerable potential in medical imaging applications such as brain tumor segmentation using brain multimodal MRI. The key element of such fractal-based techniques is determining fractal dimensions (FDs) which well characterize irregularity and randomness embedded in natural phenomena such as the cancerous deformation in biological tissues. Hence, it is reasonable to apply fractal-based techniques to 1D TSNIT RNFL data wherein irregularity and local randomness are expected to be present. Consequently, we exploit the fractal-based techniques for identifying early stage of glaucoma.

In this work, we apply our novel fractal-based techniques on both SLP (GDx-VCC) and OCT (StratusOCT) data. For SLP, 1D TSNIT RNFL data has been obtained via GDx-VCC for randomly selected patients (227 study participants: 116 glaucoma and

111 ocular normal patients). Then, a mono-fractal BC method is utilized, which takes pseudo 2D images from 1D TSNIT RNFL data. For OCT, a multi-fractional Brownian motion (mBm) method is used, which incorporates both fractal and wavelet analyses, to analyze the dataset obtained from StratusOCT (136 study participants: 63 glaucoma and 73 ocular normal eyes).

The rest of the chapter is organized as follows. In section 3.2, the detail methods of our novel fractal-based techniques for identifying glaucoma using SLP and OCT data are provided. Section 3.3 presents the experimental results, performance evaluation of our novel fractal-based techniques and relevant discussions. Finally, conclusion is given in section 3.4.

3.2. Methods

Figure 3-1 shows the flowcharts of our fractal-based techniques for SLP and OCT data. In Fig. 3-1, the first step for both SLP and OCT data involves converting 1D TSNIT RNFL data into pseudo 2D images. We discuss pseudo 2D image generation later. A mono-fractal BC method is applied next on SLP data while a multi-fractal mBm method as well as a BC method are applied on OCT data respectively.

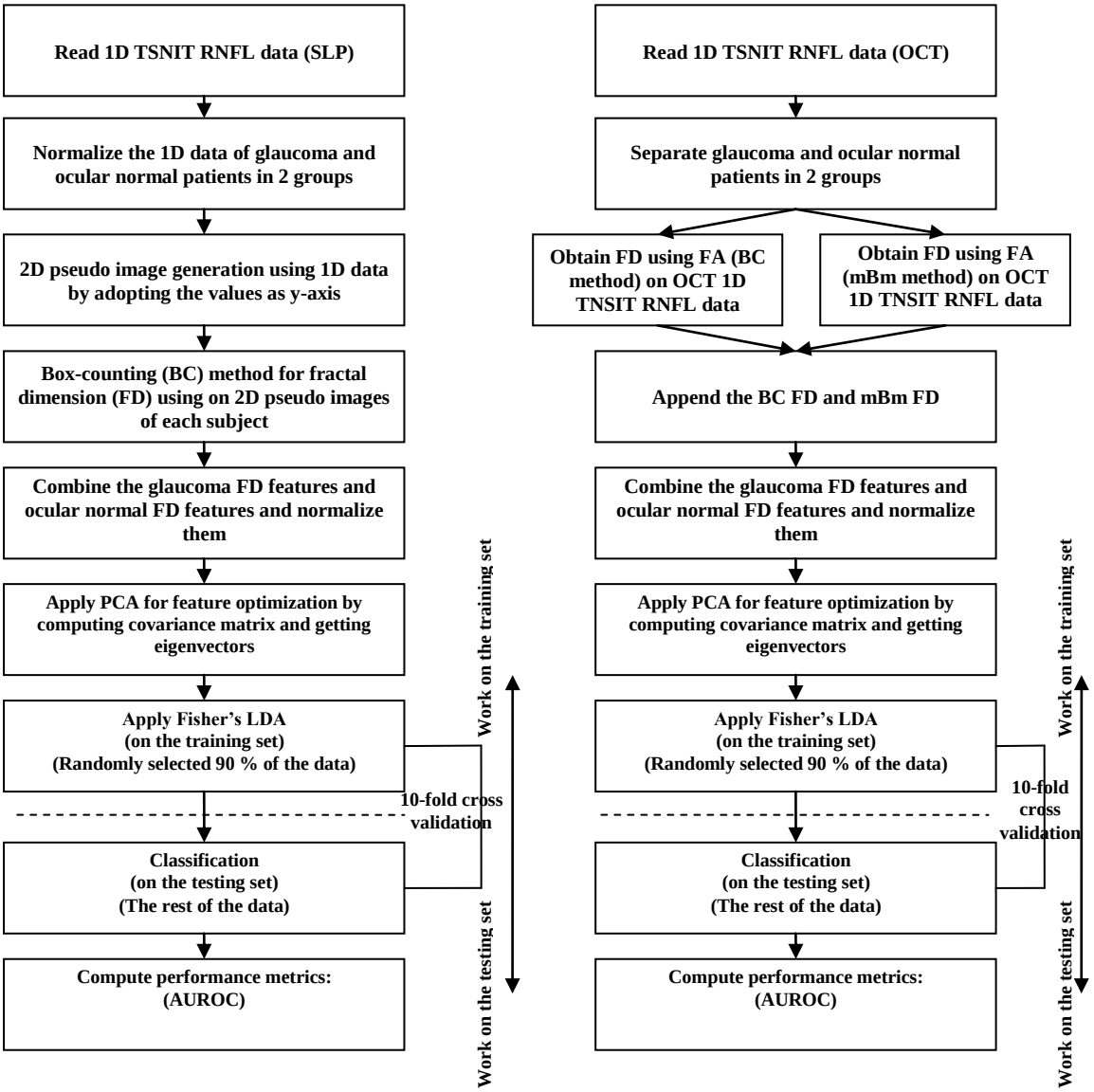

Figure 3-1. The flowchart of the proposed fractal-based techniques for (a) SLP (GDx-VCC) data (b) OCT (StratusOCT) data

The resulting FD features are then normalized and are further processed by using PCA for data reduction. Finally, Fisher's LDA classifier is used for classification of the reduced dimensionality data. A 10-fold cross validation is also used where 90% of the data are selected for training and the remaining 10% is applied for testing. For SLP data,

the sensitivity, specificity and AUROC are calculated and compared with those of FFA and WFA to identify glaucoma from ocular normal individuals. For OCT data, the same metrics as above are also calculated along with those of standard machine output of Inferior Average, Superior Average and Average RNFL thickness. Comparison of AUROC was performed using the DeLong *et al*. technique [91].

3.2.1. Acquiring 1D TSNIT RNFL Data

Figure 3-2 (a) shows the RNFL thickness measurement obtained along a circular path in the retina from a scanning laser polarimeter (GDx-VCC). The obtained RNFL thickness measurement are grouped into 64 sectors to yield a 1D TSNIT RNFL data of 64 points in the 360° around the optic disk as shown in Fig. 3-2 (b).

For SLP data, the dataset includes 116 glaucomatous and 111 ocular normal subjects (85 males and 142 female), randomly selected for only one eye of each subject. The mean age of glaucomatous and ocular normal subjects was 57.9 and 56.1 years respectively. The groups are matched for age and the difference in age between the ocular normal subjects and glaucoma patients was not significant (Independent samples t-test t = -1.08, p = 0.28).

For OCT data, 1D TSNIT RNFL data were obtained from 136 participants who underwent a full ophthalmological evaluation and were labeled as glaucomatous or ocular normal on the basis of visual field (VF) test. The VF tests were performed using a standard automated perimetry (SAP) (either a central 30-2 or a 24-2 threshold test and size III white stimulus) with Swedish Interactive Threshold Algorithm (SITA Standard).

Participants were under the care of glaucoma specialists. The VF data were classified as glaucomatous using Anderson and Patella criteria [92].

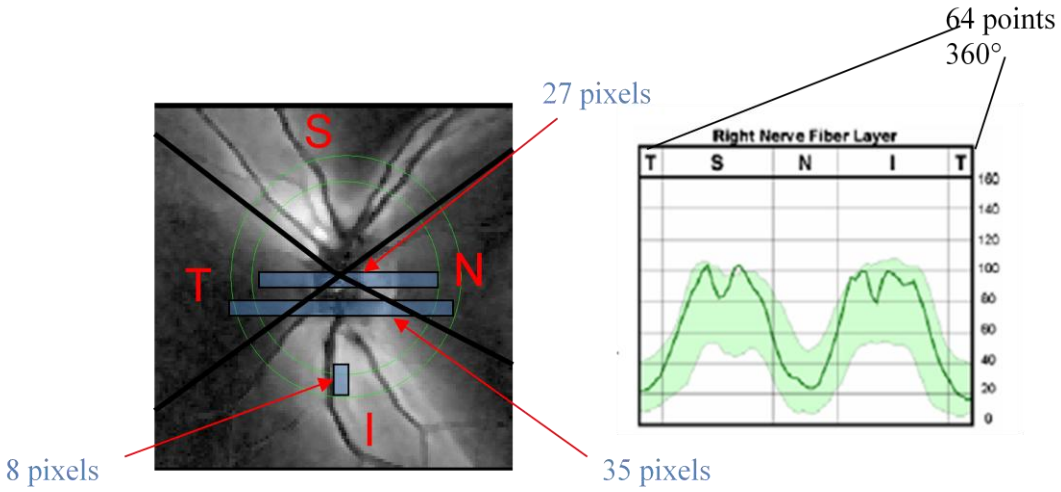

(a) (b)

Figure 3-2. (a) TSNIT RNFL measurement around the optic disc using a scanning laser polarimeter (b) resulting 1D TSNIT RNFL data composed of 64 sectors of thickness

The glaucomatous VF data met at least 2 of the 3 criteria: (1) Three or more non-edge points on the pattern deviation plot having a probability of less than 5% of the normal population and at least one of those points with a probability of less than 1%, (2) a PSD value less than that of 5% of normal reliable fields, and (3) a Glaucoma Hemifield Test (GHT) ‘‘outside normal limits.’’ The ocular normal eyes had to have reliable and normal VF data (absence of all 3 of Anderson and Patella criteria [92]. Reliability criteria for automated perimetry were: fixation losses < 20% and false positives and false negatives < 33%. The VF tests were repeated and defects confirmed within 2 weeks. The ocular normal subjects had the normal VF data that were repeated only if the first VF was

unreliable. The severity of glaucoma was analyzed by staging the VF data using the criteria of Hodapp *et al.* [93]. All glaucomatous individuals included were the ‘‘mild’’ stage. Briefly, the mean deviation (MD) value was no worse than -6 dB and the pattern deviation plot had (1) ≤18 points (25%) depressed below the 5% probability, (2) ≤10 points depressed below 1% probability, and (3) no points in the central 5° with sensitivity below 15 dB.

The 1D TSNIT RNFL data utilized in this study were obtained using the StratusOCT . The RNFL thickness values were obtained from dilated eyes (1% tropicamide) using the fast RNFL protocol (256 A-scans) of StratusOCT. Feature-based techniques were performed on the 1D TSNIT RNFL data of the mean image from 1 eye (selected at random) of each individual. The mean images were created from 3 images (obtained along a ring 3.46 mm in diameter and 20-mm wide) and had a quality score of 8 (on a scale of 0 to 10). The OCT software calculates the average thickness, overall (i.e., 360°), and quadrants (superior, inferior, nasal, and temporal, each 90°). There are no classifiers output by StratusOCT but prior reports have indicated that the output measures, Average Thickness (mean over the 360° TSNIT curve) or Inferior Average (inferior quadrant average thickness, i.e., 226 to 315°) are best at discriminating glaucoma eyes from healthy individuals [8,10-20]. In this study we used Inferior Average, Average thickness and Superior Average and compared it to various fractal-based techniques.

3.2.2. Generating Pseudo 2D Image from 1D TSNIT RNFL Data

The acquired 1D TSNIT RNFL data is usually analyzed along with other information using the standard machine classifier known as the Nerve Fiber Indicator (NFI). However, in the present work, this 1D TSNIT RNFL data is converted into pseudo 2D image format. The detailed algorithm for such pseudo 2D image generation technique from a 1D TSNIT RNFL data is shown in Fig. 3-3. For each row vector of 1D TSNIT RNFL data, its maximum value (m) is calculated and rounded into the closest integer. Then, a 2D matrix is formed using the integers as the x-values and corresponding indices as the y-value. For the final pseudo 2D image, the resulting matrix is flipped and plotted.

Algorithm 1

for *each 1D TSNIT RNFL data vector set*

Calculate maximum value (m) of the vector set

Obtain a null (m × m) matrix array a(i,j)

for *each value of data vector*

Round the value to the closest integer

Populate matrix a(i,j) using data vector as y-values and corresponding index as x-value

Flip the matrix a(i,j)

Save the resulting pseudo 2D image of 1D TSNIT RNFL data vector

Figure 3-3. Pseudo code for pseudo 2D image generation

Figure 3-4 (a) shows an example of the 64-point 1D TSNIT RNFL data obtained by GDx-VCC and Fig. 3-4 (b) shows an example of pseudo 2D image converted from the obtained 1D TSNIT RNFL data for a patient. Note in Fig. 3-4 (b), the pseudo 2D image is obtained by plotting each data point as the *y*-axis value with the corresponding index as the *x*-axis value. This pseudo 2D representation is used to compute FD using a box-counting (BC) method as discussed below. The pseudo 2D image still characterizes 1D TSNIT RNFL data while retaining its fractal elements.

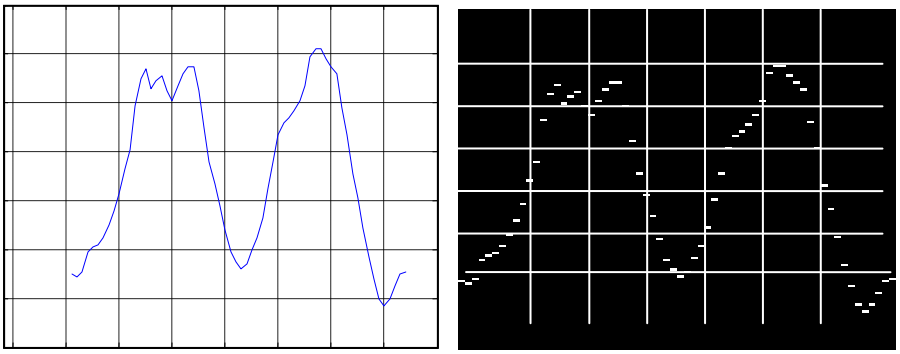

(a) (b)

Figure 3-4. (a) Plot of 1D TSNIT RNFL data (b) corresponding pseudo 2D image

3.2.3. Generating Fractal-based Features Using FD

Using the pseudo 2D image of a 1D TSNIT RNFL data, fractal analysis (FA) is performed to calculate the fractal dimensions (FDs) for each size of the boxes. The detailed algorithm to compute the FDs using the BC method is shown in Fig. 3-5. The pseudo 2D image is divided into boxes of predetermined size, "*r*." Then, for each box size of *r*, the number of the boxes needed to capture the signal values, "*N*," is counted and

the magnitude factor is calculated, which is the reciprocal value of *r*. The resulting FDs are the ratios between the logarithmic values of *N* and 1/*r*.

Algorithm 2

for *each pseudo 2D image*

Divide the pseudo 2D image into boxes of size r × r

for *each box of size r*

Count the occupied boxes: N

Calculate the magnitude factor (1/r)

FD = log(the number of occupied boxes)/log(1/r)

Figure 3-5. Pseudo code for the box counting (BC) method

Figure 3-6 shows an example of the BC method for calculating the FDs. Note in Fig 3-6. (a)(b)(c) that the number of occupied boxes, *N*, is varied with the box size, *r*. The resulting FDs are piece-wise linear and the slopes between each box-size have been extracted as the new features. In Fig. 3-7 (a)(b), we show the examples of two different patients' FD features. Each plot shows the new fractal-based features for two example patients from glaucoma and ocular normal patient group, respectively. For both plots, the *x*-axis is the size of box for fractal computation and the *y*-axis is the FD at each box size.

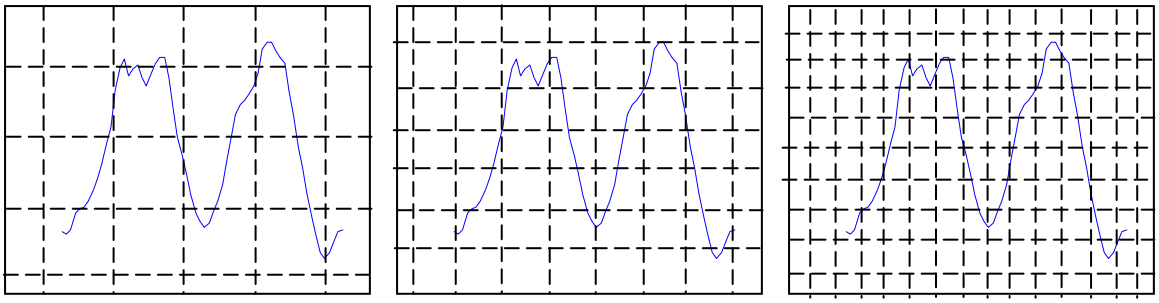

(a) (b) (c)

Figure 3-6. The box-counting (BC) method to estimate FD (a) box size (pixels): r = 6; the number of occupied boxes: N = 14 (b) r = 8; N = 23 (c) r = 4; N = 31

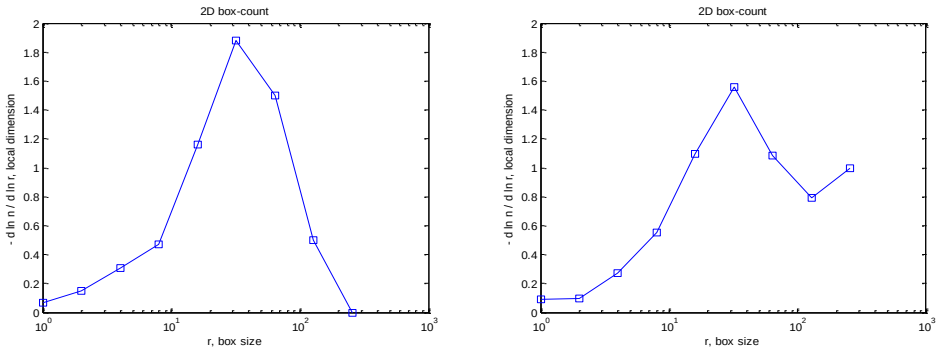

(a) (b)

Figure 3-7. Two different patients' FD features based on pseudo 2D image representation of (a) glaucomatous (b) ocular normal patient

3.2.4. Feature Selection Using PCA and Classification Using LDA Classifier

Once the FD features are extracted, the features need to be selected for effective handling. Principal component analysis (PCA) is used to select the FD features by reducing their dimension and keeping all the essential information contained in the features. By selecting the fractal-based features, the redundancy caused by interdependencies in the features is eliminated and statistical independence is maintained. The next step involves classifying the patient data into the two classes. We exploit a Fisher's LDA classifier for an easy and robust way for the classification. The role of the

LDA classifier is to provide a criterion that optimally classifies a set of values into two categories (in the present study: glaucomatous eyes and ocular normal ones). The criterion of the LDA classifier is based on two distinct values. The resulting classification measure is obtained by using the shorter distance from the testing sets. To assure the external validity of the classifier using the LDA classifier, it must be tested on the testing data that are independent of the training data from which they were derived. To achieve this, the whole dataset is first randomly split into two independent subsets; one for training the LDA classifier and the other for testing. This is called a "leave-out" method. To provide even more robust validation procedure, a variation of 10-fold cross validation is used, as it is superior to a "leave-out" method and is especially advantageous when a very large sample size is not available. For this procedure, the majority of the patient data (in our study, 90%) are selected for the training data, and the classification is applied to the small test data consisting of the remaining data (10%). In the present work, we train the data set ten times for each tenth.

3.3. Results and Discussions

3.3.1. SLP Data

Figure 3-8 (a) shows the plot of raw 1D TSNIT RNFL data of the glaucomatous and ocular normal patients. As can be seen in Fig. 3-8 (a), there are considerable overlaps between the two patient groups. In Fig. 3-8 (b), the scatter plot of the mean thickness values and the variance between them is shown, which suggests that the classification is very difficult using only the mean thickness values.

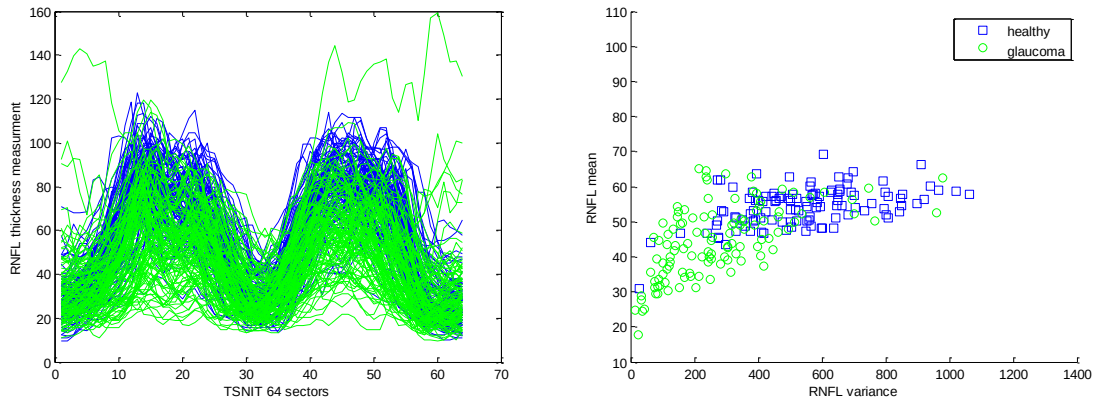

(a) (b)

Figure 3-8. Plot of (a) raw data of glaucomatous (green) and ocular normal patients (blue) (b) Scatter plot using the mean and variance of each patient group

Figure 3-9 (a) shows the LDA distance measure plot for each patient samples. In Fig. 3-9 (a), it is obvious that the glaucomatous and ocular normal patients can be better differentiated using our new feature set obtained from the difference measures. To calculate these difference measures, the largest LDA values of each glaucomatous or ocular normal group are extracted. These LDA values are obtained based on the mean and variance from the first principal component of each group in the training phase. When a given testing patient's data is presented, the largest LDA value of the patient is calculated and subsequently its distance measure from each group's LDA value is measured, respectively. For our classification purpose, the distance measures from the ocular normal patient group have been assigned to be positive while those of glaucomatous patients have been assigned to be negative. Then, the shorter distance toward either group indicates the more likelihood toward that group and, thus, the unknown testing patient is labeled belonging to that specific group. Figure 3-9 (b) shows the scatter plot using the distance measures and the LDA values. In Fig. 3-9 (b), the

ocular normal patients and glaucomatous patients are separated in the vertical line of "0" and the typical LDA values for each patient group are around "+1" and "-1." Figure 3-9 (c) shows the relationship between AUROC and feature numbers. This relationship demonstrates that the more FD features are included, the better performance is achieved. Hence, all of the seven FD features are used to compute PCA and LDA, respectively.

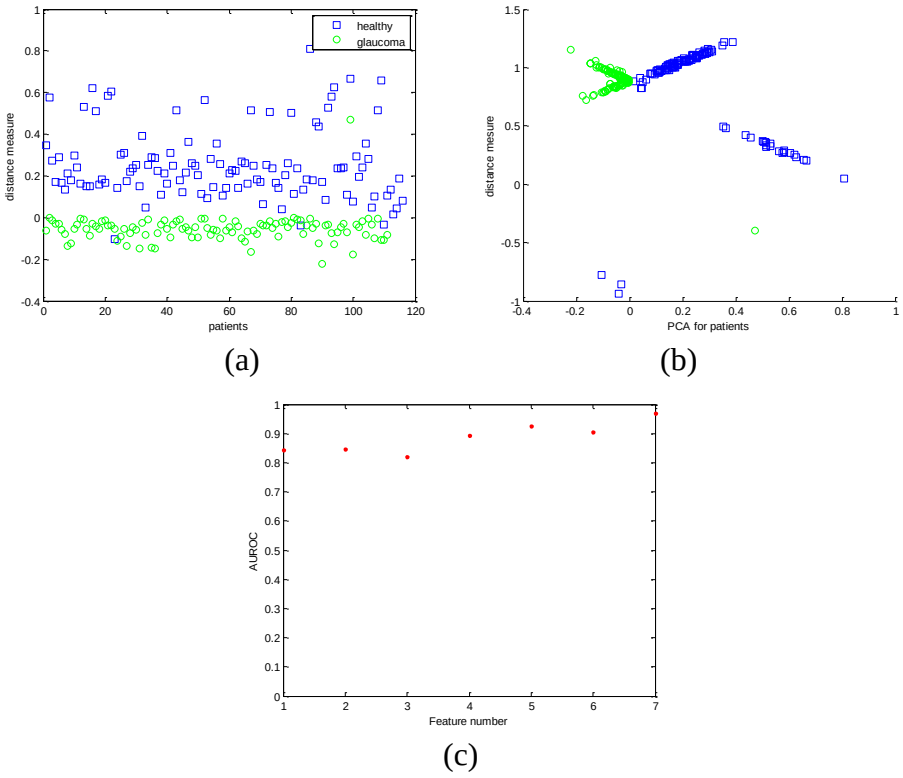

Figure 3-9. (a) Plot of distance measures of healthy patients (square) and glaucoma patients (circle) (b) Scatter plot using the distance measure and LDA value of each patient group (c) AUROC vs. feature numbers

Figure 3-10 (a) shows the comparison of AUROC curves between fractal and a few other machine generated parameters such as NFI, TSNIT Average, Superior Average

and Inferior Average. The sensitivity and specificity plot in Fig. 3-10 (b) shows the improved detection capability of our fractal-based technique.

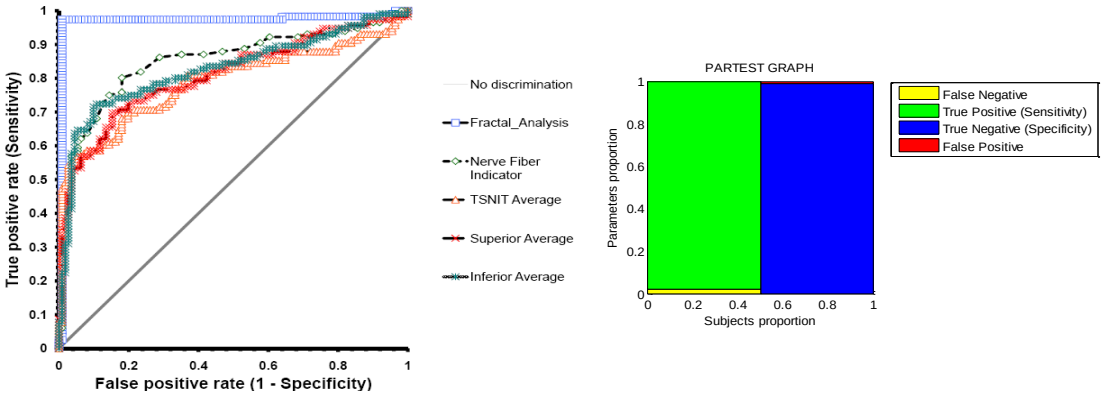

(a) (b)

Figure 3-10. The results of fractal-based technique using piecewise FD slopes as features (a) The comparison of AUROC (b) Truth table (AUROC: 0.97)

Table 3-1. The comparison of sensitivity, specificity and AUROC among standard machine parameters and FA

	TSNIT Average	**Superior Average**	**Inferior Average**	**NFI**	**Fractal Analysis**
Sensitivity	0.97	0.70	0.72	0.75	0.97
Specificity	0.54	0.85	0.89	0.86	0.99
AUROC	0.79	0.81	0.83	0.85	0.97

We summarize our results in Table 3-1. From the Table 3-1, we observe that the AUROC of the fractal analysis (FA) is higher than those of the standard machine classifiers obtained with the parameters output by GDx-VCC. Note the NFI had the

highest AUROC and is significantly different when compared to the TSNIT average and Superior Average but not Inferior Average (DeLong *et al.*'s method, p = 0.002, 0.01 and 0.2 respectively). Comparison to the FA shows that the AUROC of FA is greater than all standard machine parameters in identifying glaucomatous eyes ($p < 0.0001$ in all comparisons).

3.3.2. OCT Data

Figures 3-11 shows the comparison of ROC curves for the fractal-based techniques. In Fig. 3-11 (a) the combined BC and mBm technique performs the best when compared to the BC technique and the mBm technique. Note in Fig. 3-11(a), the combined BC and mBm method performs the best among all three fractal-based techniques with corresponding AUROC of BC, mBm and the combined BC and mBm methods being 0.81, 0.87 and 0.89, respectively. Comparing the diagnostic accuracy of standard machine classifiers output, usually given as Superior Average, Inferior Average and Average thickness of the 1D TSNIT RNFL, note that the Inferior Average is the best at discriminating glaucoma from ocular normal individuals followed by Average thickness and Superior Average with the AUROC being 0.84, 0.76 and 0.70, respectively.

Comparison of the AUROC of the best fractal-based technique and the set of standard machine measures shows that the diagnostic accuracy of the combined BC and mBm method is significantly greater than the Average Thickness and Superior Average by 13% and 19% respectively (DeLong *et al.* $p < 0.0001$ and $p = 0.001$), whereas the difference in diagnostic accuracy of Inferior Average and the combined BC and mBm

method was 5%, which was not statistically significant (DeLong *et al*. p = 0.058). The summary of results is shown in Table 3-2.

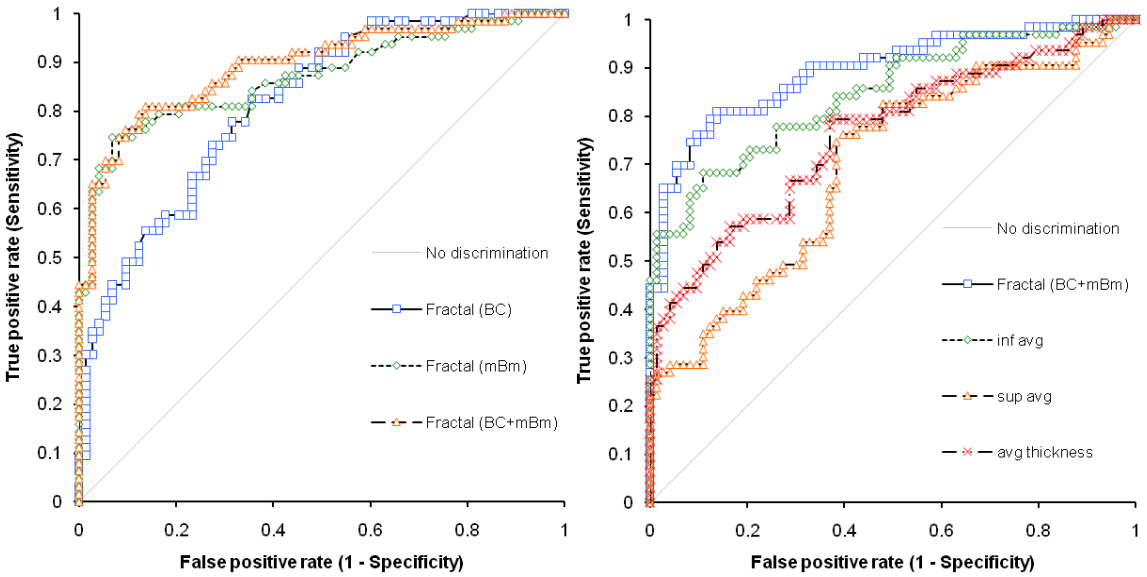

Figure 3-11. ROC curves comparison of (a) BC, mBm and the combined BC and mBm (b) the combined BC and mBm, Inferior Ave., Superior Ave. and Ave. thickness

Comparison of the AUROC of the best fractal-based technique and the set of standard machine measures shows that the diagnostic accuracy of the combined BC and mBm method is significantly greater than the Average Thickness and Superior Average by 13% and 19% respectively (DeLong *et al*. p < 0.0001 and p = 0.001), whereas the difference in diagnostic accuracy of Inferior Average and the combined BC and mBm method was 5%, which was not statistically significant (DeLong *et al*. p = 0.058). The summary of results is shown in Table 3-2.

The performance as assessed by AUROC in diagnosing glaucomatous damage using fractal-based techniques in SLP data is 0.97 while that in OCT data is 0.89

respectively. There are numerous reasons that could account for such a difference. First, the patients with glaucoma in the present study were with mild glaucomatous damage whereas the previous study included all stages of glaucoma. Second, there are inherent differences between the 1D TSNIT RNFL data obtained using SLP and OCT that could account for the difference in diagnostic performance.

Table 3-2. The comparison of sensitivity, specificity and AUROC among standard machine parameters and fractal feature-based techniques

	Average Thickness	**Superior Average**	**Inferior Average**	**FA (BC)**	**FA (mBm)**	**FA (BC+mBm)**
Sensitivity	0.79	0.76	0.68	0.83	0.75	0.81
Specificity	0.63	0.60	0.89	0.64	0.93	0.86
AUROC	0.76	0.70	0.84	0.81	0.87	0.89

A prior report by Gunvant *et al*. found that the diagnostic performance of the WFA was better when using the RNFL estimates obtained using OCT where as the FFA techniques performed best with SLP data [94]. It may be possible that fractal-based techniques give the best diagnostic performance when utilizing SLP data. The present work did not have SLP data matching with OCT data, so direct statistical comparison of the performance of fractal-based technique in SLP versus OCT is not possible but will be an interesting topic of research in future.

For OCT, the 1D TSNIT RNFL data has been obtained by TD-OCT (StratusOCT 4.0 Carl Zeiss Meditec) which is still widely used and commercially available. The newer generation of frequency domain OCT (FD-OCT) like Cirrus OCT (Carl Zeiss Meditec, RTVue OCT Optovue, Inc.) provides 1D TSNIT RNFL data that have an axial resolution of approximately 5-6 microns. It is anticipated that performance of such fractal-based techniques will be maintained or improved given the decrease in signal to noise ratio of the new OCT's. This hypothesis however remains to be investigated.

3.4. Conclusion

In this chapter, we develop and implement novel fractal-based techniques for improved glaucoma detection on pseudo 2D representation of SLP data. Our statistical analysis shows that in comparison, our FA method outperforms the standard machine classifiers (i.e., NFI of the GDx-VCC) with 97% accuracy in SLP data.

Our novel multi-fractal-based techniques for improved glaucoma detection using OCT data is the first attempt in literature to apply such techniques on the 1D TSNIT RNFL data obtained by the StratusOCT. We observe that the pseudo 2D fractal-based techniques for OCT data perform better than the standard machine classifier. Our novel multi-fractal features (i.e., the combined BC and mBm FD features) also obtain diagnostic accuracy greater than standalone machine outputs with 89% accuracy.

In the future, direct statistical comparison of the performance of fractal-based technique in SLP versus OCT will be investigated, since there are inherent differences between the 1D TSNIT RNFL data provided by the SLP (GDx-VCC) and that provided by the OCT (StratusOCT).

4. Novel Fractal/Multi-Fractal Features and Application of Multi-class Classification for Improved Progression Prediction

4.1. Introduction

In this work, we investigate novel fractal/multi-fractal features and application of multi-class classification for improved glaucomatous progression prediction using the 1D TSNIT RNFL data acquired by SLP. Since glaucomatous damage to the RNFL is irreversible and glaucomatous progression worsens vision loss, detecting or predicting glaucomatous progression is critical in management of glaucoma. While analyzing a series of the visual field (VF) data obtained by standard automated perimetry (SAP) has been widely used in diagnosing glaucomatous progression, it has been shown that structural changes in the RNFL often precede functional changes in the VF data [3-4]. Also, glaucomatous progression is known to be very difficult to differentiate from the test variability and the progression prediction may require a variety of statistical approaches. Hence, detecting or predicting glaucomatous progression in an objective manner by assessing the progressive structural damage to the RNFL still remains challenging.

In addition, prediction of glaucomatous progression may require a multi-class classifier, since it is a multi-staged disease–progression, non-progression and ocular normality. For two-class classification, support vector machine (SVM) has been widely used for its simple geometrical interpretation, but it cannot be directly applied to a multi-class classification problem such as classification of progressors, non-progressors and ocular normal patients 40-41. A kernel-based SVM has been proved to be effective in multi-class classification due to its capacity of handling nonlinearly separable data by

mapping the input space into the kernel-based feature space [42]. The Gaussian kernel has a corresponding infinite-dimensional feature space, which is well regularized.

We first extract novel fractal/multi-fractal features from 1D TSNIT RFNL data and normalize them accordingly. We then evaluate the effectiveness of utilizing fractal/multi-fractal features for classification of progressors and non-progressors, progressors and ocular normal patients using different types of two-class linear classifiers including LDA. We also compare our methods with other types of feature-based techniques such as wavelet-Fourier analysis (WFA) and fast Fourier analysis (FFA). Next, we experiment and compare the efficacy of fractal/multi-fractal features with those of WFA and FFA for multi-class classification of progressors, non-progressors and ocular normal patients using a nonlinear Gaussian kernel SVM classifier. Finally, we evaluate and compare the effectiveness of our novel application of multi-class classification with other nonlinear methods such as neural network (NN) to predict glaucomatous progression.

For this research work, we analyze the 1D TSNIT RNFL data acquired by SLP from one eye of 96 real patients (14 progressors, 45 non-progressors, and 37 ocular normal patients). For statistical performance evaluation and comparison, we compute the sensitivity, specificity and AUROC for our novel fractal/multi-fractal feature-based techniques along with similar AUROC using other feature-based techniques such as WFA and FFA.

The rest of the chapter is organized as follows. In section 4.2, the detail methods of our proposed techniques are provided. Section 4.3 presents the experimental results

and discussions for our proposed techniques that utilize our novel fractal/multi-fractal features and multi-class classification. Finally, conclusion is given in section 4.4.

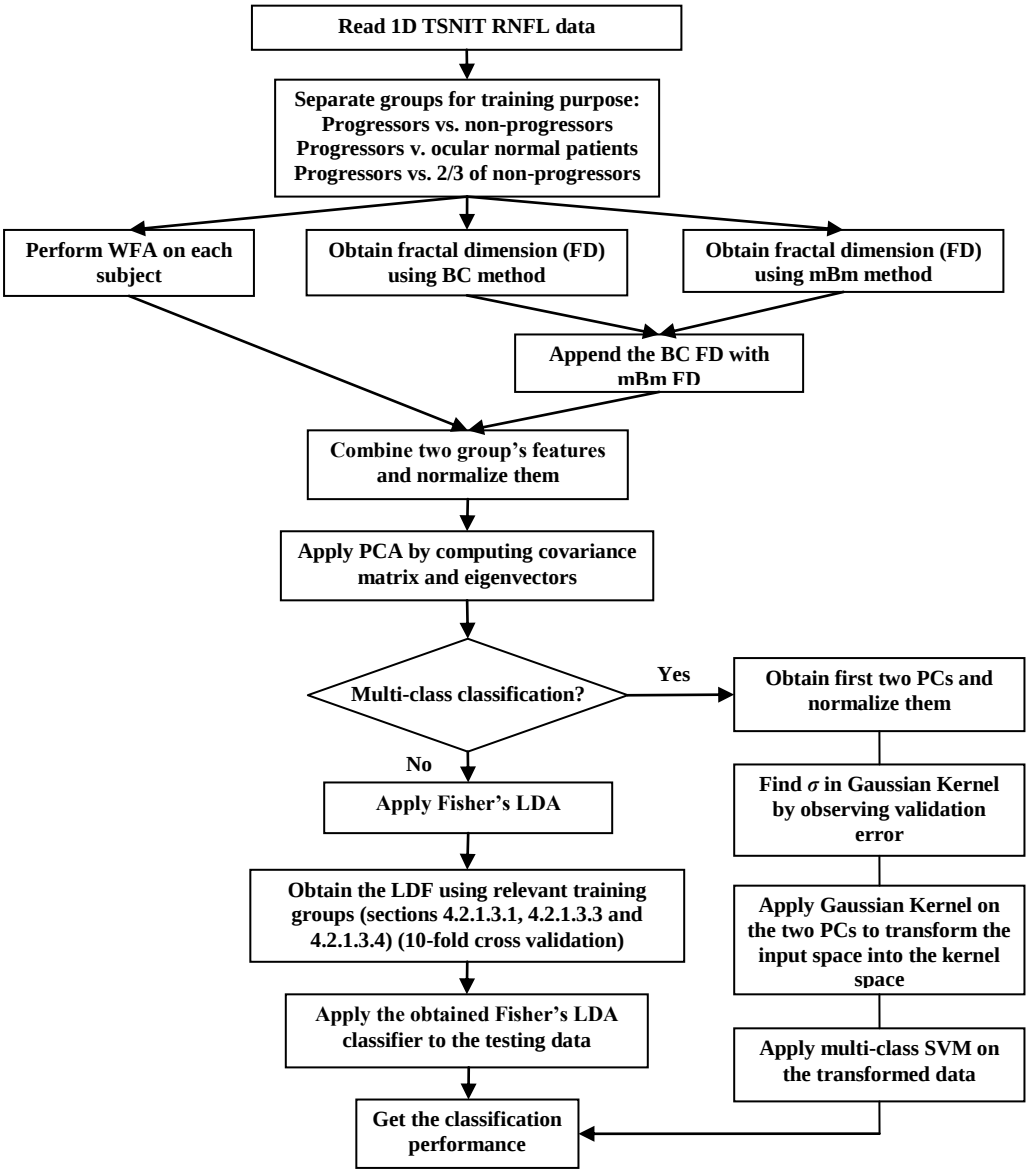

Figure 4-1. The flowchart of our feature-based techniques and application of multi-class classification for glaucoma progression prediction

4.2. Methods

Figure 4-1 shows the flowchart of our novel fractal/multi-fractal based techniques and application of multi-class classification for glaucomatous progression prediction. For preprocessing, 1D TSNIT RNFL data are acquired, normalized and transformed to pseudo 2D images as discussed in [33]. Then, a WFA and fractal/multi-fractal based techniques are applied to obtain the representative features for subsequent classification. PCA projection and Gaussian kernel method are utilized next for feature selection. Finally, Fisher's LDA classifier and a multi-class SVM classifier are used for two-class and multi-class classification problems respectively. Note these classifiers are chosen based on good glaucoma classification performance in our prior works [95-96]. A 10-fold cross validation is also used for two-class problem wherein 90% of the data are selected for the training and the remaining 10% is applied for the testing. The sensitivity, specificity and AUROC are calculated for classification performance among progressors, non-progressors and ocular normal patients. AUROC is calculated using the DeLong *et al*. technique [91].

In this work, total 96 patients are followed starting from the baseline up to 40 months. Using the SLP (GDx-VCC), 1D TSNIT RNFL data have been measured on each patient, approximately every 6 months. The patients are deemed progressors, non-progressors or ocular normal on the basis of visual field (VF) test. For extracting more meaningful features from each group of the 1D TSNIT RNFL data, we adopt feature extraction techniques such as BC and mBm methods as explained in previous sections. We now discuss the detailed steps in the proposed techniques and the different options

for training and testing our classifiers for discriminating progressors, non-progressors and ocular normal patients respectively.

4.2.1. Two-class Classification Method

4.2.1.1. Preprocessing 1D TSNIT RNFL Data for FA

For effective extraction of fractal/multi-fractal features, the 1D TSNIT RNFL data are converted to pseudo 2D images. Briefly, for each 1D TSNIT RNFL data, its 1D maximum value (m) is calculated and rounded to the closest integer. Then, a 2D matrix is formed using the integers as the x-values and corresponding indices as the y-values. For the final pseudo 2D image, the resultant matrix is flipped and plotted.

4.2.1.2. FD Estimation Using the Combined BC and mBm Features

The main difference between the BC and mBm methods lies in mono-fractal and multi-fractals. While the BC method only calculates the homogenous mono-fractal, the mBm method calculates multi-fractals using wavelet filters. The combination of BC method and mBm method may enhance the performance, for they may complement each other. The BC method acquires its FD features by counting the occupied boxes and dividing them by the magnitude factor, which is the reciprocal of the size of the box. This method is closely related to the morphology of the 1D TSNIT RNFL data (i.e., shape of the data). On the other hand, the mBm method involves estimation of fractal characteristics in multi-resolution for non-stationary signal. Therefore, second technique may be complementary to the features that cannot be represented by BC method alone.

We extract the BC and the mBm features from the pseudo 2D TSNIT RNFL images. Subsequently, the resulting FDs appended to each other for subsequent analysis. For comparison, other existing feature-based technique such as WFA is also applied on the 1D TSNIT RNFL data. The extracted features are normalized and are further processed by principal component analysis (PCA) to be stabilized.

4.2.1.3. Case Study

For two-class cases, Fisher's LDA classifier is used for the classification of the selected features. A 10-fold cross validation is also used where 90% of the data are selected for training and the remaining 10% is applied for testing. For the multi-class case, we first take two largest principal components (PCs) and normalize them for the use of the Gaussian kernel-based multi-class SVM. After finding σ, the input space is transformed to the kernel space. Then, a linear classifier is used for multi-class classification. The sensitivity, specificity and AUROC are calculated in identifying glaucoma from ocular normal individuals. We now discuss different options for training and testing our classifiers for discriminating progressors, non-progressors and ocular normal patients respectively. The goal is to investigate with what accuracy does the classifiers detect progressive damage in the RNFL due to glaucoma prior to the occurrence of the "event" that is progression as recorded by visual fields (VFs).

4.2.1.3.1. Classification of Progressors vs. Non-progressors: Training with 90% of Progressors and Non-progressors

We use the complete dataset comprised of the baseline 1D TSNIT RNFL data that include 14 progressors and 45 non-progressors for training. Using 90% of this baseline dataset (progressors and non-progressors), the target classifier for each feature-based technique (e.g., WFA and FA) is obtained. This procedure obtains the reduced number of features using PCA and uses Fisher's LDA classifier to characterize the glaucomatous progression. The testing data is composed of the remaining 10% of the dataset. The baseline progressors are replaced with the progressors from a prior visit (1, 2 or 3 scans prior), and the non-progressors are replaced with the average values of non-progressors at all visits (up to 60 months) to prevent over-fitting problem. We assess each feature-based technique by calculating sensitivities, specificities and AUROC at 1 scan prior, 2 scans prior and 3 scans prior to the progression. The interval between successive scans (prior to progression) is approximately 6 months.

4.2.1.3.2. Evaluation of Ocular Normal Patients

Along with predicting the changes in glaucoma, it is also very crucial that we do not have a high rate of false positives (specificities) that would limit the usability of our classifiers for further analysis. Consequently, for measuring specificities, we use the same training data and the same LDA classifiers as discussed in the previous analysis, the section 4.2.1.3.1, for the progressors and non-progressors case. However, the testing data is different and consists of 37 ocular normal patients. Here, we obtain only specificities, since the progressors are not included in testing. The reason for this testing is to assess

the effectiveness of previous classifiers for avoiding false positives in ocular normal patients.

4.2.1.3.3. Classification of Progressors vs. Ocular Normal Patients: Training with 90% of Progressors and Ocular Normal Patients

The differentiation between the progressors and ocular normal patients using appropriate features is also interesting. Therefore, we first obtain the complete dataset comprised of the 1D baseline TSNIT RNFL data that includes 14 progressors and 37 ocular normal patients. Similar to the section 4.2.1.3.1, using 90% of this dataset, the target LDA classifier for each feature-based technique is obtained. After obtaining the LDA classifiers, instead of using non-progressors, we use ocular normal patients as the test dataset.

4.2.1.3.4. Classification of Progressors vs. Non-progressors: Training with 67% of Non-Progressors and Ocular Normal Patients

Similar to the previous analysis, it is important to differentiate the non-progressors from ocular normal patients for predicting the changes in the progressors. In this case, we train our LDA classifiers with 2/3 of non-progressors (31 out of 45 patients) and all of ocular normal patients (37 patients). Based on the LDA classifiers obtained from this training set, we classify the ocular normal patients from those who convert to non-progressors. By assessing the relationship between ocular normal patients and non-progressors, we may predict the future progressors. The test data is composed of 14 progressors at 1 scan prior, 2 scans prior and 3 scans prior to the progression and the

remaining 1/3 of non-progressors (14 out of 45). These 14 non-progressors are selected randomly and the testing is done using 10-fold cross validation. The results are then averaged over the 10 folds to produce a single estimation.

4.2.2. Multi-class Classification Method

For multi-class classification, we first exploit kernel-based SVM, since such a nonlinear classifier has shown to be effective in discriminating nonlinearly separable data [39].

4.2.2.1. Data Preprocessing Using the Gaussian Kernel

For using the kernel-based multi-class SVM, we first organize the extracted features into a 2D format. For this, we obtain two largest principal components (PCs) from the features of each input space (i.e., WFA and FA). We then apply a Gaussian transform as discussed in section 2.6.2 on the PCs for better separability. Using the modularity of kernels, we consider the outputs of Gaussian kernel function as the first vector, while the largest principal components (PCs) as the second vector [42].
For this reason, we have adopted the kernel selection procedure shown at [43]. The detailed algorithm is shown in Fig. 4-2.

As explained in section 2.6.2, σ of the Gaussian kernel is tuned. In this work, we start with 0.35 as an initial value and find that at 1.06, the Gaussian kernel function achieves the best separability among three classes. Figure 4-3 shows the scatter plot using our technique. We plot the kernel data on the *y*-axis versus the first PCs on the *x*-axis. It shows how this kernel method enhances the separability of features. In Figs. 4-3 (a) and

(b), the three classes require a nonlinear classifier. However, in Figs. 4-3 (c) and (d), the three sets of data are relatively better separated than Figs. 4-3 (a) and (b). Note in Fig. 4-3 (b), the features are aligned in straight lines. A possible explanation for this feature alignment can be the characteristic of fractals measurement, which accounts for the closeness of irregularity in natural phenomenon such as TSNIT shapes.

Algorithm 1

1 .Initialize σ with a very small value

2. Maximize the margin

3. ***for*** *each validation set*

Calculate validation error

Increase the kernel parameter with pre-assigned increment: $\sigma \leftarrow \sigma+\delta\sigma$

4. Stop when a pre-determined value of σ is reached. Otherwise, repeat the step 3.

Figure 4-2. Pseudo code for tuning the parameter of the Gaussian kernel [43]

4.2.2.2. Application of Multi-class SVM among Progressors, Non-progressors and Ocular Normal Patients

After pre-processing the data, we train the complete 1D baseline TSNIT RNFL data comprised of 14 progressors and 45 non-progressors and 37 ocular normal patients. By using multi-class SVM, we are able to train three classes concurrently, which is not possible in the sections 4.2.1.3.1, 4.2.1.3.2, 4.2.1.3.3 and 4.2.1.3.4. We then obtain the multi-class SVM classifiers that best characterize each class's decision function. Finally,

the testing is done in a repeated manner and the rate of correct class prediction is measured.

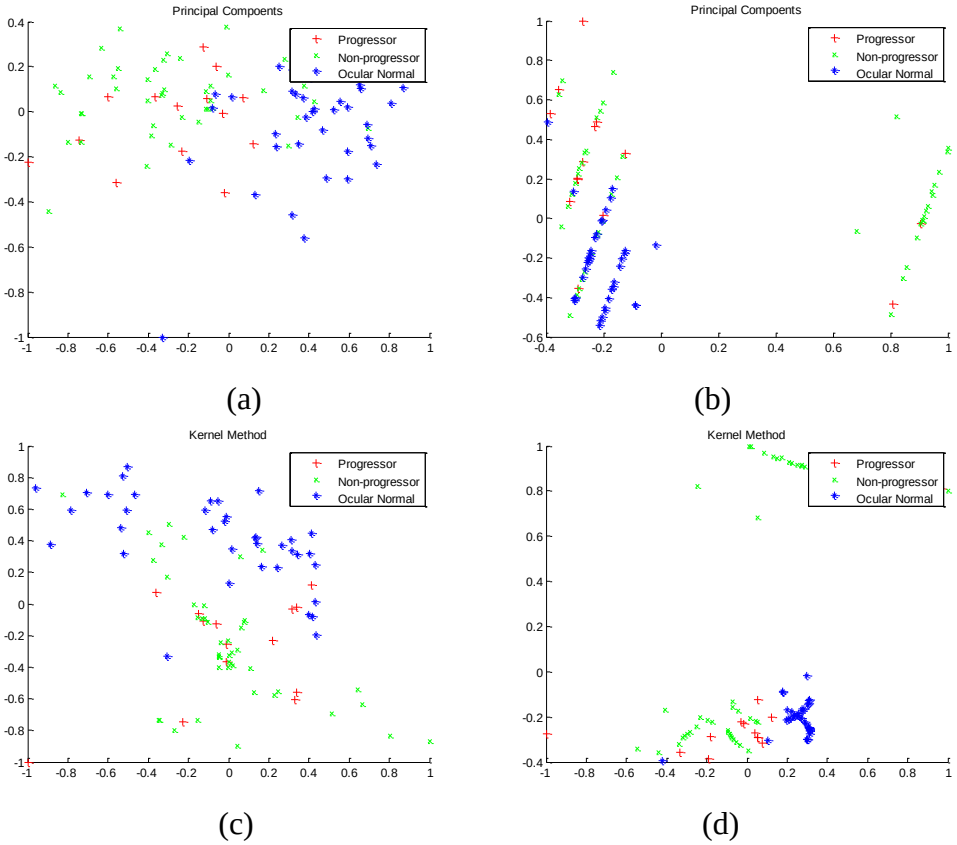

Figure 4-3. An example of using Gaussian kernel method (a) WFA (b) FA - before applying Gaussian kernel (c) WFA (d) FA - after applying Gaussian kernel

4.3. Results and Discussions

4.3.1. Two-class Classification Method

Figure 4-4 compares ROC curves among the two feature-based techniques such as WFA and FA. In Fig. 4-4, as discussed in section 4.2.3.1.2, we do not obtain any ROC curves for the method described in section 4.2.3.1.2, due to the absence of sensitivity.

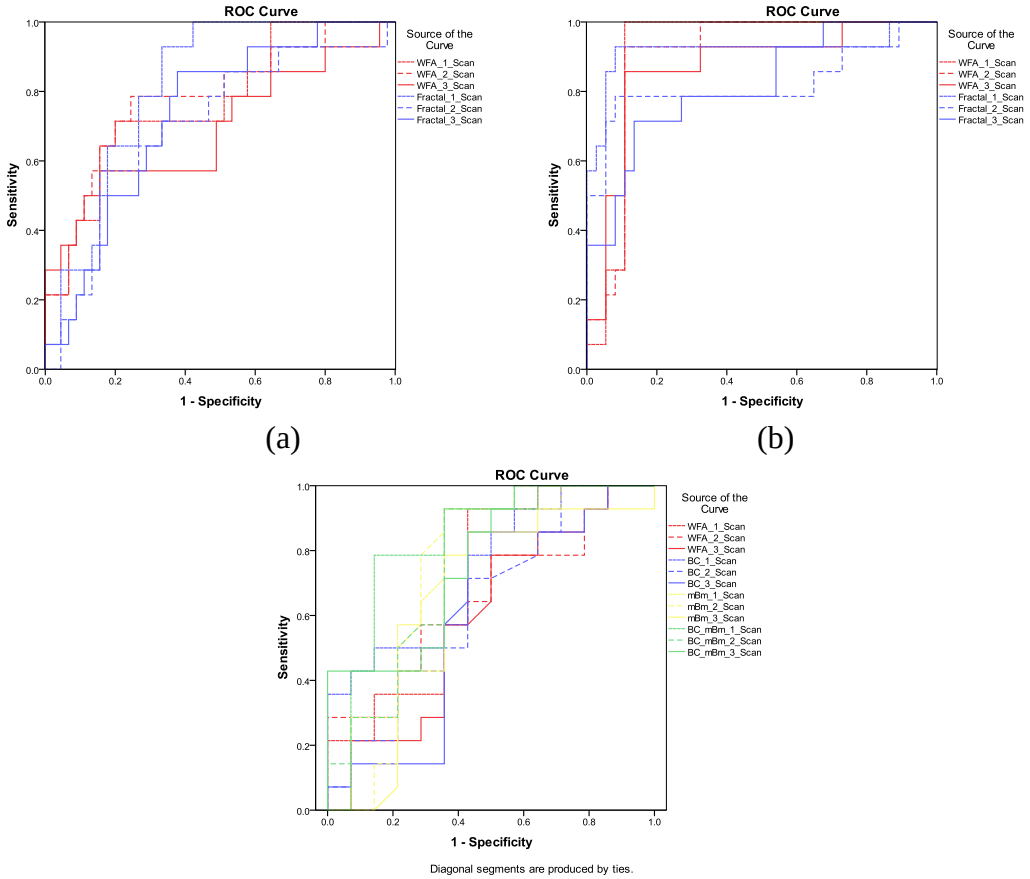

Figure 4-4. ROC curves for WFA and FA: (a) progressors vs. non-progressors as described in section 4.2.1.3.1 (b) progressors vs. ocular normal as described in section 4.2.1.3.3 (c) progressors vs. 1/3 of non-progressors as described in section 4.2.1.3.4

Table 4-1. Classification between progressors and non-progressors using WFA and FA on different visits (sensitivity/specificity/**AUROC**) with sensitivity reported in parentheses when specificity is fixed at 80 and at 90.

Methods	1 scan prior	2 scan prior	3 scan prior
WFA	0.72/0.80/**0.78**	0.78/0.75/**0.78**	0.57/0.84/**0.69**
	(0.72;0.43)	(0.72;0.43)	(0.57;0.43)
FA	0.93/0.67/**0.82**	0.57/0.84/**0.70**	0.85/0.62/**0.73**
	(0.64;0.29)	(0.57;0.21)	(0.50;0.21)

Table 4-1 shows the sensitivities, specificities and AUROC at different visits after the 1 scan prior to progression as explained in the section 4.2.3.1.1. The values in Table 4-1 indicate that the prediction rate using all three feature-based techniques is highest at the first prior to the progression. Comparing the obtained AUROC, we find that the difference in classification performance WFA and FA is not significant (DeLong *et al.* [91] $p > 0.05$). Table 4-2 shows the specificities for WFA and FA respectively, as explained in section 4.2.3.1.2. Note that FA achieves the prediction rate above 80% specificity, which implies that FA can predict progressive glaucomatous damage with moderate accuracy. The above-mentioned results show how FA can be effectively used in predicting glaucomatous progression. It also shows that such methods can be used in predicting ocular normal patient's glaucomatous progression.

Table 4-2. Evaluation of ocular normal patients: training with data from section 4.2.1.3.1.

Methods	Specificity
WFA	**0.76**
FA	**0.86**

Table 4-3. Classification between progressors and ocular normal patients using WFA and FA on different visits

Methods	1 scan prior	2 scan prior	3 scan prior
WFA	0.99/0.89/**0.91** (0.99;0.29)	0.93/0.89/**0.90** (0.93;0.29)	0.86/0.89/**0.87** (0.86;0.50)
FA	0.93/0.92/**0.92** (0.93;0.86)	0.79/0. 92/**0.82** (0.79;0.71)	0.71/0.87/**0.81** (0.71;0.50)

Table 4-3 shows the AUROC as discussed in section 4.2.3.1.3. Table 4-3 indicates the consistency of prediction capability of FA method with moderate accuracy. Table 4-4 shows the result of the partial separation for training and testing. This result implies that partial separation among the same group may not provide the best prediction performance. In Table 4-4, we show that our fractal feature-based techniques offer better classification performance such as 0.82, 0.92 and 0.82, when compared with that of 0.78, 0.91 and 0.70 for WFA for about 6 months (1 scan) prior to progression respectively. However, at two scans prior to progression, the results are reversed, and at three scans prior, the results are about equivalent. Note in Table 4-4 our proposed method using Fisher's LDA performs the best when compared to the least square and multivariate methods. Furthermore, our fractal feature-based method uses just seven features, compared with thirty two features for WFA method to obtain such AUROC results.

4.3.2. Multi-class Classification Method

Figure 4-5 shows the decision boundaries for the kernel-based SVM among progressors, non-progressors and ocular normal patients using WFA and FA features respectively. In Fig. 4-5, the progressors are shown using the darkest, non-progressors are the lightest and ocular normal patients are medium. For comparison with another multi-class classification technique, we use neural network (NN). Figure 4-6 shows the result of multi-class classification using feed forward NN method among progressors, non-progressors and ocular normal patients using WFA and FA.

Table 4-4. Classification between progressors and non-progressors using WFA, FFA and FA on different visits: Training with the data from 2/3 of non-progressors and ocular normal patients and applying the obtained classifier to test all progressors and 1/3 of non-progressors

Methods	Discriminant	1 scan prior	2 scan prior	3 scan prior
WFA	**LDA**	0.93/0.57/**0.70** (0.36;0.21)	0.79/0.50/**0.65** (0.29;0.29)	0.79/0.57/**0.60** (0.21;0.21)
	Least Square	0.36/0.93/**0.53** (0.36;0.36)	0.36/0.93/**0.52** (0.36;0.36)	0.36/0.93/**0.53** (0.36;0.36)
	Multivariate	0.71/0.57/**0.58** (0.14;0.07)	0.50/0.71/**0.54** (0.14;0.07)	0.64/0.57/**0.52** (0.21;0.07)
FFA	**LDA**	0.43/0.93/**0.71** (0.50;0.43)	0.93/0.50/**0.66** (0.35;0.21)	0.71/0.71/**0.66** (0.36;0.14)
	Least Square	0.36/0.93/**0.56** (0.36;0.36)	0.43/0.93/**0.55** (0.36;0.36)	0.43/0.93/**0.53** (0.36;0.36)
	Multivariate	0.93/0.36/**0.56** (0.14;0.07)	0.93/0.36/**0.51** (0.07;0.07)	0.93/0.36/**0.53** (0.07;0.07)
FA (BC)	**LDA**	0.93/0.43/**0.74** (0.50;0.43)	0.71/0.57/**0.63** (0.21;0.21)	0.86/0.57/**0.60** (0.14;0.14)
	Least Square	0.36/0.93/**0.56** (0.36;0.36)	0.36/0.93/**0.56** (0.36;0.36)	0.36/0.93/**0.57** (0.43;0.36)
	Multivariate	0.93/0.57/**0.68** (0.36;0.29)	0.79/0.57/**0.59** (0.14;0.07)	0.86/0.43/**0.55** (0.21;0.07)
FA (mBm)	**LDA**	0.93/0.64/**0.76** (0.29;0.29)	0.93/0.64/**0.72** (0.14;0.07)	0.86/0.57/**0.64** (0.14;0.07)
	Least Square	0.43/0.86/**0.55** (0.43;0.36)	0.43/0.86/**0.55** (0.43;0.36)	0.43/0.93/**0.56** (0.43;0.43)
	Multivariate	0.93/0.50/**0.66** (0.07;0.07)	0.93/050/**0.62** (0.07;0.07)	0.86/0.57/**0.62** (0.07;0.07)
FA (BC+mBm)	**LDA**	0.93/0.64/**0.82** (0.79;0.43)	0.93/0.64/**0.76** (0.29;0.29)	0.93/0.50/**0.76** (0.43;0.43)
	Least Square	0.36/0.93/**0.56** (0.36;0.36)	0.36/0.93/**0.55** (0.36;0.36)	0.36/0.93/**0.55** (0.36;0.36)
	Multivariate	0.93/0.50/**0.63** (0.07;0.07)	0.93/0.43/**0.59** (0.07;0.07)	0.86/0.50/**0.57** (0.07;0.07)

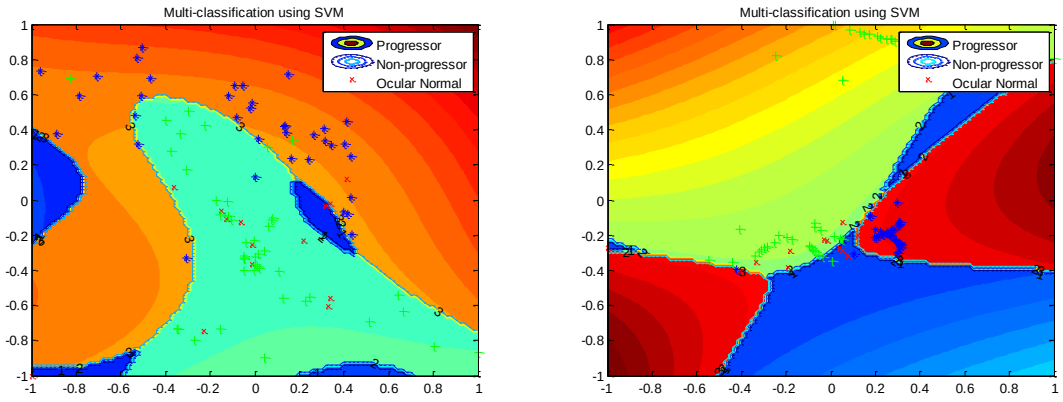

(a) (b)

Figure 4-5. Multi-class classification using SVM with three classes (darkest - progressors; lightest-non-progressors; medium-ocular normal patients) (a) WFA (b) FA

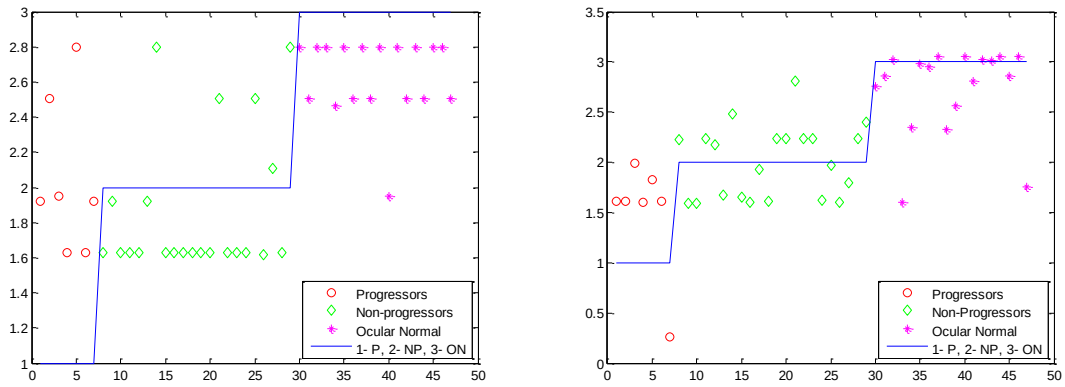

(a) (b)

Figure 4-6. Multi-class classification using NN with three classes (a) WFA (b) FA (circles – progressors; diamonds – non-progressors; stars – ocular normal patients)

Table 4-5 summarizes and compares the multi-class SVM classification results with NN method for predicting glaucomatous progression. Here again we show FFA performance results for complete comparison [97]. Since this result is for multi-class classification, separate sensitivity and specificity measures cannot be obtained. Table 5 shows the better correct rate of 0.88 for multi-class classification using our multi-class

SVM method among progressors, non-progressors and ocular normal patients using FA, compared with those of 0.82 and 0.86 using WFA and FFA respectively.

Table 4-6 shows further comparison of our fractal feature-based technique with other existing approaches to glaucomatous progression prediction in literature [60-61]. Note both Vermeer *et al*. and Alencar *et al*. achieved better sensitivity than ours. Vemeer *et al*. used two different datasets to obtain such measures (e.g., dataset A for specificity and dataset B for sensitivity). Similarly, Alencar *et al*. used an observational cohort study where there are too many glaucoma patients including the progressors compared to ocular normal patients (431 glaucomatous and 22 ocular normal out of 453 total patients, which is, 95% to 5% ratio for glaucoma patients). In comparison, our patient data is more balanced such that our corresponding ratio between glaucoma and ocular normal patients is 61% to 39% (59 glaucomatous and 37 ocular normal patients out of 96 total patients).

Table 4-5. Correct classification rates for using FFA [96], WFA and FA

Methods	Correct Rate (SVM)	Correct Rate (NN)
WFA	**0.82**	**0.72**
FFA	**0.86**	**0.76**
FA	**0.88**	**0.77**

Table 4-6. Comparison of the fractal feature-based technique with existing methods

Authors	Number of patients	Dataset Acquisition	Feature Extraction	Classification Result	Training/Testing
Vermeer *et al.*	812 normal eyes from 154 patients 3351glaucoma eyes from 489 patients 20 progressors	GDx-VCC	Global loss and local loss from 1D TSNIT RNFL data	Sensitivity: 0.420 Specificity: 0.905	Training – dataset A: the ocular normal patients dataset for specificity dataset B: the progressors set for sensitivity Testing – Using the same sets via k-fold cross validation.
Alencar *et al.*	453 eyes from 252 patients	GDx-VCC	1D TSNIT RNFL data	Sensitivity: 0.500 Specificity: 0.960	Training – GDx-GPA (Inherently trained using Normative Database (540 normal and 271 glaucoma)) Testing – 453 patients
Our current work	96 eyes (14 progressors, 45 non-progressors, 37 ocular normal patients)	GDx-VCC	Fractal (BC & mBm) features from pseudo 2D TSNIT RNFL data	AUROC: 0.820 (section 4.2.1.3.1) Specificity: 0.860 (section 4.2.1.3.2)	Training – Using 90% of the dataset Testing – 10% (10-fold cross validation)

Table 4-7. Comparison of computational time among FFA, WFA and FA

Elapsed Times								
FFA			**WFA**			**FA**		
Feature Extraction	Feature Selection	Total Time	Feature Extraction	Feature Selection	Total Time	Feature Extraction	Feature Selection	Total Time
2.24	344.28	346.52	1.78	75.58	77.36	30.19	2.24	32.43

Therefore, our technique in this study obtains comparable or better results with more balanced patient dataset than those reported in literature [60-61]. Furthermore, while the existing methods utilize feature extraction that involves up to 64 Fourier coefficients, our technique exploits only seven fractal features, which results in less computational complexity. Table 4-7 shows the comparison of the computation time among FFA, WFA and FA for feature extraction and selection respectively. Note we use a PC with the CPU speed of 3.06GHz and the memory of 3.48 GB for all our processing in this work. Table

4-7 shows that while FA takes more time in feature extraction step, it takes the less time overall compared to the other methods due to the less number of features.

4.4. Conclusion

In this work, we demonstrate the efficacy of novel fractal and multi-fractal feature-based techniques to detect glaucoma and predict glaucomatous progression. We also compare our performance with existing feature-based techniques such as WFA and FFA. We then report the effectiveness of classification of progressors, non-progressors and ocular normal patients using multi-class SVM. Statistical analyses show that our novel multi-fractal feature-based technique can predict glaucomatous progression more effectively than the existing feature-based techniques such as WFA and FFA. In addition, we also show that application of multi-class SVM classification can discriminate the different stages of glaucomatous progression. Our fractal feature-based technique also achieves either better or comparable performance, when compared to those in literature with less number of features and less computational complexity.

5. Selective Fusion of Structural and Functional Data for Improved Glaucoma Detection

5.1. Introduction

Glaucoma is a progressive optic neuropathy characterized by both structural and functional damages to the visual system. It has been known that retinal ganglion cell death corresponds to the structural changes in retinal nerve fiber layer (RNFL) [1-4]. Glaucomatous damages may also result in functional deficits in visual field (VF) and ultimately cause blindness [51, 68]. For a complete and reliable assessment of glaucoma, it may be necessary to consider both structural and functional damages. The RNFL defect and VF loss in glaucoma have been shown to be closely related. Such a relation indicates a local correspondence between structural and functional changes in glaucoma [48]. Hence, it is desirable to exploit a known relationship between structural and functional data such that a topographic correspondence may provide better glaucoma detection [98-100]. Further, directly combining structural and functional data has shown improvement of the diagnostic capability of glaucoma [47]. Consequently, we investigate selective feature-based fusion that exploits the known topographic correspondence.

For effective fusion of structural and functional data, we first separately perform structural and functional analyses to acquire respective features utilizing feature-based techniques. For functional analysis, we apply our novel feature-based techniques on VF data. The VF test is known to detect certain minute functional deficits which may not be detected by the patients until severe vision loss has progressed [51, 68]. Also, it is known to be difficult to differentiate the true VF deficits from the variability caused by the patient response fluctuations. Hence, in this work, we investigate quantitative feature-based

techniques on the labeled VF data vectors for detection of glaucoma. We first label the VF data according to our labeling methodology and the labeled VF data are converted into 1D data vectors. Then the labeled VF data vectors are stacked into a matrix for further processing.

For structural analysis, we analyze both 1D and 2D RNFL eye scan data. For 1D RNFL analysis, we use 1D temporal, superior, nasal, inferior, and temporal (TSNIT) graph, which is RNFL thickness data acquired by scanning laser polarimetry around the parapapillary retina area. A TSNIT graph shows a unique double-hump pattern due to a much greater number of ganglion cells and their axons entering the optic disc superiorly and inferiorly. Hence, we utilize our novel feature-based techniques on 1D TSNIT RNFL data for 1D structural analysis. For 2D RNFL assessment, we investigate 2D feature-based techniques on specific regions of interest (ROIs) such that ROIs may better represent the glaucomatous damages.

In any data processing, 2D image data provides more information than 1D data vectors [77]. By utilizing real 2D eye scan image data, we may be able to fully exploit the whole 2D image data. It has been shown that the standard methods and other feature-based techniques have been applied only on 1D TSNIT RNFL data [5-8]. Consequently, we investigate the 2D feature-based techniques on real 2D RNFL image data. For 2D RNFL assessment, we investigate 2D feature-based techniques on specific regions of interest (ROIs) such that ROIs may better represent the glaucomatous damages. To obtain such ROIs, we first take the squares that include the surrounding areas of the optic disc. We then exclude the squares that include the optic disc, since the features from the optic disc

do not contain useful information. We then apply fractal analysis (FA) using piecewise triangular prism surface area (PTPSA) method to acquire fractal dimension (FD) features.

Finally, we investigate a novel selective feature-based fusion method using the results from structural and functional analyses that exploit respective features. For this novel selective fusion task, we obtain the topographic correspondence between the structural and functional data utilizing the mapping definition table. The mapping definition table divides the corresponding structural and functional data into 10 clusters respectively. Utilizing the mapping definition table, we then obtain the cluster-wise correlation coefficients between structural and functional data. Such coefficients can be regarded as the strength of correspondence. We use the cluster-wise strength of correspondence as the global coefficients to weight corresponding structural and functional data for emphasizing the areas of significance in the clusters. We then select only the clusters that are more emphasized than others and discard the rest of the clusters. We also extract respective fractal analysis (FA) features from the selected clusters of both structural and functional data. Next we append the fractal analysis (FA) features from the functional data to those from the structural data. We compute the classification performance of our feature-based selective fusion method for improved glaucoma detection.

The rest of the chapter is organized as follows: In section 5.2, the detail methods of feature-based functional analysis using labeling methodology, feature-based real 2D structural analysis and a selective fusion method on structural and functional data are provided. Section 5.3 presents the experimental results and performance evaluation of the proposed techniques. Finally, conclusion is given in section 5.4.

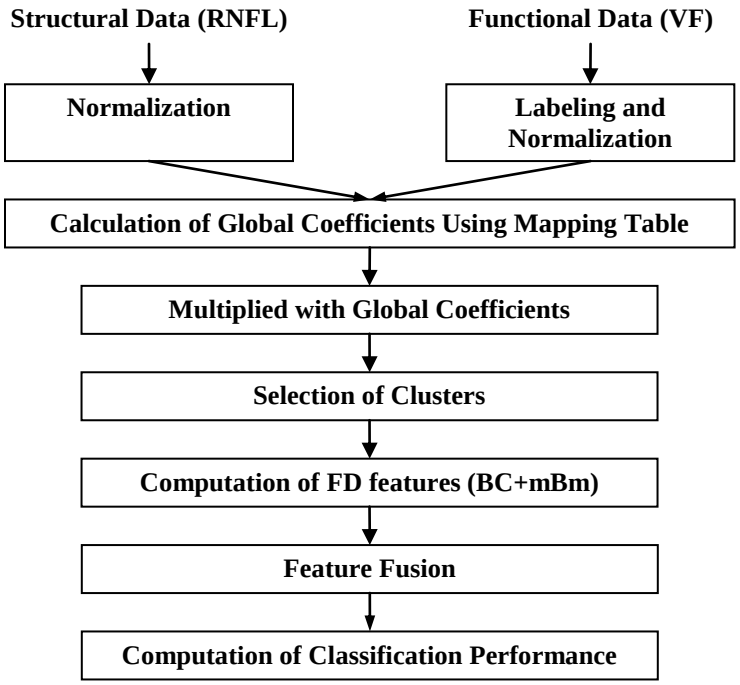

Figure 5-1. The flowchart of our selective feature-based fusion method using fractal features from structural and functional data for glaucoma detection

5.2. Methods

Figure 5-1 shows the overall flowchart of our selective feature-based fusion method using fractal features from structural and functional data for improved glaucoma detection. In this work, we use 154 eyes (85 right and 69 left; 77 glaucomatous and 77 ocular normal patients; 59 male and 95 female). Average age for these 154 patients is 57.06 with a standard deviation of 11.82. The glaucomatous and ocular normal patient groups are matched for age and the difference in age between them was significant (independent samples t-test $t = -2.13$, $p = 0.036$). We perform statistical analysis by calculating sensitivity, specificity and AUROC. For complete comparison, we compare our performance with those of existing feature-based techniques such as WFA and FFA. We briefly discuss each step in Fig. 5-1 below.

5.2.1. Functional Analysis

5.2.1.1. Labeling Methodology

Our functional analysis begins by labeling the VF sensitivities at each of 59 locations in our novel labeling methodology. For the labeling methodology, we arrange the entire 59 VF points corresponding to the visual sensitivities into 1D data vectors by labeling and regrouping them with our pre-determined labeling indices. For labeling the VF points, Ferreras *et al*. report using a raster scan labeling for the VF data acquired by Humphrey perimeter as shown in Fig. 5-2 [98]. In this labeling, the test pattern has 52 points and the points have been labeled either from right to left or from left to right. Then the next downward lines follow the previous steps.

Unlike other labeling such as a raster scan method [98], we label VF points in a clockwise fashion for the left eyes and counterclockwise for the right eyes. This labeling is consistent with that proposed in Strouthisdis *et al.* [99]. In Fig. 5-3, our novel labeling methodology of 59 VF test points is shown. In Fig. 5-3, the labeling starts from the center point. We follow the labeling from the center point to the point that is located either in 45° for the left eye or 135° for the right eye. We follow in the subsequent points in a clockwise fashion for the left eye and in a counterclockwise fashion for the right eye. Once the labeling is done, all the VF points of a specific patient are obtained in a vector form. These VF data vectors are stacked together for all the patients.

		4	3	2	1			
	10	9	8	7	6	5		
18	17	16	15	14	13	12	11	
26		25	24	23	22	21	20	19
34		33	32	31	30	29	28	27
42	41	40	39	38	37	36	35	
	48	47	46	45	44	43		
		52	51	50	49			

(a)

			1	2	3	4		
		5	6	7	8	9	10	
	11	12	13	14	15	16	17	18
19	20	21	22	23	24	25		26
27	28	29	30	31	32	33		34
	35	36	37	38	39	40	41	42
		43	44	45	46	47	48	
			49	50	51	52		

(b)

Figure 5-2. Numbering of 24-2 Swedish Interactive Threshold Algorithm (SITA) standard automated perimetry (SAP) test [98]

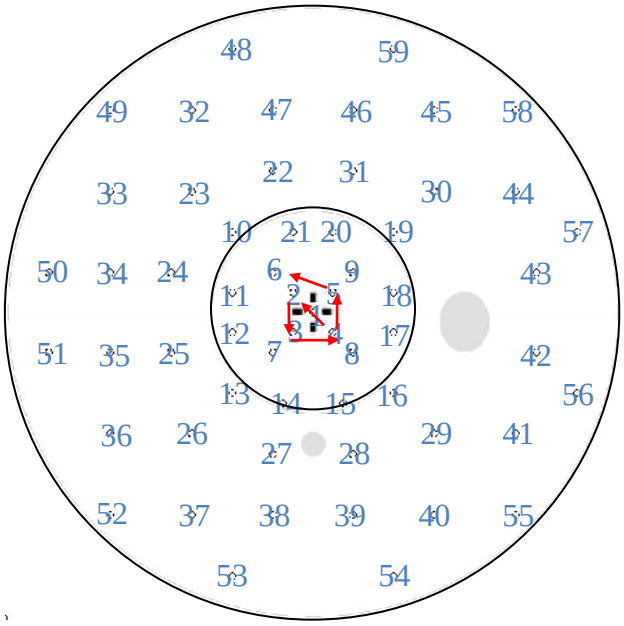

Figure 5-3. The proposed labeling of Octopus VF points in our work

5.2.1.2. Evaluation of Feature-based Techniques on VF Data Vectors

After extracting the VF data vectors, we apply our novel fractal feature-based techniques on the VF data vectors to acquire fractal dimension (FD) features. The FD

features obtained by using a BC method are appended on top of the FD features obtained by mBm method. Once the FD features are acquired, we use PCA for feature dimensionality reduction. We then obtain a Fisher's LDA classifier using the reduced FD feature dataset. The LDA classifier is trained with 90% of data while we use the rest 10% of data for testing. For checking the validity of this classifier, we take advantage of 10-fold cross validation and estimate the statistical performance. The results are then averaged over the 10 folds to produce a single AUROC estimation. The sensitivity and specificity are calculated using a statistical software, known as IBM SPSS Statistics 18.

5.2.2. Real 2D Structural Analysis

5.2.2.1. 1D TSNIT RNFL Analysis

For 1D structural analysis, we analyze 1D TSNIT RNFL data acquired by scanning laser polarimetry (SLP). In this analysis, there are 213 study participants (108 glaucoma and 105 ocular normal patients). However, for complete comparison with functional analysis and fusion method, we only use 154 out of 213 study participants (77 glaucoma and 77 ocular normal patients). For 1D TSNIT RNFL analysis, the details of the fractal/multi-fractal techniques are shown in the section 4-2. We compute sensitivity, specificity and AUROC for our feature-based technique and other existing feature-based techniques, such as FFA and WFA.

Table 5-1. Comparison of AUROC and the number of coefficients. The * represent following: *@ 27th feature vector; †@ 28th feature vector; ‡@ 8th feature vector

ROI	AUROC (FFA)	AUROC (WFA)	AUROC (FA)	# of Coefficients		
				(FFA)	(WFA)	(FA)
47x47	0.88	0.84	0.86	1105	836	36
51x51	0.91	0.89	0.91	1301	983	49
53x53	0.91	**0.94†**	0.91	1405	1061	49
55x55	**0.92***	0.92	0.93	1513	1142	49
59x59	0.91	0.90	0.93	1741	1313	64
63x63	0.91	0.90	**0.95‡**	1985	1496	64
67x67	0.89	0.93	0.94	2245	1691	81
71x71	0.90	0.93	0.92	2521	1898	81
75x75	0.90	0.94	0.92	2813	2117	100
79x79	0.92	0.92	0.92	3121	2348	100
83x83	0.91	0.92	0.92	3445	2591	121

Table 5-2. Comparison of the elapsed times. The *,† and ‡ represent following the corresponding box sizes in Table 5-1 that provide best AUROC

ROI	Elapsed Times								
	(FFA)			(WFA)			(FA)		
	Feature Extract-ion	Feature Selection	Total Time	Feature Extract-ion	Feature Selection	Total Time	Feature Extract-ion	Feature Selection	Total Time
47×47	2.24	397.81	400.05	2.29	243.15	245.44	89.11	23.60	112.71
51×51	2.79	542.97	545.76	2.64	317.26	319.90	121.88	24.36	146.24
53×53	2.96	618.62	621.58	2.90	382.47	385.37†	124.58	24.26	148.84
55×55	3.11	697.73	700.84*	3.00	418.73	421.73	123.58	24.26	147.84
59×59	3.63	920.67	924.30	3.45	555.00	558.45	159.08	25.72	184.80
63×63	4.00	1167.26	1171.26	3.90	708.67	712.57	161.76	25.54	187.30‡
67×67	4.86	1487.40	1492.26	4.39	806.91	811.30	200.62	27.83	228.45
71×71	5.52	1877.64	1883.16	4.91	1097.39	1102.30	200.13	27.79	227.92
75×75	5.65	2342.99	2348.64	5.33	1349.27	1354.60	246.86	30.91	277.77
79×79	6.82	2878.96	2885.78	6.11	1629.35	1635.46	250.10	31.34	281.44
83×83	7.57	3518.53	3526.10	6.73	1985.65	1992.38	298.73	35.59	334.32
Total	**49.15**	**14650.58**	**14699.73**	**45.65**	**9493.85**	**9539.50**	**1976.43**	**301.20**	**2277.63**

5.2.2.2. Real 2D RNFL Analysis

For 2D structural analysis, we first find an ROI that provides the best classification performance using real 2D RNFL data. The size of real 2D RNFL image

data is 256×128, which are 32,768 pixels. However, not all of the pixel information may be useful. Figure 5-4 shows average RNFL images (55×55) that include the optic disc for 2D glaucomatous and ocular normal patients. Note in Fig. 5-4 that the average 2D RNFL images for glaucomatous patients are different from those for ocular normal patients. Hence, we investigate the ROIs from the original 2D RNFL (256×128) images for the best performance. We choose box-shaped ROIs for ease of data processing. Further, we use piecewise triangular prism surface area (PTPSA) method for fractal feature extraction [30]. The detailed algorithm to compute the FD using the PTPSA method is shown in Fig. 5-5.

According to GDx-VCC manual [101], the default calculation circle for TSNIT, which has a form of a band, is centered on the optic disc. The inner diameter of the band is 2.4 mm, the outer diameter of the band is 3.2 mm, and the band is 0.4 mm wide. Since one pixel is equivalent to 0.0465 mm, the inner diameter is equivalent to 52 pixels and the outer diameter is 70 pixels. Using this information, in Table 5-2, the AUROC is compared as the box size is increased in the step of 4 pixels from the box size of 47×47 to that of 83×83 where the centers of the ROIs are aligned with those of the optic discs. Note in Table 5-1 that the box sizes that generate the highest AUROC for FFA, WFA and FA are 55×55, 53×53 and 63×63 respectively. These box sizes are within between the inner diameter pixel size (52) and the outer diameter pixel size (70). We study the effect of less number of coefficients needed for FA further. Table 5-2 compares the elapsed time for the feature-based techniques. In Table 5-2, it is shown that total elapsed time for best AUROC performance for FA is about 50% of that for WFA and 25% of that of FFA

respectively. Thus, it is shown that FA performs with less number of features and less computational complexity.

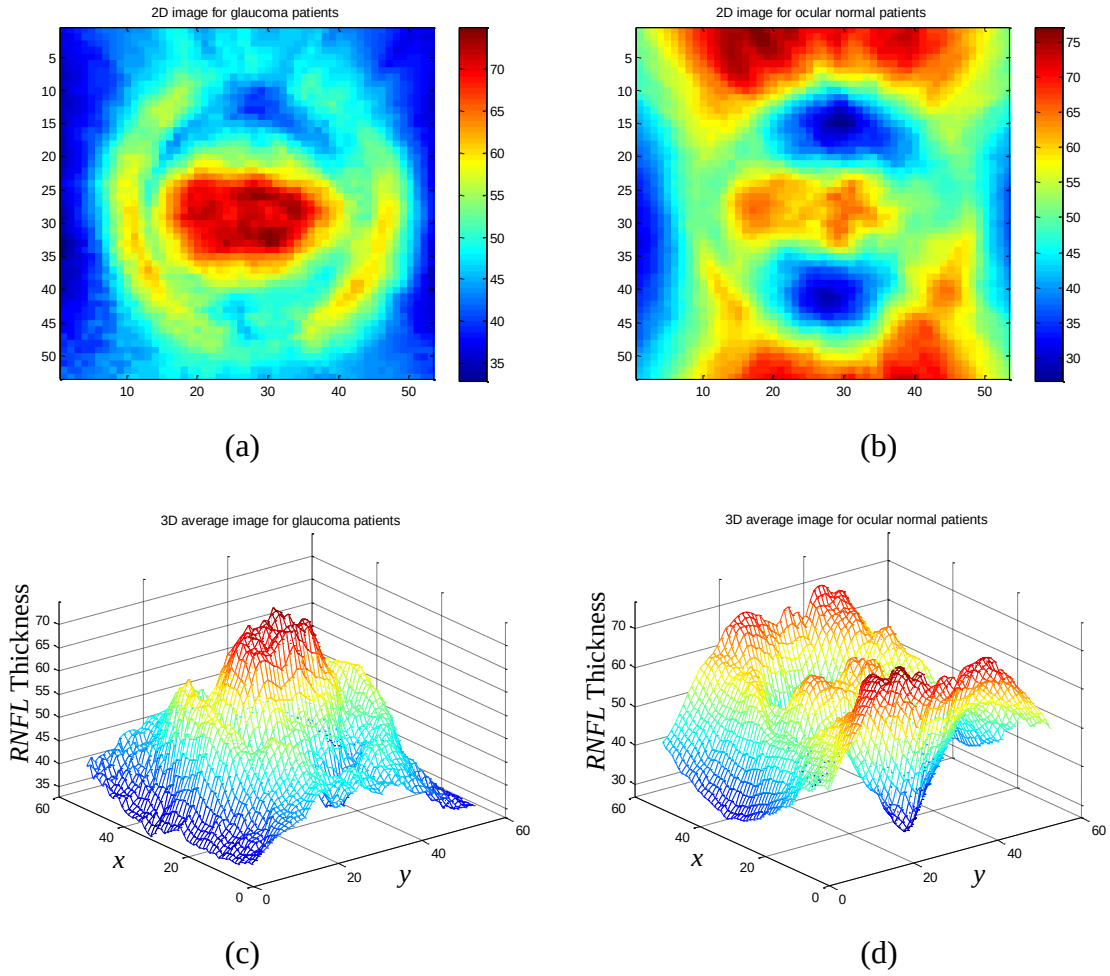

Figure 5-4. Average RNFL images (55×55) that include optic disc for (a) 2D glaucomatous (b) 2D ocular normal (c) 3D glaucomatous (d) 3D ocular normal patients

Based on the findings in Table 5-2, we first obtain the squares that include the surrounding areas of the optic disc. We then exclude the squares that include the optic disc, since the features from the optic disc do not contain useful information. For this task, we measure all the optic disc sizes from 154 study participants. Since the largest

optic disc diameter is 48, we select 48×48 as the common inner box size. The largest possible outer box size is according to the shortest distance from the position of the centroids of the optic discs, which is 48 and is doubled for preventing overlapping.

Algorithm 3

for *each sub-image*

Divide sub-image into boxes of size n × n

for *each box of size n × n*

Find the surface area of the four triangles formed by treating gray value as the third dimension and connecting the four corner points with the center point and each other.

Sum surface areas for entire sub-image

FD = log(*sum of surface areas*)/log(*n*)

Figure 5-5. Pseudo code for piecewise triangular prism surface area (PTPSA) method

Hence, the resulting outer box size is 96×96. To make it symmetric, we choose an odd number of box size. Hence, the inner box size of 47×47 is selected while the outer box size of 95×95 is selected. An example for a patient is shown in Fig. 5-6.

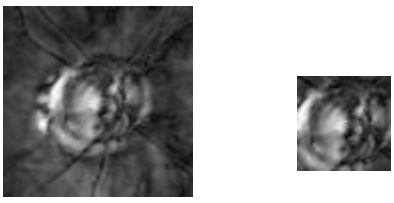

(a) (b)

Figure 5-6. An example of a patient (a) outer box (95×95) (b) inner box (47×47)

6.99	6.91	7.05	7.07	7.13	7.09	6.94	6.95	7.07	7.28	6.88	6.95
6.86	6.83	6.97	7.10	7.22	7.07	6.91	6.92	7.17	7.05	7.26	7.27
6.77	6.61	6.87	7.20	7.37	7.30	7.10	7.43	7.14	7.28	7.09	6.94
6.70	6.53	6.61	7.17	7.30	7.25	7.01	7.32	7.16	7.04	6.82	6.70
6.69	6.39	6.46	6.95	6.85	7.09	7.23	7.45	7.25	6.72	6.65	6.66
6.49	6.43	6.68	6.78	7.28	7.69	7.67	7.71	7.73	6.80	6.77	6.67
6.70	6.52	6.60	6.92	7.01	7.84	7.54	7.60	7.61	6.96	6.66	6.72
6.66	6.36	6.59	6.93	7.40	6.95	7.32	7.53	7.56	6.45	6.69	6.68
6.83	6.66	6.63	7.13	7.38	7.45	7.48	7.29	7.05	6.91	6.74	6.66
6.66	6.68	7.02	7.19	7.24	7.29	7.35	7.12	7.24	6.98	6.79	6.65
6.84	6.90	6.95	7.17	7.19	7.22	7.36	7.23	7.33	7.32	6.84	6.60
6.91	6.84	7.08	7.15	7.20	7.18	7.29	7.14	7.05	7.35	7.04	6.64

(a)

7.17	7.30	7.25	7.01	7.32	7.16
6.95	6.85	7.09	7.23	7.45	7.25
6.78	7.28	7.69	7.67	7.71	7.73
6.92	7.01	7.84	7.54	7.60	7.61
6.93	7.40	6.95	7.32	7.53	7.56
7.13	7.38	7.45	7.48	7.29	7.05

(b)

Figure 5-7. FA (PTPSA) features from (a) the outer box (b) the inner box optic disc area

Based on these box sizes, the feature-based techniques such as FFA, WFA and FA are applied on the real 2D RNFL data. For FFA and WFA, we subtract the resulting 2D FFA and 2D WFA features of the inner boxes from those of the outer boxes, with the center points aligned using a shift function. The features from the inner box that corresponds to optic disc area are subtracted since optic disc does not contain any

information about glaucoma. After adjustment for the optic disc area, we obtain PCA and LDA classifiers for FFA and WFA features respectively.

For FA, the 2D fractal dimension (FD) features are obtained based on 8×8 block processing. Figure 5-7 shows an example of the FD features acquired from the outer box (95×95) and the inner box (47×47) respectively for a glaucomatous patient. Note in Fig. 5-7 the FD features acquired from the inner box are the exactly same as the central portion of the FD features acquired from the outer box. Figure 5-8 is the effective ROI for this study.

6.99	6.91	7.05	7.07	7.13	7.09	6.94	6.95	7.07	7.28	6.88	6.95
6.86	6.83	6.97	7.10	7.22	7.07	6.91	6.92	7.17	7.05	7.26	7.27
6.77	6.61	6.87	7.20	7.37	7.30	7.10	7.43	7.14	7.28	7.09	6.94
6.70	6.53	6.61							7.04	6.82	6.70
6.69	6.39	6.46							6.72	6.65	6.66
6.49	6.43	6.68							6.80	6.77	6.67
6.70	6.52	6.60							6.96	6.66	6.72
6.66	6.36	6.59							6.45	6.69	6.68
6.83	6.66	6.63							6.91	6.74	6.66
6.66	6.68	7.02	7.19	7.24	7.29	7.35	7.12	7.24	6.98	6.79	6.65
6.84	6.90	6.95	7.17	7.19	7.22	7.36	7.23	7.33	7.32	6.84	6.60
6.91	6.84	7.08	7.15	7.20	7.18	7.29	7.14	7.05	7.35	7.04	6.64

Figure 5-8. FA (PTPSA) features of the ROI that subtract those from the inner box

After the 2D FD features are obtained, we obtain PCA for dimensionality reduction and obtain LDA classifiers for the final classification task.

5.2.3. Selective Feature-based Fusion of Structural and Functional Data

In this section, we first study the cluster-wise structural and functional relationship for selective feature-based fusing for improved glaucoma detection. Fig. 5-9 shows a mapping between the 1D 64-point TSNIT RNFL data and 59 VF test points in 10 clusters according to the polar angle segmentation, explained in Table 5-3 [102]. In order to show an example mapping, the 1st RNFL zone (0-70°) is associated with the four VF points in the 1st VF cluster as shown in Fig. 5-9. Note that while polar angle analysis is done in a clock-wise way, the clusters are labeled in a counter-clock-wise way due to the fact that the RNFL defects and VF defects are vertically mirrored. Table 5-3 is the mapping definition table that contains the actual VF points in each cluster.

To ascertain the degree of the association between the clusters of the 1D TSNIT RNFL and VF data, we obtain the scatter plots between the 1D TSNIT RNFL and VF data for 154 patients. We show the corresponding 10 clusters in Fig. 5-10. On each cluster scatter plot, linear regression analysis has been done to analyze the association between the 1D TSNIT RNFL and VF data. Linear regression analyses indicate that there are positive trends in 2nd, 9th, 4th, 3rd and 7th clusters while there is a negative trend in 8th cluster. We then compute the degree of the association for each cluster using Pearson's correlation coefficients. Figure 5-11 (a) shows the different degrees of association on the different clusters. We select four clusters that are most related based on Pearson's coefficients. We then discard the information in the other clusters and utilize only 2nd, 3rd, 8th, and 9th clusters that are weighted with the global coefficients as shown in Fig. 5-11 (b) (c). Therefore we use 40% of RNFL TSNIT and VF data for the rest of this work.

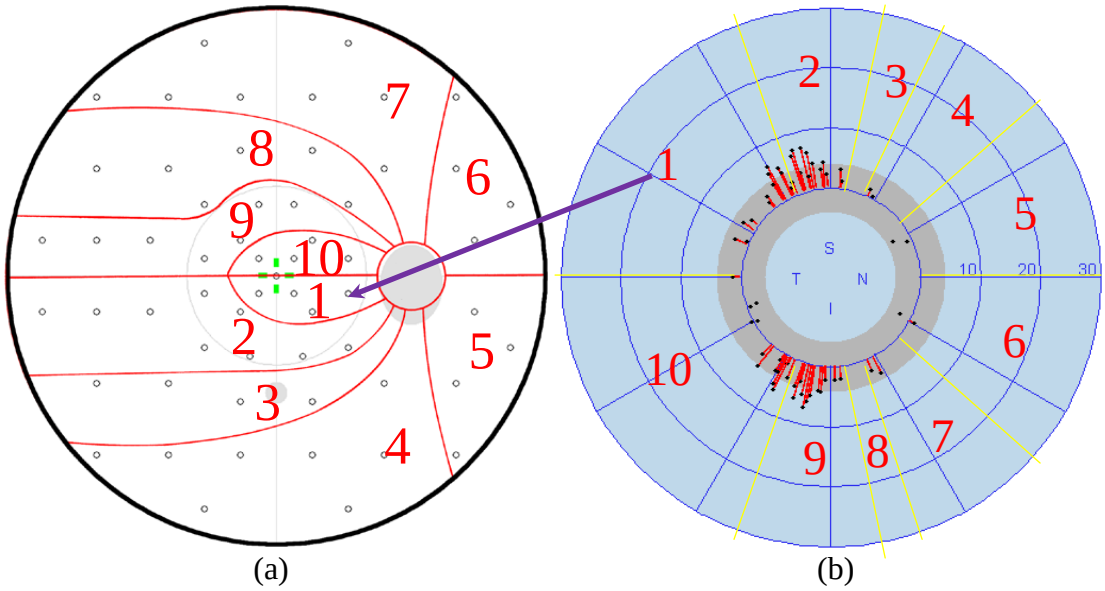

(a) (b)

Figure 5-9. (a) VF clusters (b) Corresponding optic disc polar angle sections [102]

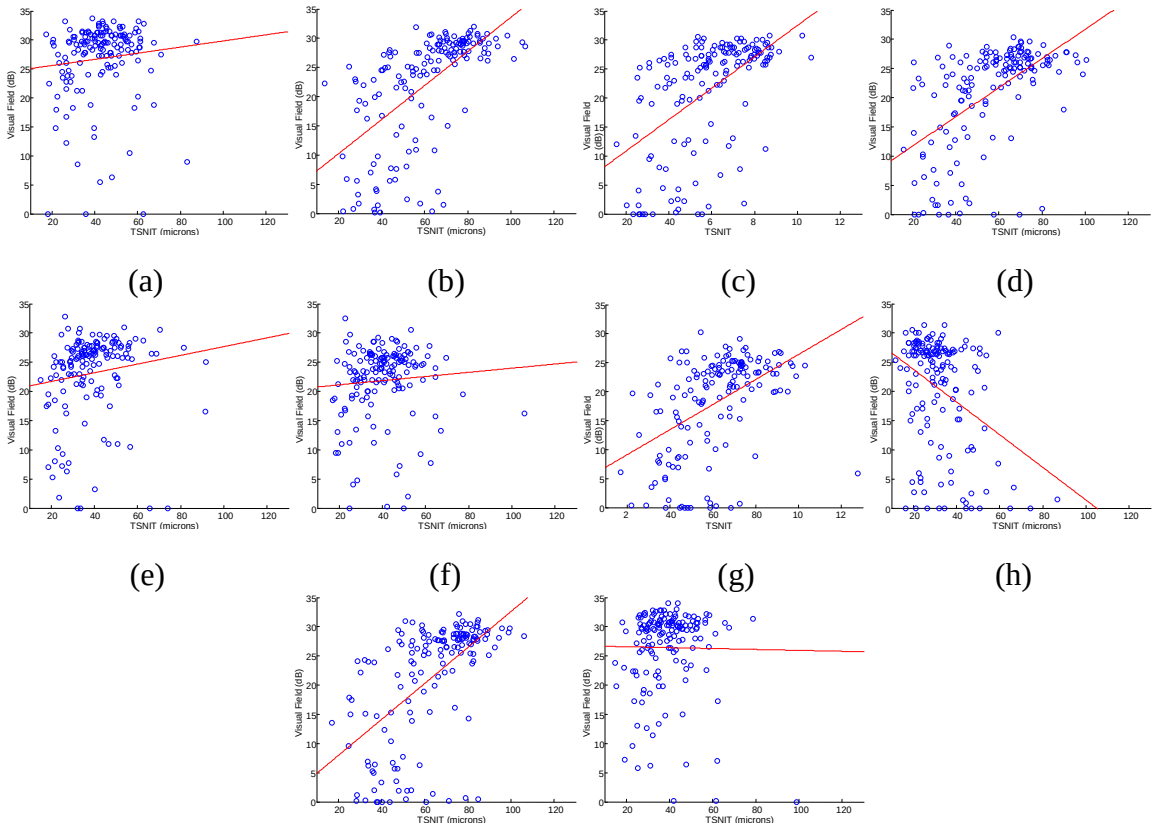

(a) (b) (c) (d)

(e) (f) (g) (h)

(i) (j)

Figure 5-10. Scatter plots showing the association between the TSNIT measured by SLP and VF measured by SAP in each cluster.

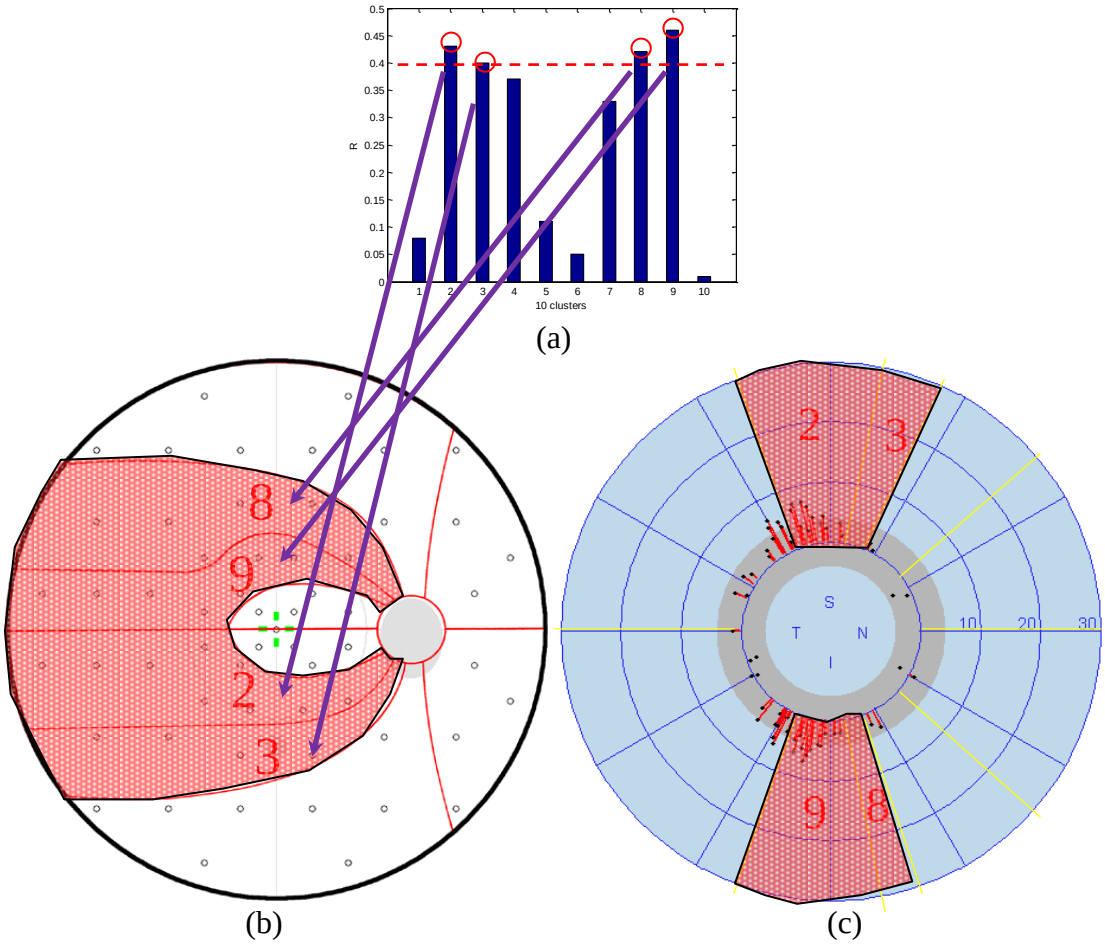

Figure 5-11. (a) Global coefficients for each cluster (b) the selected VF clusters (c) the selected TSNIT clusters

Table 5-3. Cluster (or Mapping) definition table using the RNFL angles and the corresponding VF points [102]

Cluster #	Polar Angle Start	Polar Angle End	Corresponding VF points
1	0	70	3,4,8,17
2	71	102	7,12,13,14,15,16,25,35,51
3	103	116	26,27,28,36
4	117	140	29,37,38,39,40,52,53,54
5	141	179	41,42,55,56
6	181	222	43,44,57,58
7	223	250	30,32,45,46,47,48,49,59
8	251	257	10,19,22,23,31,33
9	258	290	6,11,20,21,24,34,50
10	291	359	1,2,5,9,18

5.3. Results and Discussions

5.3.1. Functional Analysis

Figure 5-12 shows the VF data points from the normal and glaucomatous eyes (right and left) for all 154 eyes. As discussed earlier, these VF data points have been labeled and plotted separately for comparison purpose. Note in Figs. 5-11 (b), (d), (f) and (h) the right and left eyes in each group (i.e., normal and glaucomatous eyes) have similar shapes respectively. For normal eyes, as shown in Figs. 5-11 (a) and (c), the plots show monotonically decreasing values without much variation. However, the shape of glaucomatous eyes have very different values than that of normal eyes as shown in Figs. 5-11 (e) and (g) wherein there are considerable irregularity and abrupt changes. Such differences and changes in the shape of the VF data points between normal and glaucomatous eyes justify the use of the feature-based techniques such as FFA, WFA and FA.

Figure 5-13 shows the comparison of ROC curves for the feature-based methods in our functional analysis. Note in Fig. 5-13 our fractal/multi-fractal feature-based technique performs the best among all other feature-based techniques. Table 5-4 shows the comparison of sensitivity, specificity and AUROC for FFA, WFA and FA (the combined BC and mBm method) in the same functional analysis. In Table 5-4, our fractal/multi-fractal feature-based technique performs the best among all feature-based techniques with corresponding AUROC of FFA, WFA and FA (the combined BC and mBm method) being 0.87, 0.87 and 0.95 respectively. In this analysis, the FA offers the highest AUROC and is significantly different when compared to the FFA and WFA using DeLong *et al.*'s method [91], for p = 0.03 and 0.006 respectively. The best performance of

fractal/multi-fractal features demonstrates that embedded irregularity and randomness have been well characterized. Hence, our novel FA technique outperforms other feature-based techniques such as FFA and WFA by the margin of 8% in the functional analysis. However, this result does not match the performance of using the mean deviation (MD) method. The AUROC of the MD is 0.98. There are several possible reasons why our proposed feature-based results may not be as good as using the MD method. First, the patient group we study may not reflect enough local variation or randomness in their original VF data. Hence, a global index such as the MD performs well while feature-based techniques such as FFA, WFA or FA may not perform. Second, even with the novel labeling methodology, the VF data vectors may not contain structural information in the case of the RNFL. Consequently, the performance may not be comparable. To address this issue, we plan to utilize the topographic correspondence between structural and functional data to fuse useful information from both domains for improved glaucoma detection.

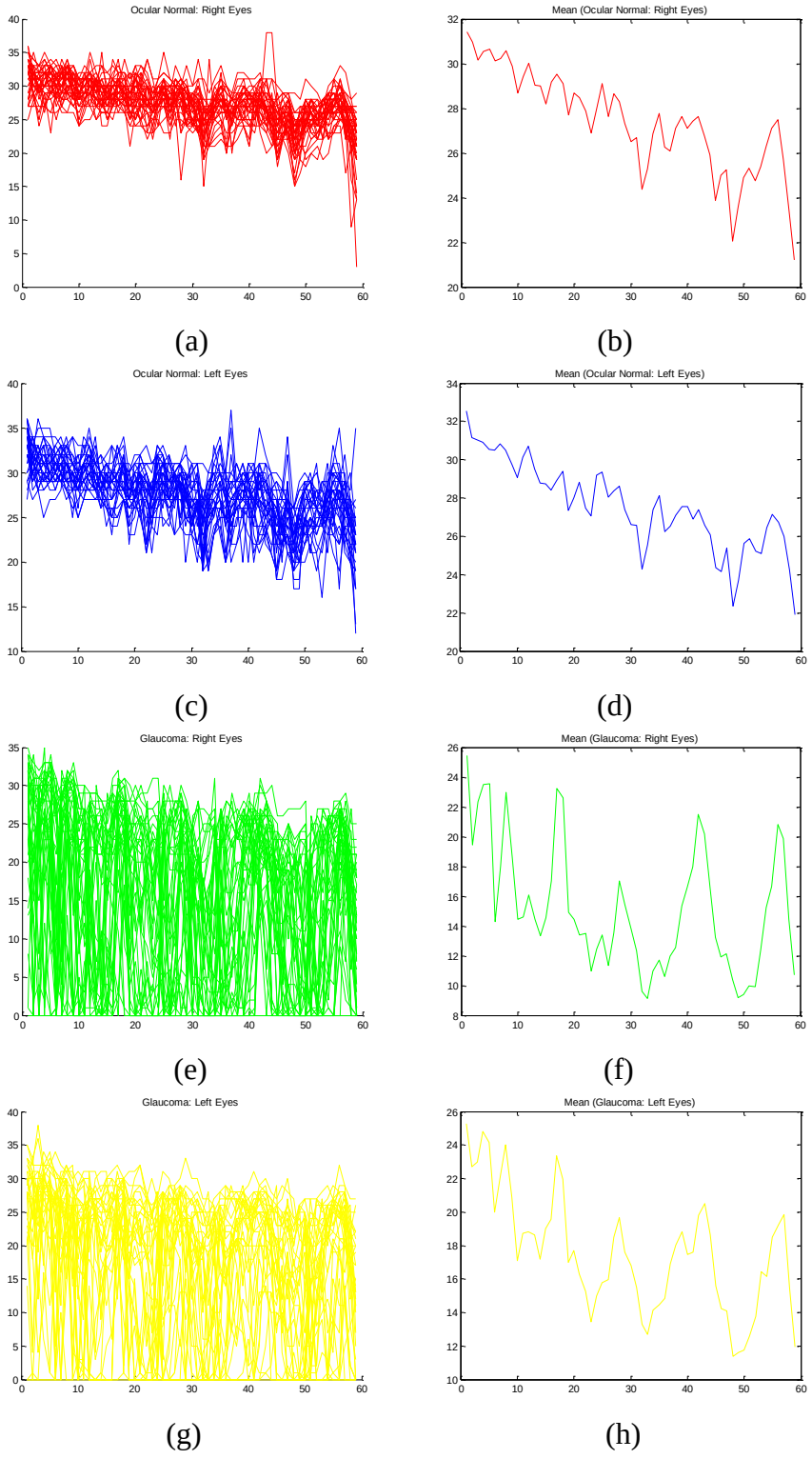

Figure 5-12. 1D Visual field (VF) plotting for (a) normal right eyes (b) the mean value of the normal right eyes (c) normal left eyes (d) the mean value of the normal left eyes (e) glaucomatous right eyes (f) the mean value of the glaucomatous right eyes (g) glaucomatous left eyes (h) the mean value of the glaucomatous left eyes

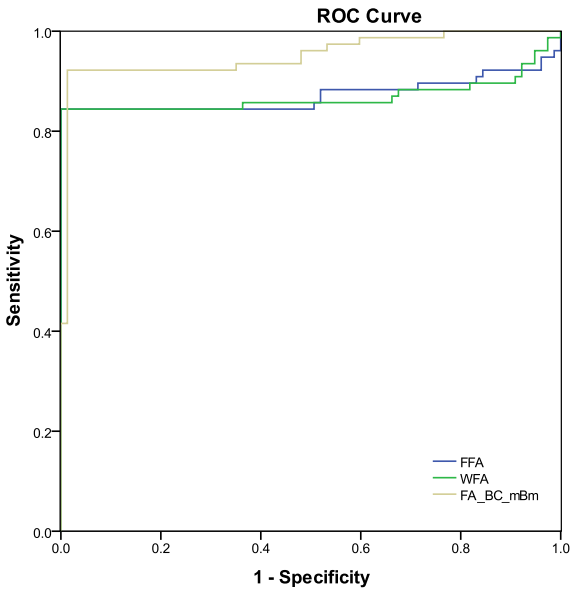

Figure 5-13. The comparison of ROC curves for FFA, WFA and FA (BC+mBm) in functional analysis

Table 5-4. The comparison of sensitivity, specificity and AUROC for functional analysis

Methods	(Sensitivity/Specificity/**AUROC**) (Sensitivity at 80; Sensitivity at 90)
FFA	0.84/0.99/**0.87** (0.84; 0.84)
WFA	0.84/0.99/**0.87** (0.84; 0.84)
FA (BC+mBm)	0.92/0.99/**0.95** (0.92; 0.92)

5.3.2. Structural Analysis

In this section, we use our novel FD along with FFA and WFA features for 1D and 2D RNFL structural analysis. Table 5-5 shows the comparison of AUROC for 1D RNFL structural analysis while Table 5-6 shows that of 2D RNFL structural analysis. We use the same PTPSA method for computing FD in this analysis. We then compute the AUROC that discriminates between glaucoma and ocular normal patients with selected

the classifiers based on FFA, WFA and FA features extracted from the ROIs of real 2D RNFL image data. Note both 1D and 2D RNFL data analyses, even with our novel fractal features from real 2D RNFL image data, are not comparable to 0.94 AUROC of the standard machine method known as the Nerve Fiber Index (NFI). There may be several reasons for this. First, literature review shows that real 2D RNFL image may not better represent the characteristic of glaucoma than 1D TSNIT RNFL [5-8].

Table 5-5. Comparison of AUROC for 1D TSNIT RNFL analysis

Methods	(Sensitivity/Specificity/**AUROC**) (Sensitivity at 80; Sensitivity at 90)
FFA	0.87/0.93/**0.89** (0.87; 0.87)
WFA	0.87/0.93/**0.91** (0.87; 0.87)
FA	0.90/0.92/**0.91** (0.94; 0.73)

Table 5-6. Comparison of AUROC for real 2D RNFL analysis without optic disc

Methods	(Sensitivity/Specificity/**AUROC**) (Sensitivity at 80; Sensitivity at 90)
	(without optic disc)
FFA	0.92/0.92/**0.91** (0.95; 0.92)
WFA	0.88/0.87/**0.91** (0.90; 0.81)
FA	0.92/0.90/**0.92** (0.95; 0.90)

Second, we choose specific ROIs for real 2D analysis as square shape while the better representation may be circular shape. Since separate feature-based analyses of VF

and RNFL data do not offer better glaucoma detection performance, we investigate fusion analysis of these data next.

5.3.3. Selective Feature-based Fusion Analysis

We first plot 1D TSNIT RNFL and VF data and corresponding mean values in Fig. 5-14. As can be seen in Fig. 5-14 (b)(d), neither of glaucomatous 1D TSNIT RNFL or VF data is distinct in its shapes. For fusion, we then multiply each signal and the mean values in Fig. 5-14 with Pearson's correlation coefficients. Figure 5-15 shows the plots of 1D TSNIT RNFL and VF data after the multiplication with the Pearson's correlation coefficients.

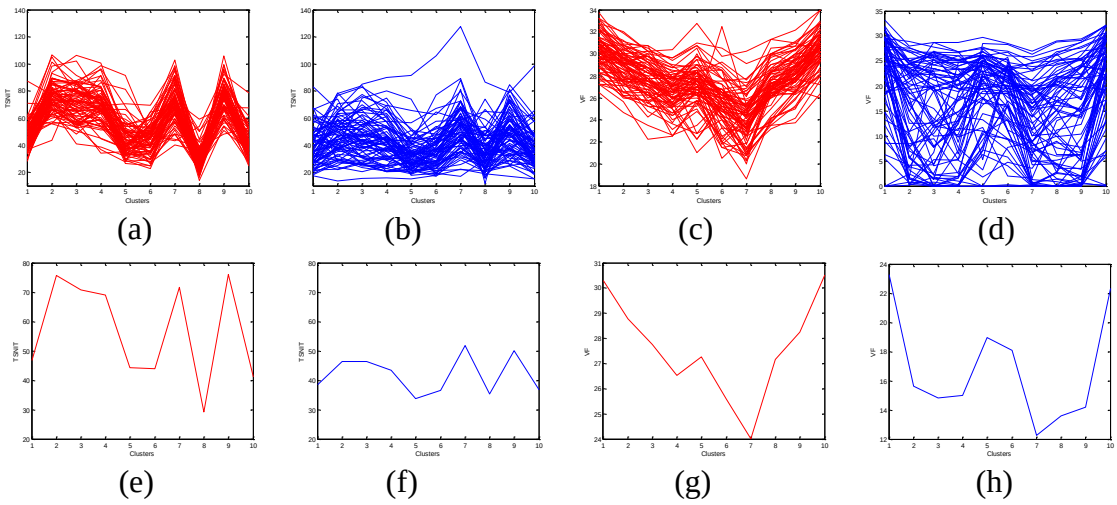

Figure 5-14. Clusters for (a) TSNIT (Normal) (b) TSNIT (Glaucoma) (c) VF (Normal) (d) VF (Glaucoma); Mean values for (e) TSNIT (Normal) (f) TSNIT (Glaucoma) (g) VF (Normal) (h) VF (Glaucoma)

This simple fusion method emphasizes the more informative areas in both 1D TSNIT RNFL and VF data, making them distinctly display double hump patterns as

shown in Fig. 5-15. We then extract FFA, WFA and FA features from the weighted structural and functional data as shown in Fig. 5-15. The respective features from the functional data are appended to those from the structural data. We compare the AUROCs of the fusion methods on the feature-based techniques and include the performance of the raw data performance for complete comparison.

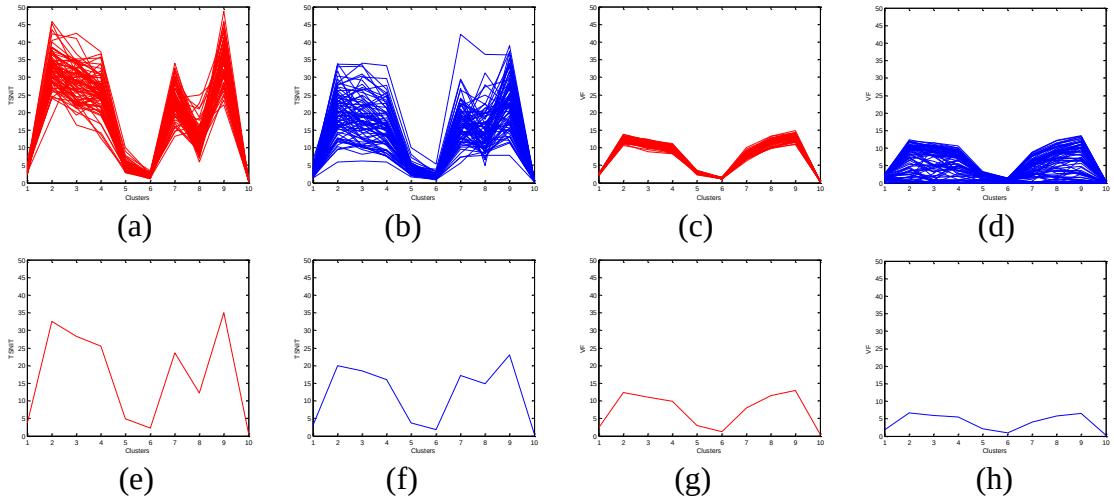

Figure 5-15. Clusters multiplied by R values for (a) TSNIT (Normal) (b) TSNIT (Glaucoma) (c) VF (Normal) (d) VF (Normal); Mean values for (e) TSNIT (Normal) (f) TSNIT (Glaucoma) (g) VF (Normal) (h) VF (Normal)

For complete comparison, we first show the results from simple fusion of structural and functional data. The AUROCs of structural, functional and a simple fusion method and a selective fusion method for raw, FFA, WFA and FA are shown in Table 5-7. Table 5-7 shows that all of simple fusion methods on raw, FFA, WFA and FA enhance the classification performance. Specifically, simple fusion of FA features from the structural and functional data offers 0.98 AUROC, which is comparable to using only the MD. Next we show that our novel selective fusion method using FA features outperforms

all feature-based and MD methods with AUROC of 0.99. It is obvious that not much can be improved in classification performance from AUROC of 0.98 for the MD method. However, it is important to not that we achieve improved glaucoma detection performance with fusion of only 40% of VF and RNFL data.

Table 5-7. Comparison of AUROC of structural, functional and their selective fusion for raw, FFA, WFA and FA after the cluster-wise multiplication of Pearson's correlation coefficients

Methods	(Sensitivity/Specificity/**AUROC**) (Sensitivity at 80; Sensitivity at 90)			
	Structural (RNFL)	**Functional (VF)**	**Fusion of all VF and RNFL data**	**Selective fusion of 40% VF and RNFL data**
Raw	0.84/0.91/**0.94** (0.92; 0.84)	0.78/0.99/**0.92** (0.88; 0.79)	0.87/0.97/**0.96** (0.92; 0.90)	0.96/0.90/**0.98** (0.96; 0.95)
FFA	0.87/0.90/**0.94** (0.90; 0.84)	0.78/0.96/**0.92** (0.88; 0.79)	0.86/0.99/**0.96** (0.96; 0.87)	0.96/0.94/**0.98** (0.97; 0.96)
WFA	0.84/0.95/**0.94** (0.88; 0.84)	0.84/0.99/**0.94** (0.91; 0.86)	0.87/0.94/**0.96** (0.94; 0.87)	0.94/0.94/**0.98** (0.95; 0.94)
FA	0.81/0.91/**0.90** (0.84; 0.81)	0.88/0.95/**0.93** (0.88; 0.88)	0.92/0.94/**0.98** (0.97; 0.92)	0.91/0.99/**0.99** (1.00; 0.95)

5.4. Conclusion

In this chapter, we demonstrate the efficacy of selective fusion of structural and functional data for improved glaucoma detection. We first apply our labeling methodology to the VF data and perform vectorization process in order to obtain the VF data vectors. We then obtain the features from structural analysis. It is shown that our fractal analysis feature-based technique can exploit the shape features from functional data and perform the best among other feature-based techniques with corresponding AUROCs of FFA, WFA and FA being 0.87, 0.87 and 0.95 respectively. It is also shown that our proposed feature-based technique on functional analysis offers comparable

performance when compared to the MD method (0.98 AUROC). We also report a novel feature-based technique on real 2D RNFL image data based on specific ROIs. It is shown that using such ROIs, fractal-based techniques perform comparably to existing methods with AUROC of 0.92. We believe that performance of 2D RNFL method may be improved with the better representation of ROI such as using a circular shape.

We then demonstrate the efficacy of selective fusion of structural and functional data for improved glaucoma detection. For using our novel selective feature-based fusion, the global coefficients that emphasize the more informative area for 1D TSNIT RNFL and VF data are introduced. We then selectively choose 40% of data that most emphasize clusters and use only such clusters for final classification. For comparison, we compute the performance of the proposed selective feature-based fusion method and compare it with those of existing feature-based techniques such as WFA and FFA. Statistical analyses show that our selective fusion of the structural and functional data outperforms the existing WFA and FFA with AUROC being 0.98, 0.98 and 0.99 respectively. In addition, we also show that our proposed selective feature-based fusion method on structural and functional data offers better AUROC when using only MD method.

6. Conclusions and Future Works

6.1. Major Contributions

The primary goal of this dissertation is to investigate novel feature-based methods for improved glaucoma detection and progression prediction. For this goal, we exploit novel fractal/multi-fractal features, application of multi-class classification and selective feature-based fusion of structural and functional data. We propose and implement novel fractal/multi-fractal feature extraction using two types of data such as structural (RNFL) and functional (VF) data. We also develop the feature-based techniques to predict glaucomatous progression using the novel fractal/multi-fractal features. We then introduced the first novel application of multi-class classification that better predicts glaucomatous progression than the existing nonlinear methods such as neural network (NN). Finally, we also showed the first novel selective feature-based fusion of structural and functional data.

Chapter 3 describes one of the major contributions of this dissertation. In this chapter, we obtain novel fractal/multi-fractal feature extraction to capture structural changes to the RNFL. Previous works show that the Fourier coefficients and wavelet-Fourier coefficients features parameterize the shape features from the 1D TSNIT RNFL data [22-23]. Such features provide better diagnostic capability of glaucoma over the standard machine outputs of inferior average, superior average and average RNFL thickness. However, our fractal/multi-fractal features better characterize the embedded local variation and randomness in the RNFL and thus offer enhanced diagnostic capability of glaucoma with 97% AUROC. We extract novel fractal/multi-fractal features from both the 1D TSNIT RNFL data acquired by scanning laser polarimetry (SLP) and

by optical coherence tomography (OCT). There is a difference between the performances of the fractal/multi-fractal features on SLP and OCT data [33, 95]. It has been shown that the different stages of the disease and inherent difference between SLP and OCT may be accountable for such difference [95].

Another contribution of this dissertation as discussed in Chapter 4 involves the utilization of fractal/multi-fractal features for multi-class classification in predicting glaucomatous progression. We show that our novel fractal/multi-fractal features can characterize the multi-staged glaucomatous progression in structural data. We demonstrate progression prediction efficacy with 82% AUROC [96]. Another key contribution of this dissertation is the application of multi-class classification using a Gaussian kernel for classifying progressors from non-progressors and ocular normal patients. This application of multi-class SVM classifier offers better predictive capability of glaucomatous progression than the existing nonlinear techniques such as neural network (NN) with AUROCs being 88% and 77% respectively [96].

In addition, we report a feature-based functional visual field data analysis that exploits a novel labeling methodology. We also report 2D feature-based techniques to analyze real 2D RNFL image data. For our novel 2D feature-based techniques, we illustrate how to obtain ROIs for better characterizing the glaucomatous damages. The classification performance of our real 2D feature-based analysis is 92% AUROC.

The final contribution of this dissertation is the efficacy of our novel selective feature-based fusion of respective features from structural and functional data. Statistical analysis shows that this fusion method offers better performance with AUROC of 99%. To obtain a selective feature-based fusion method, global coefficients that emphasize the

more informative area for 1D TSNIT RNFL and VF data are identified. We then selectively choose 40% of structural and functional data that are representative of all clusters. We use these clusters for final classification. We then compare our performance with other existing feature-based techniques such as FFA and WFA. Hence, we demonstrate the possibility of building a novel global classifier that simultaneously detects glaucoma and predicts glaucomatous progression utilizing this selective feature-based fusion method.

In summary, this dissertation proposes novel fractal/multi-fractal feature extraction, multi-class SVM classification using a Gaussian kernel and a selective feature-based fusion method for improved glaucoma detection and glaucomatous progression prediction. The feature-based techniques that utilize novel fractal/multi-fractal features outperform the standard methods and the existing feature-based techniques in glaucoma detection. It is also shown that the proposed feature-based techniques and multi-class SVM classifiers offer enhanced diagnostic capability for glaucomatous progression prediction. Furthermore, the proposed selective feature-based fusion method shows excellent performance in glaucoma detection when compared to the existing standard mean deviation (MD) method.

6.2. Future Works

Glaucoma detection and glaucomatous progression prediction are patient-dependent techniques and are often unpredictable. In order to claim a clinically important glaucoma detector and glaucomatous progression predictor, we need to further improve our algorithms to make them less patient-dependent and more robust. This will require us

more careful investigation on feature extraction, feature selection and feature/classifier fusion.

In Chapter 3, systematic feature-based techniques for glaucoma detection on SLP and OCT data are described. For our future direction, we plan to investigate the relationship between SLP and OCT data for obtaining better glaucoma detection. In Chapter 4, the use of novel fractal/multi-fractal features and multi-class classification for glaucomatous progression is demonstrated. As a future direction of this work, other multi-class prediction methodologies can be investigated.

In Chapter 5, a novel selective feature-based fusion method is proposed that exploits both the features from structural and functional data. In evaluating the proposed method, we have found that our simple fusion scheme can achieve slightly better when compared to the existing mean deviation (MD) method. For better diagnostic capability of glaucoma, we investigate individualized coefficients that exploit correction factors for individuals. We show that the utilization of the topographic correspondence between structural and functional data, which is expressed as the global coefficients, can emphasize the more informative areas of structural and functional data respectively. For enhanced performance of glaucoma detection and glaucomatous progression prediction, a customized correction factors for individuals may be obtained for comparison with the proposed techniques. Hence, we plan to further investigate selective fusion methods that exploit the individualized coefficients.

REFERENCES

[1] Weinreb, R. N. and Khaw, P. T., "Primary open angle glaucoma," Lancet, 363, 1711-1720 (2004).

[2] Garway-Heath, D. F., Caprioli, J., Fitzke, F. W. and Hitchings, R. A., "Scaling the hill of vision: the physiological relationship between light sensitivity and ganglion cell numbers," Invest Ophthalmol Vis Sci., Vol. 41, pp. 1774–1782, (2000).

[3] Quigley, H. A., Miller, N. R. and George, T., "Clinical evaluation of nerve fiber layer atrophy as an indicator of glaucomatous optic nerve damage," Arch Ophthalmol, 98, 1564-1571 (1980).

[4] Quigley, H. A. and Addicks, E. M., "Quantitative studies of retinal nerve fiber layer defects," Arch Ophthalmol, 100, 807-814 (1982).

[5] Reus, N. J. and Lemij, H. G., "Diagnostic accuracy of the GDx VCC for glaucoma," Ophthalmology 111(10), 1860-1865 Oct. (2004).

[6] Hougaard, J. L., Heijl, A. and Bentsson, B., "Glaucoma Detection by StratusOCT," J Glaucoma, 16(3), 302-306, May. (2007).

[7] Parikh, R. S., Parikh, S. R., Kumar, R. S., Prabakaran, S., Babu, J. G. and Thomas, R., "Diagnostic capability of scanning laser polarimetry with variable cornea compensator in Indian patients with early primary open-angle glaucoma," Ophthalmology, 115(7), 1167-1172 (2008).

[8] Wollstein, G., Ishikawa, H., Wang, J. et al., "Comparison of three optical coherence tomography scanning areas for detection of glaucomatous damage," Am J. Ophthalmol., 139, 39-43 (2005).

[9] Chakraborty, S., Asher, N., Singh, R., Ramakrishnan, R., Vasudev, T. and Bacchav, A., Assessment of Retinal Nerve Fibre Layer (RNFL) Thickness in Glaucomatous and Normal Eye Using Scanning Laser Polarimetry_Gdxvcc_in South Indian Population, All India Ophthal. Soc (AIOS), 278-280 (2008).

[10] Leung, C. K., Chan, W. M., Hui, Y. L. et al., "Analysis of retinal nerve fiber layer and optic nerve head in glaucoma with different reference plane offsets, using optical coherence tomography," Invest Ophthalmol Vis Sci. 46, 891-899 (2005).

[11] Leung, C. K., Chan, W. M., Chong, K. K. et al., "Comparative study of retinal nerve fiber layer measurement by StratusOCT and GDx VCC, I: correlation analysis in glaucoma," Invest Ophthalmol Vis Sci. 46, 3214-3220 (2005).

[12] Kanamori, A., Nagai-Kusuhara, A., Escano, M. F. et al., "Comparison of confocal scanning laser ophthalmoscopy, scanning laser polarimetry and optical coherence tomography to discriminate ocular hypertension and glaucoma at an early stage," Graefes Arch Clin Exp Ophthalmol., 1, 56-68 (2006).

[13] Chen, H. Y. and Huang, M. L., "Discrimination between normal and glaucomatous eyes using Stratus optical coherence tomography in Taiwan Chinese subjects," Graefes Arch Clin Exp Ophthalmol, 243, 894-902 (2005).

[14] Budenz, D. L., Michael, A., Chang, R. T. et al., "Sensitivity and specificity of the Stratus OCT for perimetric glaucoma," Ophthalmology,112, 3-9 (2005).

[15] Kanamori, A., Nakamura, M., Escano, M. F. et al., "Evaluation of the glaucomatous damage on retinal nerve fiber layer thickness measured by optical coherence tomography," Am J Ophthalmol. 135, 513-520 (2003).

[16] Guedes, V., Schuman, J. S., Hertzmark. E., et al., "Optical coherence tomography measurement of macular and nerve fiber layer thickness in normal and glaucomatous human eyes," Ophthalmology, 110, 177-189 (2003).

[17] Bowd, C., Zangwill, L. M., Berry, C. C., et al., "Detecting early glaucoma by assessment of retinal nerve fiber layer thickness and visual function," Invest Ophthalmol Vis Sci. 42, 1993-2003 (2001).

[18] Greaney, M. J., Hoffman, D. C., Garway-Heath, D. F., Nakla, M., Coleman, A. L. and Caprioli, J., "Comparison of optic nerve imaging methods to distinguish normal eyes from those with glaucoma," Invest Ophthalmol Vis Sci, 43(1), 140-145, Jan. (2002).

[19] Zangwill, L. M., Bowd, C., Berry, C. C., et al., "Discriminating between normal and glaucomatous eyes using the Heidelberg Retina Tomograph, GDx Nerve Fiber Analyzer, and Optical Coherence Tomograph," Arch Ophthalmol. 119, 985-993 (2001).

[20] Wollstein, G., Schuman, J. S., Price, L. L., et al., "Optical coherence tomography (OCT) macular and peripapillary retinal nerve fiber layer measurements and automated visual fields," Am J Ophthalmol., 138, 218-225 (2004).

[21] Medeiros, F. A., Zangwil, L. M., Bowd, C., Vessani, R. M., Susanna, R. Jr. and Weinreb, R. N., "Evaluation of retinal nerve fiber layer, optic nerve head, and macular thickness measurements for glaucoma detection using optical coherence tomography," Am J Ophthalmol., 139(1), 44-55 (2005).

[22] Essock, E. A., Sinai, M. J., Fechtner, R. D., Srinivasan, N. and Bryant, F. D., "Fourier Analysis of nerve fiber layer measurements from scanning laser polarimetry in glaucoma: emphasizing shape characteristics of the 'double-hump' pattern," J Glaucoma 9, 444-452 (2000).

[23] Essock, E. A., Zheng, Y. and Gunvant, P., "Analysis of GDx-VCC Polarimetry Data by Wavelet-Fourier Analysis across Glaucoma Stages," Invest Ophtalmol Vis Sci 46(8) Aug. (2005).

[24] Iftekharuddin, K. M., "Techniques in Fractal Analysis and Their Applications in Brain MRI," Medical Imaging Systems: Technology and Applications, Edited by Cornelius T. Leondes, Vol. 1: Analysis and Computational Methods, World Scientific Publications, (2005).

[25] Lee, W. L., Chen, Y. C. and Hsieh, K. S., "Ultrasound liver tissues classification by fractal feature vector based on M-band wavelet transform," IEEE Transactions of Medical Imaging, 22(3), 382-392, Mar., (2005).

[26] Lopes, R. and Betrouni, N., "Fractal and Multifractal Analysis: A Review," Medical Image Analysis, 13, 634-649 (2009).

[27] Iftekharuddin, K. M., Islam, A., Shaik, J., Parra, C. and Ogg, R., "Automatic brain tumor detection in MRI: methodology and statistical validation," Proc. of SPIE, 5747, 2012-2022 (2005).

[28] Iftekharuddin, K. M., Zheng, J., Islam, M. A. and Ogg, R. J., "Fractal-based Brain Tumor Detection in Multimodal MRI," Invited Paper for special issue on Emergent Applications of Fractals and Wavelets in Biology and Bio-medicine in Applied Mathematics and Computation, 207, 23-42 (2009).

[29] Iftekharuddin, K. M., Jia, W. and Marsh, R., "Fractal analysis of tumor in brain MR images," Machine vision and applications, 13, 352-362 (2003).

[30] Zook, J. M. and Iftekharuddin, K. M., "Statistical analysis of fractal-based brain tumor detection algorithms," Magnetic Resonance Imaging, 23, 671-678 (2005).

[31] Islam, A., Iftekharuddin, K. M., Ogg, R., Laningham, F. H. and Sivakumar, B., "Multifractal modeling, segmentation, prediction and statistical validation of posterior fossa tumor," Proc. of SPIE, 6915, 69153C-69153C-12 (2008).

[32] Ahmed, S. and Iftekharuddin, K. M., "Discrimination of medulloblastoma and low grade astrocytoma PF tumors using selected MR image features," MemBis 2008, (2008).

[33] Kim, P. Y., Iftekharuddin, K. M., Gunvant, P., Tóth, M., Holló, G. and Essock, E. A., "Efficacy of Fractal Analysis in Identifying Glaucomatous Damage," Proc. of SPIE, 7627, 76271G-1-76271G-10 (2010).

[34] Casas-Llera, P., Rebolleda, G., Muñoz-Negrete, F. J., Arnalich-Montiel, F., Pérez-López, M. and Fernández-Buenaga, R., "Visual field index rate and event-based glaucoma progression analysis: comparison in a glaucoma population," Br J Ophthalmol, 93, 1576-1579 (2009).

[35] Spry, P. G. and Johnson, C. A., "Identification of progressive glaucomatous visual field loss." Survey of Ophthalmology 47, 158-173 (2002).

[36] Gunvant, P., Zheng, Y., Essock, E. A., Chen, P. P., Greenfield, D. S., Bagga, H. and Boehm, M. D., "Predicting Subsequent Visual Field Loss in Glaucomatous Subjects With Disc Hemorrhage Using Retinal Nerve Fiber Layer Polarimetry," J Glaucoma, 14(1), 20-25 (2005).

[37] Essock, E. A., Gunvant, P., Zheng, Y., Garway-Heath, D. F., Kotecha, A. and Spratt, A, "Predicting Visual Field Loss in Ocular Hypertensive Patients Using Wavelet-Fourier Analysis of GDx Scanning Laser Polarimetry," Optometry and Vision Science, 84(5), E380-E386 (2007).

[38] Medeiros F. A., Zangwill, L. M., Alencar, L. M., Bowd, C., Sample, P. A., Susanna, R. Jr, and Weinreb, R. N., "Detection of Glaucoma Progression with Stratus OCT Retinal Nerve Fiber Layer, Optic Nerve Head, and Macular Thickness Measurements," Invest Ophthalmol Vis Sci, 50, 5741-5748, Oct. (2009).

[39] Vapnik, V., [The Nature of Statistical Learning Theory], 2nd edition, Springer, (1999).

[40] Angulo, C., González, L., Català, A. and Velasco, F., "Multi-classification with Tri-class Support Vector Machines. A Review," Neural Processing Letters, 23(1), 89-101 (2007).

[41] Hsu, C. W. and Lin, C. J., "A comparison of methods for multiclass support vector machines," IEEE Trans. on Neural Networks, 13(2), 415-425 (2002).

[42] Chen, G. Y. and Bhattacharya, P., "Function Dot Product Kernels for Support Vector Machine," Pattern Recognition, ICPR 2006, 2, 614-617 (2006).

[43] Cristianini, N., Campbell, C., and Shawe-Taylor, J., [Dynamically Adapting Kernels in Support Vector Machines], Advances in Neural Information Processing Systems, MIT Press, (1999).

[44] Ruta, D. and Gabrys, B., "An Overview of Classifier Fusion Methods," Computing and Information Systems, 7, 1-10 (2000).

[45] Islam, A. M., "Computer-aided pediatric brain tumor detection, prediction and statistical validation using structural MRI and gene expression data," Ph.D. dissertation, Univ. of Memphis, (2008).

[46] Li, X., Wang, L. and Sung, E., "AdaBoost with SVM-based component classifiers," Engineering Applications of Artificial Intelligence, 21(5), 785-795, Aug. (2008).

[47] Shah, N. N., Bowd, C., Medeiros, F. A., Weinreb, R. N., Sample, P. A., Hoffmann, E. M. and Zangwill, L. M., "Combining Structural and Functional Testing for Detection of Glaucoma," Ophthalmology, 113, 1593-1602 (2006).

[48] Horn, F. K., Mardin, C. Y., Laemmer, R., Baleanu, D., Juenemann, A. M., Kruse, F. E. and Tornow, R. P., "Correlation between Local Glaucomatous Visual Field Defects and Loss of Nerve Fiber Layer Thickness Measured with Polarimetry and Spectral Domain OCT," Invest Ophthalmol Vis Sci., 50(5), 1971-1977, May. (2009).

[49] Vesti, E., Johnson, C. A. and Chauhan B. C., "Comparison of different methods for detecting glaucomatous visual field progression," Invest Ophthalmol Vis Sci, 44 (9), 3873-3879, Sep. (2003).

[50] Považay, B., Hofer, B., Hermann, B., Unterhuber, A., Morgan, J. E., Glittenberg, C., Binder, S. and Drexler, W., "Minimum distance mapping using three-dimensional optical coherence tomography for glaucoma diagnosis," J Biomed Opt, 12(4), Jul.-Aug., (2007).

[51] Lauande-Pimentel, R., Carvalho, R. A., Oliveira, H. C., Gonçalves, D. C., Silva, L. M., and Costa, V. P., "Discrimination between normal and glaucomatous eyes with visual field and scanning laser polarimetry measurements," Br. J. Ophthalmol. 85, 586-591, (2001).

[52] "Causes of blindness and visual impairment," World Health Organization, retrieved 02/02/2011

[53] http://www.glaucoma.org/learn/glaucoma_worldw.php, retrieved 02/02/2011

[54] Quigley, H. A., "The number of people with glaucoma worldwide in 2010 and 2020," Br J Ophthalmology, 90(3), 262-267 Mar. (2006).

[55] Curcio, C. A. and Allen, K. A., "Topography of ganglion cells in human retina," The Journal of Comparative Neurology 300, 5-25 (1990).

[56] Webvision.med.utah.edu/book/part-i-foundations/simple-anatomy-of-the-retina

[57] Gupta, D., [Glaucoma diagnosis and management], Lippincott Williams & Wilkins, 1st Edition, Sep. (2004).

[58] Sommer, A., Katz, J. Quigley, H. A., et al. "Clinically detectable nerve fiber atrophy precedes the onset of glaucomatous field loss," Arch Ophthalmol, 109, 77-83 (1991).

[59] Medeiros, F. A., Alencar, L. M., Zangwill, L. M., Bowd, C., Vizzeri, G., Sample, P. A. and Weinreb, R. N., "Detection of Progressive Retinal Nerve Fiber Layer Loss in Glaucoma Using Scanning Laser Polarimetry with Variable Corneal Compensation," Invest Ophtalmol Vis Sci, 50(4), 1675-1681 (2009).

[60] Vermeer, K. A., Reus, N. J., Vos, F. M., Lemij, H. G. and Vossepoel, A. M., "Progression Detection of Glaucoma from Polarimetric Images," Medical Image computing and computer-assisted intervention, 611-619 (2003).

[61] Alencar, L. M., Zangwill, L. M., Weinreb, R. N., Bowd, C., Vizzeri, G, Sample, P. A., Susanna, R. and Medeiros, F. A., "Agreement for Detecting Glaucoma Progression with the GDx Guided Progression Analysis, Automated Perimetry, and Optic Disc Photography," Ophthalmology, AAO, 117(3), 462-470 (2010).

[62] Arnalich-Montiel, F., Casas-Llera, P., Muñoz-Negrete, F. J. and Rebolleda, G., "Performance of glaucoma progression analysis software in a glaucoma population," Graefe's Archive for Clinical and Experimental Ophthalmology, 247(3), 391-397 (2009).

[63] Meditec.zeiss.com

[64] Cirrus™ HD-OCT brochure, http://www.cirrusoctdemo.com/CZM_5947_BS_Cirrus_LY15c%20final.pdf,

[65] Bourezak, R., Lamouche, G. and Cheriet, F., "Artery Wall Extraction from Intravascular OCT Images, ICIAR 2009, LNCS 5627, 792-801 (2009).

[66] Bressler, N. M. and Ahmed, I. I. K., [Essential OCT],

[67] Lin, R., Optical Coherence Tomography for Screening of Donor Corneas and Evaluation of the Retinal Nerve Fiber Layer, PhD Dissertation, Case Western Reserve University

[68] Dersu, I. and Wiggins, M. N., "Understanding Visual Fields, Part II; Humphrey Visual Fields," J. of Ophthalmic Medical Technology, 2(3), (2006).

[69] Mosby's Medical Dictionary, 8th edition, Elsevier, (2009).

[70] Traquair, H. M., "Clinical Detection of Early Changes in the Visual Field," Arch Ophthal. 22, 947-967 (1939).

[71] Silverstone, D. E. and Hirsch, J., Automated visual field testing: Techniques of examination and interpretation, Appleton-Century-Crofts, (1986).

[72] www.agingeye.net/glaucoma/Humphrey.pdf

[73] www.haag-streit-usa.com/haag-streit-products/octopus-perimeters/octopus-300.aspx

[74] Reus, N. J. and Lemij, H. G., "The Relationship between Standard Automated Perimetry and GDx VCC Measurements," Invest Ophthalmol Vis Sci., 45(3), 840-845, Mar., (2004).

[75] Spry, P. G. D., Johnson, C. A., McKendrick, A. M. and Turpin, A., "Measurement error of visual field tests in glaucoma," Br J Ophthalmol, 87, 107-112 (2003).

[76] www.haag-streit-usa.com/products/perimetry

[77] Oppenheim, A. V. and Schafer, R. W., [Discrete-Time Signal Processing], Prentice Hall, Englewood Cliffs, (1989).

[78] Gonzalez, R. C. and Woods, R. E., [Digital Image Processing], 2nd edition, Prentice Hall, Upper Saddle River, (2002).

[79] Rao, R.M. and Bopardikar, A. S., [Wavelet Transforms: Introduction to Theory and Applications], Pearson Education (Singapore), (1998)

[80] Mallat, S.G., "A theory for multiresolution signal decomposition: The Wavelet Representation", IEEE Transactions on Pattern Analysis and Machine Intelligence, 2(7), 674-693 (1989).

[81] Rioul, O. and Vetterli, M., "Wavelets and signal processing," IEEE Signal Processing Magazine, 14-38, Oct., (1991).

[82] Mandelbrot, B. B., "The fractal geometry of nature", San Francisco;Freeman, (1983).

[83] Abry, P., Goncalves, P. and Vehel, J. L., [Scaling, Fractals and Wavelets], John Wiley &Sons, (Hoboken, NJ), (2009).

[84] Sarkar, N. and Chaudhuri, B. B., "An efficient approach to estimate fractal dimension of textural images," Pattern Recognition, Vol. 23, pp. 1035-1041, (1992).

[85] Stanley, H. E. and Meakin, P., "Multifractal phenomena in physics and chemistry," Nature, Vol. 335, pp. 405-409, (1988).

[86] Ivanov, P. C., Amaral, L. A. N., Goldberger, A. L., Havlin, S., Rosenblum, M. B., Struzik, Z. and Stanley, H. E., "Multifractality in healthy heartbeat dynamics," Nature, Vol. 399, pp. 461-465, (1999).

[87] Goncalves, P., "Existence of moments: Application to Multifractal Analysis," Proceedings Int. Conf. on Telecommunications, Acapulco (Mexico) May, (2000).

[88] Ayache, A., Cohen S. and Vehel, J. L., "The covariance structure of multifractional Brownian motion, with application to long range dependence," Proceedings of the International Conference on Acoustics, Speech and Signal Processing, Vol. 6, pp. 3810-3813, (2000).

[89] Bishop, C. M., [Pattern Recognition and Machine Learning], Springer, Singapore, (2006).

[90] Cover, T. and Thomas, J., [Elements of Information Theory], John Wiley & Sons, Inc., New York, 2nd Edition, (2006).

[91] DeLong, E. R., DeLong, D. M. and Clarke-Pearson D. L., "Comparing the areas under two or more correlated receiver operating characteristic curves: a nonparametric approach," Biometrics. Vol. 44, pp. 837-845, (1988).

[92] Anderson, D. R., [Automated Static Perimetry], St Louis, Mosby (1992).

[93] Hodapp, E., Parrish II, R. K. and Anderson D. R., [Clinical Decisions in Glaucoma], St Louis: Mosby & Co; 1993.

[94] Gunvant, P., Zheng, Y., Essock, E. A., Parikh, R. S., Prabakaran, S., Babu, J. G., Shekar, C. G. and Thomas, R., "Comparison of shape-based analysis of retinal nerve fiber layer data obtained From OCT and GDx-VCC," J. Glaucoma. pp. 464-471, Aug. (2009).

[95] Gunvant, P., Kim, P. Y., Iftekharuddin, K. M. and Essock, E. A., "Identifying Glaucoma with Multi-fractal Features from Optical Coherence Tomography," Proc. of SPIE, 7963, 79633S-1 – 79633S-9 (2011).

[96] Kim, P. Y., Iftekharuddin, K. M., Gunvant, P., Tóth, M., Garas, A., Holló, G. and Essock, E. A., "Feature-based Glaucomatous Progression Prediction Using Scanning Laser Polarimetry Data," Proc. of SPIE, 7963, 79633T-1 – 79633T-9 (2011).

[97] Gunvant, P., Kim, P. Y., Tóth, M., Holló, G., Essock, E. A. and Iftekharuddin, K. M., "Predicting Visual Field Loss in Glaucomatous Patients Using Fast–Fourier Analysis (FFA) of GDx-VCC Scanning Laser Polarimetry," manuscript under preparation (2011).

[98] Ferreras, A., Pablo, L. E., Garway-Heath, D. F., Fogagnolo, P., and Garcıa-Feijoo, J., "Mapping Standard Automated Perimetry to the Peripapillary Retinal Nerve Fiber Layer in Glaucoma," Invest. Ophthalmol. Vis. Sci., Vol. 49 (7), pp. 3018-3025, Jul., (2008).

[99] Strouthidis, N. G., Vinciotti, V., Tucker, A. J., Gardiner, S. K., Crabb, D. P., and Garway-Heath, D. F., "Structure and Function in Glaucoma: The Relationship between a Functional Visual Field Map and an Anatomic Retinal Map," Invest. Ophthalmol. Vis. Sci., Vol. 47 (12), pp. 5356-5362, Dec., (2006).

[100] Garway-Heath, D. F., Poinoosawmy, D., Fitzke, F. W., and Hitchings, R. A., "Mapping the Visual Field to the Optic Disc in Normal Tension Glaucoma Eyes," Ophthalmology 107(10), 1809-1815 Oct. (2000).

[101] [The GDx VCC Primer: RNFL Evaluation with the GDx VCC to Diagnose and Monitor Glaucoma], Laser Diagnostic Technologies, Inc (2004).

[102] EyeSuite Application Note, Follow up from HFA with Octopus.